Precision Measurement of the ND280 Magnetic Field in the T2K Neutrino Experiment: Confirmation of the Momentum Scale through Δ^{++} Resonances

Inauguraldissertation
der Philosophisch-naturwissenschaftlichen Fakultät
der Universität Bern

vorgelegt von

Eike Frank

von Leipzig, Deutschland

Leiter der Arbeit:

Prof. Dr. Antonio Ereditato

Albert Einstein Center for Fundamental Physics
Laboratorium für Hochenergiephysik

Precision Measurement of the ND280 Magnetic Field in the T2K Neutrino Experiment: Confirmation of the Momentum Scale through Δ^{++} Resonances

Inauguraldissertation
der Philosophisch-naturwissenschaftlichen Fakultät
der Universität Bern

vorgelegt von

Eike Frank

von Leipzig, Deutschland

Leiter der Arbeit:

Prof. Dr. Antonio Ereditato

Albert Einstein Center for Fundamental Physics
Laboratorium für Hochenergiephysik

Von der Philosophisch-naturwissenschaftlichen Fakultät angenommen.

Der Dekan
Bern, 14.03.2012 Prof. Dr. Silvio Decurtins

Everything comes to him who knows how to wait.

— Wolfgang Pauli

Abstract

A measurement of the magnetic field of the ND280 near detector in the T2K experiment was performed with a dedicated, automated mapping device. A measurement accuracy of $\sim$1 G is obtained for a $\sim$700 G dipole magnetic field, provided by the ND280 magnet. The systematic errors for the nominal ND280 magnetic field of 2000 G (0.2 T) are evaluated. An accuracy of better than 2 G is achieved for the transverse magnetic field components (B_y, B_z). The systematic error of the main component is determined to be $\sigma(B_x) = 11.72$ G for a field of $B_x = 2048.14$ G in the center of the magnet, which corresponds to a magnetic field scale uncertainty of 0.57%. The precise knowledge of the magnetic field meets the requirements for ND280 TPCs of a momentum accuracy of better than 2%. The momentum scale is probed by the reconstructed invariant mass peak of Δ^{++} resonances, which are produced in ν_μ CC interactions. A sample of 126 candidate events, with an expected signal purity of 27.3%, are selected from the data of the 2010 and 2011 runs of T2K, with a neutrino flux corresponding to 1.064×10^{20} POT. A simultaneous fit of signal and background allows to reconstruct the invariant mass peak of the Δ^{++} signal, which is compared to the expected value from MC simulations $m_{\mathrm{inv}}^{\mathrm{MC}}(\Delta^{++}) = 1.218 \pm 0.013$ GeV. The value of $m_{\mathrm{inv}}^{\mathrm{data}}(\Delta^{++}) = 1.207 \pm 0.025$ GeV, which is retrieved from the data, is compatible with the MC expectation within one standard deviation. This is also found to be true for momentum biases between -7% and 18%.

Contents

Introduction

In this thesis, I will present and discuss the results of the magnetic field mapping of the ND280 magnet in the T2K experiment, which was performed in September 2009. The precise knowledge of the magnetic field is a key ingredient to achieve the requirements of knowing the momentum scale of the ND280 detector better than 2%. This will allow T2K to increase the sensitivity for the neutrino mixing parameters Δm^2_{23} and θ_{23} through the measurement of ν_μ disappearance in neutrino oscillations. Also, a precise knowledge of the momentum scale helps to determine θ_{13} in the $\nu_\mu \to \nu_e$ appearance channel. The discovery of θ_{13} is one of the major goals of T2K and is possible to reach in 2012 run period. In July 2011, the T2K collaboration published a $2.5\,\sigma$ indication of a non-zero value for θ_{13}.

In the first chapter, I briefly depict the standard model of particle physics and the role neutrinos play within and beyond this framework. A special emphasis is put to the theory of leptogenesis, since it contains the possibility of explaining the excess of matter over antimatter in our universe with the help of neutrino physics. The recent result of the T2K experiment indicates that θ_{13}, the smallest of the three mixing angles in the PMNS neutrino mixing matrix, might be large enough to measure possible leptonic CP violation within the next few years. This is required in order to test if leptogenesis is realized.

The second chapter describes the T2K neutrino oscillation experiment, which consists of three major parts: the beamline at J-PARC, near detectors to monitor and measure the unoscillated neutrino beam, and the far detector Super-Kamiokande, 295 km away, in order to measure the oscillation signal.

The proton and neutrino beamline at J-PARC (Tokai, Japan) is capable of producing a muon neutrino beam of unprecedented intensity, produced by 30 GeV protons hitting a graphite target. The high intensity allows to take advantage of the off-axis technique, where the produced neutrinos are not exactly directed to the far detector but by an offset of a few degrees to obtain a more monochromatic beam tuned to maximize the sensitivity for $\nu_\mu \to \nu_e$ oscillations. A set of near detectors monitor the beam near the production target; and the far detector Super-Kamiokande, the world's largest water Čerenkov detector.

Special emphasis is given to the description of the ND280 off-axis near detector complex, multi-purpose neutrino detector, holding several subdetectors within the former UA1/NOMAD magnet.

The third chapter describes the design, construction and performance of an automated mapping device. This device was used to precisely measure the ND280 magnetic field. A total of 89 electronic cards, each holding three Hall probes, measured the magnetic field in three dimensions at more than 10^6 spatial points, leading to a granularity of $\sim$5 cm. It is demonstrated that the error of the measurement is at the order of 1 G at a field strength of $\sim$700 G. This results in an error of less than 0.5% for the momentum scale at the nominal ND280 field of 2000 G (0.2 T). This precision of the magnetic field is required to achieve the goal of a momentum scale accuracy of the ND280 TPCs to be better than 2%, because the magnetic field components transverse to the electric field in the TPCs distort the drift of the ionization electrons in the TPCs and gives a bias on the measured momentum.

A check of the momentum scale is presented in the fourth chapter. To probe the momentum scale with a physics reaction, I concentrated on the search for Δ^{++} resonances from neutrino interactions in the ND280 tracker. The so-called "golden channel" of $K^0 \to \pi^+\pi^-$ for detector calibrations does not provide enough statistics in this early phase of the experiment. The invariant mass of the Δ^{++} can be reconstructed with the help of the momentum measurements of the ND280 TPCs. From the position of the invariant mass peak, an upper limit of the error on the momentum scale can be inferred. The study of Δ^{++} resonances also can be used to better understand resonant pion production from neutrinos with an energy around 1 GeV and can form an input to more detailed cross section studies, which are expected to be a major contribution of ND280 in the field of neutrino physics.

Chapter 1

Neutrino Physics

In this chapter the standard model of particle physics (SM) and the role of neutrinos within this framework will be briefly introduced. Since their prediction by W. Pauli in 1930, many properties of neutrinos have been discovered, which, among other things, helped to build the SM. But also exploring neutrino physics itself, as well as physics beyond the SM, are of interest to the research community.

In the past, the observed deficit of electron neutrinos from the sun with respect to the expectations from the standard solar model formulated the so-called solar neutrinos puzzle [1]. This led to the discovery of neutrino oscillations, which implies that neutrinos are massive. In contrast to the flavor mixing in the quark sector, two of the three neutrino mixing angles are large. Current oscillation experiments are aiming at measuring precisely the features and parameters of the neutrino mixing matrix, with a possible prospect of measuring CP violation in the leptonic sector. The recent indications of ν_e appearance from T2K [2] and MINOS [3], as well as the first results from Double-Chooz [4], show that this goal might be achievable within the next few years.

The implication of massive neutrinos raises several questions: Are neutrinos Dirac or Majorana particles? And what is the absolute mass of the neutrinos? These questions are addressed in Section 1.5, which summarizes the results of several experiments exploring the β-decay and the neutrinoless double β-decay ($0\nu2\beta$). But neutrinos are not only interesting in nuclear and particle physics, but also in the field of astrophysics and cosmology. In particular, a possible explanation for the matter excess over antimatter in our universe through the leptogenesis mechanism is a very attractive theory. In the future, it will be interesting to develop further and establish our picture of neutrinos and their properties.

This chapter is divided into five sections. The first section summarizes the history of the discovery of the neutrino, followed by a section which describes briefly the standard model of particle physics and the assigned neutrino properties within this framework. Neutrino interactions are described in Section 1.3, which complements the view of standard model neutrinos. Section 1.4 discusses in more detail the framework of neutrino oscillations as an extension of the SM. After deriving the general flavor transition probabilities in vacuum, neutrino oscillation with three flavors without and with matter will be briefly examined. The observation of neutrino oscillations implies that at least two of three neutrino masses must be non-zero. The current knowledge of the implications of massive neutrinos is discussed in Section 1.5. This includes the hierarchy problem of neutrino masses, measurements of the absolute value of neutrino masses and the question whether neutrinos are Dirac or Majorana particles. In Section 1.6 an outlook for the next years in neutrino oscillation physics is presented. A large value for the mixing angle θ_{13} opens a window to discover CP violation in the near future. If CP violation turns out to be large and neutrinos are of Majorana type, then leptogenesis might have occurred in the early universe, as will be discussed in the last section of this chapter.

1.1 The Discovery of the Neutrinos

In 1930 W. Pauli postulated the existence of a neutral particle in order to explain the continuous energy spectrum in β decays [5]. Since the only alternative to this new particle was the violation of the conversation laws for energy and angular momentum, the neutrino was soon accepted as a new fundamental particle. However, neutrinos have a very low cross section of $\sigma{\sim}10^{-44}\,\mathrm{cm}^2$ for an energy of $\sim 1\,\mathrm{MeV}$ [6]. This value is based on E. Fermi's theory of β-decays [7]. It was not before 1956 that F. Reines and C. Cowan finally discovered the neutrino in an experiment near the Savannah River nuclear reactor by measuring inverse β-decay reactions ($\bar{\nu}_e + p \to e^+ + n$) [8]. Two photons from the annihilation of the positron with an electron of the target material form a prompt signal. This is required to be in coincidence with a delayed signal from neutron capture in the target nuclei, where gammas in the MeV energy range are emitted.

In 1962, L. Ledermann, M. Schwartz, and J. Steinberger discovered that there must be at least two types of neutrinos, one being electronic and one being muonic [9]. They produced a beam of neutrinos from pions decaying into a muon and a neutrino in more than 99% of the cases. With the help of a spark chamber, they showed that the interacting neutrinos only produced muons and no electromagnetic showers.

With the discovery of the τ-lepton in 1975, the search for the third type of neutrino started. It lasted until the year 2000 when the τ-neutrino was discovered in the DONuT experiment at the Tevatron accelerator at Fermilab [10]. A neutrino beam with a large fraction of ν_τ (5%) was produced and shot on an emulsion target interlaced with iron plates. Nine τ-decays were observed with a background of 1.5 events, and thus the ν_τ was discovered.

Also in the 1990s, the measurement of the hadronic cross section for the Z resonance and its width at the four LEP experiments (ALEPH, DELPHI, L3 and OPAL) at CERN showed that there are exactly three generations of weakly interacting light neutrinos. As a consequence, with ν_e, ν_μ, and ν_τ all three standard model neutrinos had been discovered [11].

1.2 Neutrinos and the Standard Model of Particle Physics

1.2.1 The Standard Model

The Standard Model of Particle Physics (SM) depicts the fundamental particles and the forces which describe the interactions between these particles. It includes the electromagnetic, strong, and weak forces and their carrier particles (gauge bosons), but not gravity for which a carrier particle has not yet been discovered.

The fundamental particles consist of 24 fermions, six leptons and six quarks with their twelve antiparticles, and the gauge bosons. Leptons are grouped in three families, also called flavors, of doublets. Each doublet contains a negatively charged and a neutral lepton - an electron, muon, or tauon and its corresponding neutrino. Quarks are also grouped in three doublets, with one partner having the charge +2/3 (up, charm, top) and the second partner having the charge -1/3 (down, strange, bottom). The antiparticles have the same mass as particles, but opposite charge. The second group of particles, the gauge bosons, are the mediators of forces between the just mentioned elementary particles.

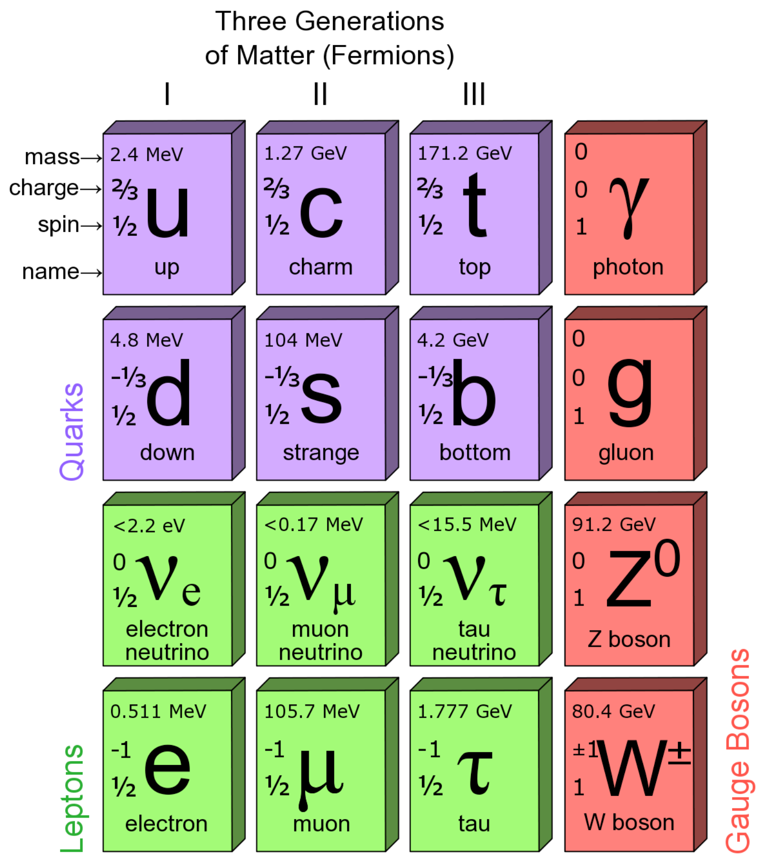

Figure 1.1: Overview of the standard model particles [12].

The mediators of the strong force are gluons which couple to the color charge (red, blue, green), a quantum number of quarks and gluons. The theory describing this type of interaction is called quantum chromodynamics (QCD). According to QCD, strongly interacting particles are in color singlet state. This implies that they are neutral with respect to the color charge, either by combining three quarks with red, green and blue charge, or having a pair of quarks with color and anticolor, e.g. red and antired. The theory also predicts the non-existence of free quarks. Particles are either formed from two quarks (mesons) or three quarks (baryons). Free particles formed from more than three quarks have not been observed yet.

The electromagnetic force acts on charged particles via photon exchange. The photon is massless, has no charge, and spin 1. Electromagnetic interactions are described by quantum electro dynamics (QED), which allows for particle creation and annihilation processes and was developed in the 1940s by R. Feynman, J. Schwinger, and S. Tomonaga [13, 14, 15].

The weak force has three mediators: the neutral Z boson with a mass of 91.2 GeV and the charged $W^{\pm}$ bosons with a mass of 80.4 GeV [16]. It is the only force which has an effect on all fermions of the SM and on $W^{\pm}$ and Z. Weak interactions allow for a conversion from one flavor to another of the particle in concern. Based on the theory of N. Cabibbo [17], in which the hadronic quark flavor states are a superposition of the quark mass states (and vice versa), M. Kobayashi and T. Maskawa generalized the picture to a three flavor framework and introduced a unitary mixing matrix, called CKM-matrix, which describes the mixing between flavor and mass eigenstates of the quarks [18]. The details of flavor mixing will be discussed for the case of neutrinos in Section 1.4.

A model of the weak force was presented for the first time by E. Fermi in 1933 [7]. In 1968, S. Glashow, A. Salam and S. Weinberg succeeded in combining the weak and electromagnetic force to one common electroweak force [19, 20]. According to their theory, the weak and the electromagnetic force are just different manifestations of the same force at low energies. The photon, Z and $W^{\pm}$ are therefore a superposition of the four gauge bosons of the electroweak theory (W_1, W_2, W_3 and B_0).

Within the framework of the SM, the three neutrinos (and their antiparticles) have no mass, no charge and no color charge and therefore only interact via the weak force. The spin of neutrinos is always opposite to its direction of flight, i.e. neutrinos have helicity -1, which M. Goldhaber showed 1958 in his experiment [21]. In 1957, C.-S. Wu discovered that parity is not conserved for the weak interaction [22]. Applying parity transformation (P) on a left-handed neutrino delivers a right-handed neutrino, but this state is not observed. Adding the charge conjugation (particle-antiparticle transformation) to the parity transformation leads to the conserved symmetry of the CP transformation. Hence, antineutrinos have helicity $+1$. Because neutrinos in the SM are massless, this implies that neutrinos are always left-handed and antineutrinos right-handed. However, experiments in 1964 with kaon decays [23] and later on B^0 decays [24] showed that also the CP transformation is not fully conserved. It is not known if this is only true for hadronic decays or if this statement also holds in the leptonic sector. In Section 1.6.3 leptonic CP violation is presented in more detail.

1.3 Neutrino Interactions

As a consequence of interacting only via the weak force, neutrinos have a very low cross section for interacting with other particles, $\sigma{\sim}10^{-38}\,\mathrm{cm}^2\mathrm{GeV}^{-1}$ for neutrino energies above ${\sim}1\,\mathrm{GeV}$. Therefore, a huge amount of detector material is needed to be able to detect neutrino interactions. The interactions can be classified into two main categories, neutral current (NC) interactions with an exchange of a Z boson and charged current (CC) interactions in which a W boson is exchanged. Observing the corresponding outgoing particles in the detector without seeing an incoming particle characterizes a neutrino event, e.g. the observation of a μ^- representing a ν_μ CC interaction.

When classifying neutrino events, generally three types are distinguished. In the sub-GeV range, where the momentum transfer Q^2 of the exchanged W boson is not sufficient to break the target nucleus, quasi-elastic (QE) scattering ($\nu_\ell + n \to \ell^- + p$) is the dominant process, with $\ell = e, \mu, \tau$. For neutrino energies above ${\sim}10\,\mathrm{GeV}$, the Q^2 is large enough to break the target nucleus, and the absorbed energy is transformed into pions and other particles forming a hadronic shower. These processes are called deep inelastic scattering (DIS). In the energy range around 1 GeV, single pion (1π) production is also an important process. Figure 1.2 summarizes the current knowledge for the energy dependent cross sections of these processes.

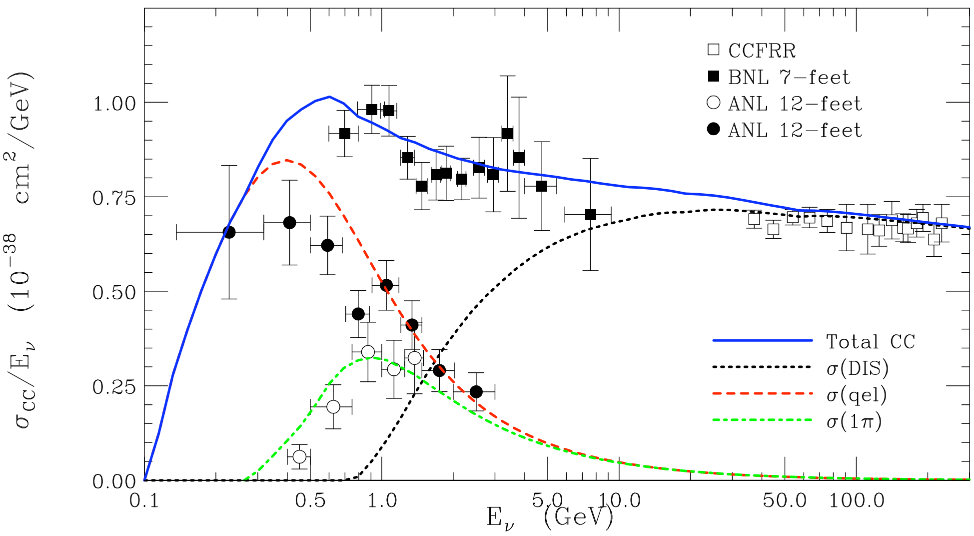

Figure 1.2: Overview of neutrino cross sections in the energy region between 0.1 GeV and 300 GeV [25].

The production of one or more pions can occur through DIS, coherent scattering (COH) or resonances (RES). In resonant processes the provided energy excites the target nucleus into a resonant baryon state. The state with the least required energy is the $\Delta(1232)$ resonance. The Δ^{++} production process $\nu_\mu + p \to \mu^- + \Delta^{++} \to \mu^- + \pi^+ + p$ will be studied in detail in Chapter 4. In Figure 1.3 the corresponding Feynman graphs are shown explaining the differences.

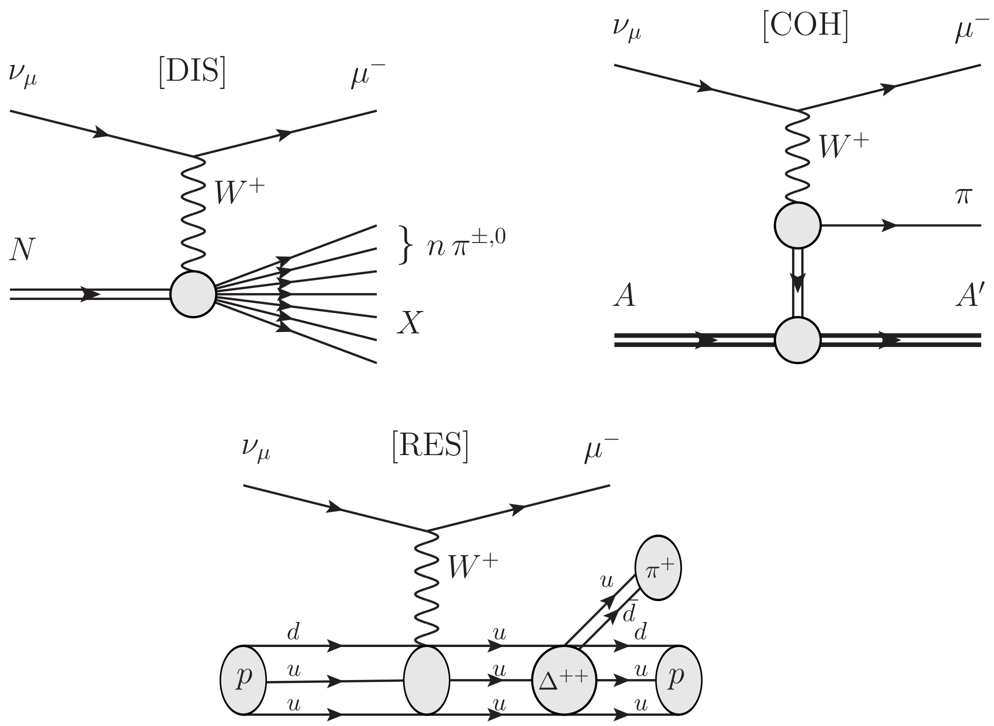

Figure 1.3: The main types of charged current muon neutrino scattering on a free nucleon/nucleus that produce pions directly. From top left to bottom right are: deep inelastic scattering (DIS), coherent pion production (COH), and resonance production (RES). In the figure N is a nucleon, A is a nucleus, and X represents the hadronic system excluding pions. The time axis in these and all diagrams in the following figures is from left to right [26].

NC events are much harder to detect, since the neutrino does not change into a charged lepton. They are only detectable when the transferred momentum (via the Z boson) is big enough to produce other particles, such as pions off the target nucleus.

The prior classification of neutrino events can be made analogously for antineutrinos, except that antineutrino cross sections (for low energies $E_\nu \lesssim 1\,\text{GeV}$) are lower by a factor three according to the quark parton model for CC interactions [27]. The $\sigma(\bar{\nu})/\sigma(\nu)$ ratio rises to one half for higher energies ($E_\nu \gtrsim 20\,\text{GeV}$) as sea quarks[a] contribute to neutrino scattering on nuclei, for recent results see for example [28].

[a]Sea quarks are virtual quark antiquark pairs, which occur in nucleons due to the strong force. They build a "sea" of quarks around the valence quarks (e.g. u, u, d for a proton) of the hadron.

1.3.1 Neutrino Cross Sections

In order to allow high precision measurements of neutrino properties, a good knowledge of neutrino cross sections is needed. Not only is this necessary to estimate the number of events which will be observed in a detector, it also allows to test the underlying theoretical models which predict neutrino interaction event rates and types. At high accelerator energies ($\gtrsim$ 10 GeV), where DIS is the dominant channel, neutrino interaction models are rather well understood. In the sub-to-few GeV range QE scattering, resonant pion production, and coherent pion production build a large fraction of the total cross section. Understanding the exact composition of these processes is one of the major research items of contemporary neutrino physics.

Data for this energy region come mainly from spark chamber, bubble chamber and emulsion experiments of the 1970s and 1980s and build the basis for the neutrino interaction models of almost all of the currently used neutrino interaction Monte Carlo (MC) generators, in particular NEUT [29] and GENIE [30]. Besides the standard DIS formulas and parton distribution functions (see for example [16]), the most commonly used theoretical models are the free nucleon QE cross sections from Llewellyn Smith [31] and the description of resonant pion production from Rein and Sehgal [32]. Across the various MC generators, the main differences arise from the treatment of nuclear and final state effects as well as the implementation of Fermi gas models [33] and the way the resonant and DIS regions are combined. The following section will concentrate on pion production, because it is the most relevant process for the studies in the last chapter of this thesis.

1.3.2 Pion Production

Pions can be produced from neutrino interactions by several mechanisms: resonant pion production, coherent pion production, DIS, and pions arising from final state interactions. The dominant channel is through the excitation of baryon resonances, which decay in a nucleon-pion final state:

$$\nu_\mu + N \rightarrow \mu^- + N^* \text{ and then } N^* \rightarrow \pi + N'$$

For single pion production, charge conservation allows for four NC and three CC final states:

$$\begin{array}{llll}
\text{NC:} & \nu_\mu + n \rightarrow \nu_\mu + n + \pi^0 & \text{CC:} & \nu_\mu + n \rightarrow \mu^- + p + \pi^0 \\
 & \nu_\mu + n \rightarrow \nu_\mu + p + \pi^- & & \nu_\mu + n \rightarrow \mu^- + n + \pi^+ \\
 & \nu_\mu + p \rightarrow \nu_\mu + p + \pi^0 & & \nu_\mu + p \rightarrow \mu^- + p + \pi^+ \\
 & \nu_\mu + p \rightarrow \nu_\mu + n + \pi^+ & &
\end{array}$$

MC generators generally base the theoretical calculations of these resonances on the model by Rein and Sehgal [32] and then tune the theoretical predictions to the data. The dominant process at energies around 1 GeV is the excitation of a $\Delta(1232)$ resonance, but also higher resonances can be excited. The available data for resonant production stems mainly from bubble chamber [34, 35, 36] and also a few spark chamber experiments [37]. Of special interest are the distributions of kinematical values, such as the invariant mass W of the resonance or the transfered four momentum Q^2, as they allow to test the theoretical predictions in detail, in particular to test the power of assuming free nucleon scattering.

For NC events the data is even more limited and usually is reported in the form of a NC/CC ratio to reduce systematic errors.

Recently, the cross sections (or upper limits for them) for coherent pion production were measured by K2K [38] , MiniBooNE [39] and SciBooNE [40, 41]. They report a significantly lower value than predicted by the Rein Sehgal model, both for the NC ($\nu_\mu A \to \nu_\mu A\pi^0$) and the CC($\nu_\mu A \to \mu^- A\pi^+$) channel.

Not only single pion production, but also multiple pion production and DIS need to be studied in detail to understand the overlap region around 1 GeV. Especially the understanding of nuclear effects are important to model neutrino interactions properly.

1.4 Neutrino Mixing and Oscillations

In the SM, there are three lepton flavor doublets with the three massless neutrinos: ν_e, ν_μ and ν_τ. From the data of several experiments, it can be inferred that neutrinos can change their flavor by means of neutrino oscillations. Among many other experiments, the most important data today come from Super Kamiokande [42, 43] for atmospheric neutrinos, KamLAND [44, 45] and CHOOZ [46] for reactor neutrinos, K2K [47, 48], OPERA [49], MINOS [50] and T2K [2] for long baseline accelerator experiments, as well as several solar neutrino experiments, such as SNO [51], GALLEX [52], SAGE [53] and Super-Kamiokande [54].

The observation of flavor changing neutrinos via oscillations implies that neutrinos have masses and that leptons mix. Massive neutrinos are described by three or more[b] neutrino mass eigenstates ν_1, ν_2 and ν_3. Lepton mixing implies that neutrinos of flavor e, μ or τ, the neutrino flavor eigenstate, is a linear combination of the mass eigenstates and vice versa.

$$|\nu_\alpha\rangle = \sum_i U_{\alpha i}|\nu_i\rangle, \quad |\nu_i\rangle = \sum_\alpha U^*_{i\alpha}|\nu_\alpha\rangle \tag{1.1}$$

with $i = 1, 2, 3$; $\alpha = e, \mu, \tau$ and a unitary mixing matrix U, the Pontecorvo-Maki-Nakagawa-Sakata (PMNS) matrix [55, 56], in analogy to the CKM matrix in the quark sector.

Neutrino oscillations extend the SM, in which lepton flavor is conserved and all neutrinos are massless, such that lepton flavor transitions $\nu_\alpha \leftrightarrow \nu_\beta$ are not allowed, where $\alpha \neq \beta$ represent two different flavors. Below, the transition probability $P(\nu_\alpha \to \nu_\beta)$ for one flavor eigenstate $|\nu_\alpha\rangle$ oscillating into another $|\nu_\beta\rangle$ will be derived in a generic way, following [57]. The derivation shows the important role of the squared mass differences of the neutrino mass eigenstates, and the obtained result allows to outline the important features of contemporary and future neutrino oscillation physics.

[b] If there are more then three neutrino mass eigenstates, then at least one of the linear combinations $|\nu_s\rangle = \sum_i U_{\alpha i}|\nu_i\rangle$ does not have a charged-lepton partner and does not couple to the standard model W and Z bosons. This theory of these so-called sterile neutrinos is not discussed in this thesis, although it is another interesting possible extension of the SM.

Introducing a mass operator $\hat{M}$, one obtains $\langle\nu_i|\hat{M}|\nu_j\rangle = m_i\delta_{ij}$, with $m_i - m_j \neq 0$ for $i \neq j$, and the Kronecker delta δ_{ij} . Unitarity implies

$$UU^\dagger = 1, \quad \text{i.e.} \quad \sum_i U_{\alpha i}U^*_{i\beta} = \delta_{\alpha\beta}, \quad \sum_\alpha U_{\alpha i}U^*_{j\alpha} = \delta_{ij}, \tag{1.2}$$

with the adjoint matrix $U^\dagger$. For antineutrinos ($\bar{\nu}_\alpha$) $U_{\alpha i}$ needs to be replaced with $U^*_{i\alpha}$, such that

$$|\bar{\nu}_\alpha\rangle = \sum_i U^*_{i\alpha}|\bar{\nu}_i\rangle.$$

In the rest frame of the neutrino mass state ν_i, the neutrino obeys the Schrödinger equation[c]

$$\boldsymbol{i}\frac{\partial}{\partial\tau}|\nu_i(\tau)\rangle = E_i|\nu_i(\tau)\rangle,$$

which can be solved through its time dependence

$$|\nu_i(\tau)\rangle = e^{-\boldsymbol{i}E_i\tau}|\nu_i(0)\rangle.$$

Here, τ is the proper time of the neutrino and E_i the energy of a neutrino in mass state ν_i. With the time t and the position L, one obtains

$$|\nu_i(t)\rangle = e^{-\boldsymbol{i}(E_i t - pL)}|\nu_i(0)\rangle = e^{-\boldsymbol{i}(E_i - p)t}|\nu_i(0)\rangle,$$

where the approximation $L \approx t$ is used, which is valid for momenta $p \gg m_i$, and $E \approx p$ is the observable neutrino energy. This leads to the relativistic approximation $E_i = \sqrt{p^2 + m_i^2} \approx p + \frac{m_i^2}{2p} \approx E + \frac{m_i^2}{2E}$, which holds for neutrinos because of their small absolute masses. The neutrino time evolution thus reads

$$|\nu_i(t)\rangle = e^{-\boldsymbol{i}\cdot\frac{m_i^2}{2E}t}|\nu_i(0)\rangle.$$

As a next step, the time dependent transition amplitude $A_{\alpha\beta} = \langle\nu_\beta|\nu_\alpha(t)\rangle$ is calculated for the flavor transition $\nu_\alpha \to \nu_\beta$. The time evolution of the state $|\nu_\alpha\rangle$ is retrieved to be

$$|\nu_\alpha(t)\rangle = \sum_i U_{\alpha i}e^{-\boldsymbol{i}\frac{m_i^2}{2E}t}|\nu_i\rangle,$$

with Equation 1.1. The amplitude becomes

$$A_{\alpha\beta}(t) = \sum_j\sum_i\langle\nu_j|U^*_{j\beta}U_{\alpha i}e^{-\boldsymbol{i}\frac{m_i^2}{2E}t}|\nu_i\rangle = \sum_i U^*_{i\beta}U_{\alpha i}e^{-\boldsymbol{i}\frac{m_i^2}{2E}t},$$

where $\langle\nu_i|\nu_j\rangle = \delta_{ij}$ was used. With the distance $L = t$ between neutrino source and target, one obtains

$$A_{\alpha\beta}(t) = A_{\alpha\beta}(L) = \sum_i U_{\alpha i}U^*_{i\beta}e^{-\boldsymbol{i}\frac{m_i^2}{2}\cdot\frac{L}{E}}.$$

[c]Throughout this thesis the convention $\hbar = c = 1$ will be used, which is common in particle physics.

Therefore, the transition probability between two flavors ν_α and ν_β is

$$\begin{aligned} P(\nu_\alpha \to \nu_\beta; t) &= |A_{\alpha\beta}(t)|^2 = \left| \sum_i U_{\alpha i} U^*_{i\beta} e^{-\boldsymbol{i}\frac{m_i^2}{2}\cdot\frac{L}{E}} \right|^2 \\ &= \sum_j \sum_i U_{\alpha i} U^*_{i\beta} U^*_{j\alpha} U_{\beta j} e^{-\boldsymbol{i}\frac{\Delta m_{ij}^2}{2}\cdot\frac{L}{E}} \\ &= \sum_i |U_{\alpha i} U^*_{i\beta}|^2 + 2\Re \sum_{j>i} U_{\alpha i} U^*_{j\alpha} U^*_{i\beta} U_{\beta j} e^{-\boldsymbol{i}\frac{\Delta m_{ij}^2}{2}\cdot\frac{L}{E}}, \end{aligned}$$

with $\Delta m_{ij}^2 = m_i^2 - m_j^2$. This implies that flavor transitions require non-degenerate mass eigenstates. Therefore, at least one of the mass eigenstates is not zero, which is an extension to the SM. Applying unitarity (Equation 1.2), one gets

$$P(\nu_\alpha \to \nu_\beta; t) = \delta_{\alpha\beta} - 2\Re \sum_{j>i} U_{\alpha i} U^*_{j\alpha} U^*_{i\beta} U_{\beta j} \left[1 - e^{-\boldsymbol{i}\frac{\Delta m_{ij}^2}{2}\cdot\frac{L}{E}} \right], \tag{1.3}$$

or split into a real and an imaginary part:

$$\begin{aligned} P(\nu_\alpha \to \nu_\beta; t) = \delta_{\alpha\beta} &- 4\Re \sum_{j>i} U_{\alpha i} U^*_{j\alpha} U^*_{i\beta} U_{\beta j} \sin^2\left(\Delta m_{ij}^2 \frac{L}{4E} \right) \\ &+ 2\Im \sum_{j>i} U_{\alpha i} U^*_{j\alpha} U^*_{i\beta} U_{\beta j} \sin\left(\Delta m_{ij}^2 \frac{L}{2E} \right). \end{aligned} \tag{1.4}$$

To help focusing on the main features, the following shorter notation is used:

$$P_{\alpha\beta} = \delta_{\alpha\beta} - 4\Re^{ij}_{\alpha\beta} \sin^2 \frac{\Delta_{ij}}{2} + 2\Im^{ij}_{\alpha\beta} \sin \Delta_{ij},$$

where

$$P_{\alpha\beta} = P(\nu_\alpha \to \nu_\beta; t), \quad \bar{P}_{\alpha\beta} = P(\bar{\nu}_\alpha \to \bar{\nu}_\beta; t),$$

$$\Im^{ij}_{\alpha\beta} = \Im \sum_{j>i} U_{\alpha i} U^*_{j\alpha} U^*_{i\beta} U_{\beta j}, \quad \Re^{ij}_{\alpha\beta} = \Re \sum_{j>i} U_{\alpha i} U^*_{j\alpha} U^*_{i\beta} U_{\beta j},$$

$$\Delta_{ij} = \Delta m_{ij}^2 \frac{L}{2E}.$$

The sign of the imaginary part changes for antineutrinos, such that

$$\Delta P^{CP}_{\alpha\beta} = P_{\alpha\beta} - \bar{P}_{\alpha\beta} = 4\Im^{ij}_{\alpha\beta} \sin \Delta_{ij}. \tag{1.5}$$

This implies the possibility of detecting CP violation, which will be the topic of Section 1.6.3.

1.4.1 Neutrino Mixing with three Flavors

In the SM we have three neutrino flavors (ν_e, ν_μ and ν_τ) and therefore retrieve a 3×3 mixing matrix with three independent mixing angles $0 \leq \theta_{ij} \leq \frac{\pi}{2}$ and the three differences of the squared masses Δm^2_{ij} with two degrees of freedom ($\Delta m^2_{23} = \Delta m^2_{13} - \Delta m^2_{12}$). Additionally, an imaginary phase δ^{CP} of the mixing matrix accounts for possible CP violation with $-\pi \leq \delta^{CP} \leq \pi$. If the CP violating phase (δ^{CP}) and all three mixing angles (θ_{ij}) differ from zero, neutrinos and antineutrinos behave differently: $P(\nu_\alpha \rightarrow \nu_\beta) \neq P(\bar{\nu}_\alpha \rightarrow \bar{\nu}_\beta)$. The most widely used parameterization of the PMNS matrix, with $c_{ij} = \cos\theta_{ij}$ and $s_{ij} = \sin\theta_{ij}$, is:

$$
\begin{aligned}
U &= \overbrace{\begin{pmatrix} 1 & 0 & 0 \\ 0 & c_{23} & s_{23} \\ 0 & -s_{23} & c_{23} \end{pmatrix}}^{\text{solar}} \times \overbrace{\begin{pmatrix} c_{13} & 0 & s_{13}e^{-i\delta^{CP}} \\ 0 & 1 & 0 \\ -s_{13}e^{i\delta^{CP}} & 0 & c_{13} \end{pmatrix}}^{\text{accelerator/reactor}} \times \overbrace{\begin{pmatrix} c_{12} & s_{12} & 0 \\ -s_{12} & c_{12} & 0 \\ 0 & 0 & 1 \end{pmatrix}}^{\text{atmospheric}} \\
&= \begin{pmatrix} c_{12}c_{13} & s_{12}c_{13} & s_{13}e^{-i\delta^{CP}} \\ -s_{12}c_{23} - c_{12}s_{23}s_{13}e^{i\delta^{CP}} & c_{12}c_{23} - s_{12}s_{23}s_{13}e^{i\delta^{CP}} & s_{23}c_{13} \\ s_{12}s_{23} - c_{12}c_{23}s_{13}e^{i\delta^{CP}} & -c_{12}s_{23} - s_{12}c_{23}s_{13}e^{i\delta^{CP}} & c_{23}c_{13} \end{pmatrix}
\end{aligned}
\tag{1.6}
$$

The first term describes the parameters relevant for the oscillation of solar neutrinos, while the third term represents atmospheric neutrinos. The middle term describes the oscillation of reactor neutrinos and is an important ingredient for $\nu_\mu \rightarrow \nu_e$ oscillations in current long-baseline accelerator experiments. The CP violating phase δ^{CP} is coupled to $\sin\theta_{13}$. This is an arbitrary choice of parameterization, but reflects the fact that θ_{13} is the smallest of the three mixing angles. Therefore, a possible observation of CP violation in the leptonic sector critically depends on the value of θ_{13}. Note that possible Majorana phases are not considered in this parameterization, because the complex conjugated terms cancel out when calculating the oscillation probabilities. This implies that neutrino oscillation experiments cannot detect these phases and thereby distinguish between Dirac and Majorana neutrinos.

1.4.2 Neutrino Oscillations in Matter

Strictly speaking, the above mechanism is only valid for neutrinos in vacuum. If neutrinos traverse matter, the Mikheyev Smirnov Wolfenstein (MSW) effect [58, 59] has to be taken into account, which differs in strength across the neutrino flavors. Electron neutrinos have a higher probability of interaction in ordinary matter than the other two flavors because of the electron abundance in the traversed matter. As shown in Figure 1.4, the ν_e can scatter elastically with the e^- by exchanging a W^+. This charged current elastic scattering on an e^- is forbidden for the other two flavors. Therefore, an additional potential $V(L) = \sqrt{2}G_F N_e(L)$, where G_F is the Fermi constant and $N_e(L)$ is the position dependent electron density), is added to the ν_e energy ($E' \rightarrow E + V(L)$) and changes the oscillation probability for ν_e.

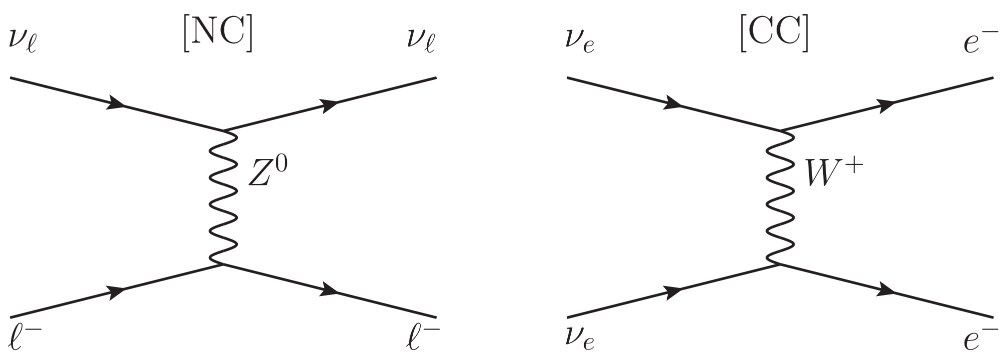

Figure 1.4: Feynman graphs for elastic neutrino scattering. While the neutrinos of all three flavors ($\ell = e, \mu, \tau$) can interact with electrons through NC by exchanging a Z boson (left graph), only electron neutrinos can scatter in CC mode by exchanging a W boson (right graph).

The MSW effect is needed to explain the solar electron neutrino deficit, which was observed by several experiments. While traveling through the sun, the neutrinos undergo the MSW effect, which changes the energy of the electron neutrinos. Therefore, the oscillation probability is altered and the MSW effect leads to a reduced electron neutrino rate on the Earth. The SNO experiment measured the total neutrino flux through NC interactions in addition to the electron neutrino flux through CC interactions and found it to be conserved (see Figure 1.5). This result could explain the electron neutrino deficit with the help of neutrino oscillations and the MSW effect, and thereby solving the solar neutrino puzzle.

Also for long baseline experiments, the MSW effect can alter the transition probabilities with respect to oscillations in vacuum. In contrast to the solar case, where the MSW effects arises from the adiabatic neutrino propagation in the sun [63], for long baseline experiments the matter effects are resonant. This is especially important for $\nu_\mu \to \nu_e$ oscillations when comparing the results of the relevant long baseline experiments (T2K and NOvA [64]) in the near future. Matter effects are also a key ingredient for understanding leptonic CP violation and the neutrino mass hierarchy, as I will depict in more detail below and in Sections 1.6.3 and 1.5.1.

With matter effects for electron neutrinos only, the effective Hamiltonian can be written as

$$H' = \frac{1}{2E}\left[U\begin{pmatrix}0 & 0 & 0\\ 0 & \Delta m_{21}^2 & 0\\ 0 & 0 & \Delta m_{31}^2\end{pmatrix}U^\dagger + \begin{pmatrix}A(L) & 0 & 0\\ 0 & 0 & 0\\ 0 & 0 & 0\end{pmatrix}\right], \tag{1.7}$$

where

$$A(L) = 2EV(L) \simeq 2.3\times 10^{-4}\,\mathrm{eV}^2\frac{\rho(L)}{3\,\mathrm{g\,cm}^{-3}}\frac{E}{\mathrm{GeV}}$$

and $\rho(L)$ is the matter density of the medium as a function of the neutrino traveling

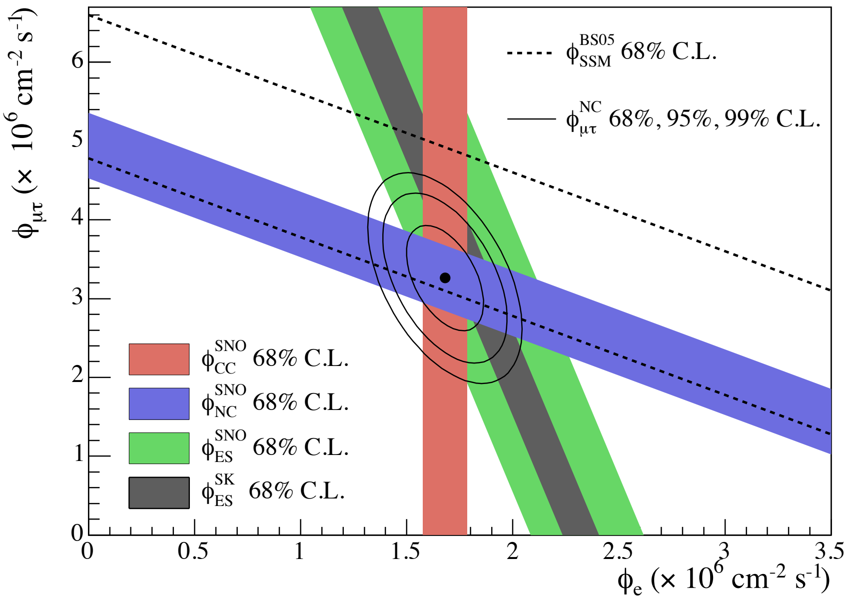

Figure 1.5: Flux of $\mu + \tau$ neutrinos versus flux of electron neutrinos from the sun. CC, NC and ES flux measurements are indicated by the filled bands. The total ^{8}B solar neutrino flux predicted by the Standard Solar Model [60] is shown as dashed lines, and that measured with the NC channel is shown as the solid band parallel to the model prediction. The narrow band parallel to the SNO ES result corresponds to the Super-Kamiokande result in [61]. The intercepts of these bands with the axes represent the $\pm 1\sigma$ uncertainties. The non-zero value of $\phi_{\mu\tau}$ provides strong evidence for neutrino flavor transformation. The point represents ϕ_e from the CC flux and $\phi_{\mu\tau}$ from the NC-CC difference with 68%, 95%, and 99% C.L. contours included [62].

distance L. With an average density $\rho_{\mathrm{Crust}} \simeq 2.7\,\mathrm{g\,cm^{-3}}$ of the Earth's crust and $\rho_{\mathrm{Mantle}} \simeq 4.5\,\mathrm{g/cm^3}$ for the Earth's mantle, matter effects are expected to be large for baselines $L \gtrsim 1000\,\mathrm{km}$. For antineutrinos, U needs to be replaced by U^* and the sign of $A(L)$ changes. The oscillation probabilities with matter effects become quite cumbersome. In order to retrieve a better picture of the involved processes, often a second order perturbative expansion in $\alpha = \Delta m^2_{21}/\Delta m^2_{31} \simeq 3 \times 10^{-2}$ is used for the relevant transition probabilities [65, 66, 67]:

$$P_{e\mu} \simeq \sin^2 2\theta_{13}\, T_1 + \alpha\, \sin 2\theta_{13}\, T_2 + \alpha\, \sin 2\theta_{13}\, T_3 + \alpha^2\, T_4, \tag{1.8}$$

where the individual terms are of the form

$$T_1 = \sin^2\theta_{23}\, \frac{\sin^2[(1-\hat{A})\Delta]}{(1-\hat{A})^2}, \tag{1.9}$$

$$T_2 = \sin\delta^{CP}\, \sin 2\theta_{12}\, \sin 2\theta_{23}\, \sin\Delta\, \frac{\sin(\hat{A}\Delta)}{\hat{A}}\, \frac{\sin[(1-\hat{A})\Delta]}{(1-\hat{A})}, \tag{1.10}$$

$$T_3 = \cos\delta^{CP} \ \sin 2\theta_{12} \ \sin 2\theta_{23} \ \cos\Delta \ \frac{\sin(\hat{A}\Delta)}{\hat{A}} \frac{\sin[(1-\hat{A})\Delta]}{(1-\hat{A})}\,, \tag{1.11}$$

$$T_4 = \cos^2 2\theta_{23} \ \sin^2 2\theta_{12} \ \frac{\sin^2(\hat{A}\Delta)}{\hat{A}^2}\,, \tag{1.12}$$

$$\text{with} \quad \Delta \equiv \frac{\Delta m^2_{31}\ L}{4\ E_\nu} \simeq 1.27 \frac{\Delta m^2_{31}}{\mathrm{eV}^2} \frac{L/\mathrm{km}}{E/\mathrm{GeV}}$$

$$\text{and} \quad \hat{A} \equiv \frac{2\sqrt{2} G_F n_e E}{\Delta m^2_{31}} = \frac{A}{\Delta m^2_{31}}.$$

This expansion is interesting for several reasons. All terms couple to the MSW effect through $\hat{A}$. T_1 and T_4 represent the oscillations due to the atmospheric and the solar mass splitting scale, respectively. Which of the two dominates depends on the size of θ_{13}. The first three terms are coupled to $\sin 2\theta_{13}$, such that a precision measurement of this parameter needs to take all the effects into account. Moreover, the CP conserving interference terms T_2 and the CP violating interference term T_3 reveal the entanglement of matter effects with δ^{CP}. The chosen channel $P_{e\mu}$ is the so-called golden channel for future neutrino factories or $\beta-$beams, in which high intense and very pure ν_e (or $\bar{\nu}_e$) beams will be available (see Section 1.6.1). The advantage is the improved possibility to study matter effects as they are enhanced for electron neutrinos. Also, the produced ν_μ (or $\bar{\nu}_\mu$) give a clear and easily distinguishable muon signal in the far detectors.

Current accelerator technology only allows high intense and sufficiently pure muon neutrino beams from pion decays. Therefore, for the current generation of neutrino long-baseline experiments, such as T2K and soon NOvA, the transition probability from muon to electron neutrinos $P_{\mu e} = P_{e\mu}(\delta^{CP} \to -\delta^{CP}, A \to A_{rev})$ is the quantity of interest. $A_{rev} = V_{rev}E/\Delta m^2_{31}$ is the 'reverse' potential, which corresponds to the swapped positions of neutrino source and detector. A_{rev} equals A if there is a symmetric matter profile (such that the T transformation is conserved). This includes the case of matter with constant density, which can be assumed as approximately true for accelerator based neutrino oscillation experiments.

On the one hand, matter effects complicate the precision measurements of the mixing angles and thereby also δ^{CP}. On the other hand, matter effects can help to decide the neutrino mass hierarchy, e.g. through the comparison of the measured $\nu_\mu \to \nu_e$ oscillation probabilities from T2K and NOvA (see also Figure 1.8). Both effects will be depicted in the following sections in more detail.

1.5 Neutrino Mass

The existence of neutrino oscillations implies neutrino masses as derived in the previous section. However, the conclusions which can be drawn from neutrino oscillations are limited. Although the order of magnitude of the mass splitting between m_1, m_2, and m_3 is known, it is not known, if m_3 is the largest or the lightest neutrino mass. This is the neutrino mass hierarchy problem and will be the topic of Section 1.5.1. Moreover, neutrino oscillations are only sensitive to squared mass differences, but cannot reveal the absolute value of neutrino masses (see Section 1.5.2). Also the question, whether neutrinos are Dirac or Majorana particles, needs to be addressed by a different kind of experiment. The most favored mechanism of how Majorana neutrinos acquire mass, the so-called seesaw mechanism, is briefly explained in Section 1.5.3.

1.5.1 Neutrino Mass Hierarchy

Although the squared mass differences between ν_1 and ν_2 in the solar sector as well as between ν_2 and ν_3 in the atmospheric sector are known, nothing can be inferred about the ordering of the two measurements (see Figure 1.6). A global analysis of all solar neutrino experiments favors a solution with $m(\nu_2) > m(\nu_1)$. However, it is not clear whether ν_3 is heavier or lighter than the (ν_1, ν_2) doublet, or in other words whether the sign of Δm_{23}^2 is negative (normal hierarchy) or positive (inverted hierarchy). If $\Delta m_{23}^2 < 0$, matter effects enhance $\nu_\mu \to \nu_e$ oscillations, while otherwise $\nu_\mu \to \nu_e$ oscillations will be suppressed.

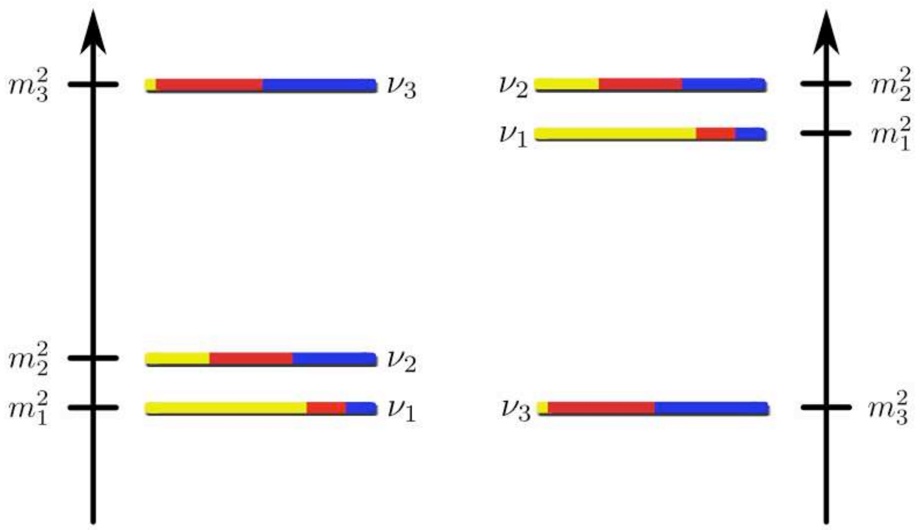

Figure 1.6: The two possible neutrino mass orderings. Left: normal hierarchy ($m_3^2 > m_2^2 > m_1^2$). Right: inverted hierarchy ($m_3^2 < m_1^2 < m_2^2$). The colors (yellow, red and blue) indicate the mixing of the flavors (e, μ and τ) within the mass eigenstates according to the current knowledge [68].

Which hierarchy is realized in nature might be determined in the near future. If direct mass measurements (from tritium decay, cosmology or double β-decay) become sensitive below $\sim$0.01 eV for the neutrino mass, then they have the power to observe the type of hierarchy. Inverted hierarchy is realized if no signal is found in this neutrino mass region (see Figure 1.7).

As depicted in the previous paragraph, long baseline experiments can help to determine the mass ordering through matter effects which are either enhanced for

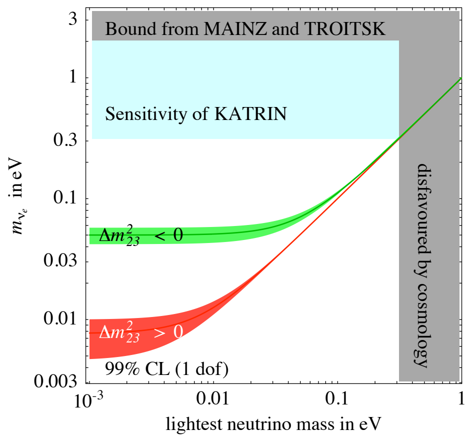

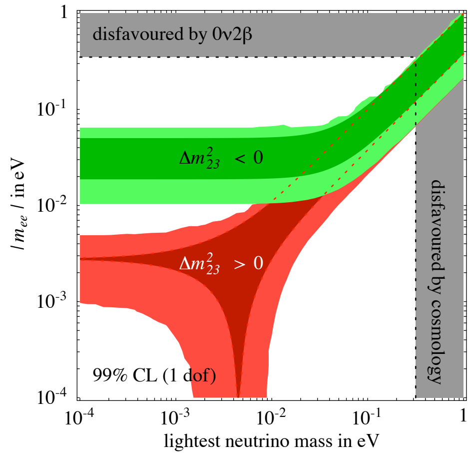

Figure 1.7: Expected ranges for 99% confidence levels as a function of the lightest neutrino mass m_1 or m_3 for normal hierarchy ($\Delta m^2_{23} < 0$) or inverted hierarchy ($\Delta m^2_{23} > 0$), respectively. The left plot shows $m_{\nu e} = \sqrt{\sum_i |U^2_{ei}| m^2_i}$, probed by β-decay; and the right plot shows $|m_{ee}| = |\sqrt{\sum_i U^2_{ei} m_i}|$, probed by $0\nu2\beta$-decay [69].

normal ordering or suppressed for inverted ordering. Although T2K is sensitive to this oscillation channel, the baseline of 295 km is too short for unambiguously discriminating between the two possible hierarchies. However, NOvA with its 810 km baseline will most likely be able to decide the mass hierarchy, as can be inferred from Figure 1.8.

1.5.2 Absolute Neutrino Masses

Although neutrino oscillation provide evidence for non-zero neutrino masses (for at least two out of the three mass eigenstates), there is no way to determine the absolute neutrino mass via neutrino oscillation, since only the differences of the squared masses enter into the transition probabilities. To determine the absolute mass, a different type of experiment is needed. Today's most promising approaches are the study of β-decay of tritium and the study of neutrinoless double β-decay. There are also hints from cosmology about neutrino masses below $\sim$1 eV [70], but the exact limits are model dependent and should be interpreted with care.

Tritium β-decay experiments try to measure the squared masses of electron neutrinos ($m^2_{\nu e} = \sum_i |U^2_{ei}| m^2_i$) through the decay of tritium atoms into helium-3, an electron, and an antielectron-neutrino ($^3H \rightarrow {}^3\mathrm{He} + e^- + \bar{\nu}_e$). If neutrinos have mass, the maximum energy of the electrons will be lessened by the neutrino rest mass m_ν, because of energy conservation: $E^{\max}_e = E_{\mathrm{H}} - E_{\mathrm{He}} - m_\nu = E_0 - m_\nu$, with the binding energies E_{H} and E_{He} for tritium and helium-3, respectively, and the endpoint energy $E_0 = 18.57\,\mathrm{keV}$. The experimental challenge lies in the determination of the kinematic endpoint with a resolution better than 10^{-4}. Moreover, the determination is complicated through the rare population in the decay spectrum with only 2×10^{-13} of all decays expected in the region with $E_e - E_0 < 1\,\mathrm{eV}$ for massless neutrinos [71]. Up to now, β-decay experiments of

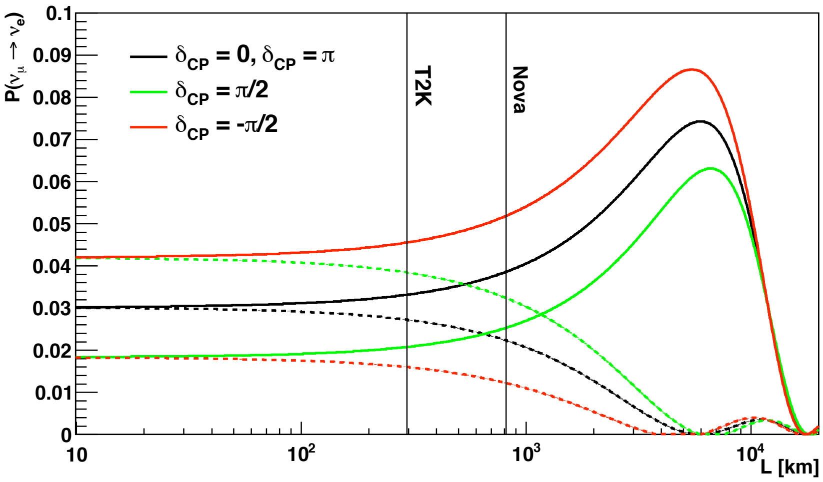

Figure 1.8: The $\nu_\mu \to \nu_e$ oscillation probability $P_{\mu e}$ is shown as a function of the baseline length L, assuming a constant L/E ratio tuned to the maximal oscillation. The colors show different values for the CP violating phase δ^{CP}. The solid lines describe the case of normal hierarchy and the dashed lines the case of inverted hierarchy.

this type lowered the upper limit for the electron neutrino mass to below 2 eV [16]. The KATRIN experiment [71], that will start operation within the next years, aims at reducing this limit by an order of magnitude.

The second approach to set limits for the absolute neutrino masses is through the study of double β-decays, in which two simultaneous β-decays occur. This is strongly suppressed as it is a second-order weak process. Therefore, this process can only be observed in a few nuclei[d] for which the normal β-decay is forbidden, because the final state of the nucleus is at a higher potential than the initial state.

However, the focus is on observing a neutrinoless double β-decay ($0\nu 2\beta$-decay), where two electrons and no neutrinos are emitted (see Figure 1.9). This process is interesting because its observation would prove that neutrinos are Majorana particles, meaning that neutrinos are their own antiparticles. The observation of left-handed neutrinos and right-handed antineutrinos implies that at least one of the neutrinos must have a non-zero mass. Moreover, the observation of Majorana type neutrinos would be compatible with the seesaw mechanism, an elegant way to explain the smallness of the neutrino mass by introducing a heavy right-handed partner. As the existence of Majorana type neutrinos violates the lepton number, theories of leptogenesis (in their simplest versions) can make use of the seesaw mechanism to explain the excess of matter over antimatter in our universe.

The decay rate $\Gamma_{0\nu 2\beta}$ can be measured by experiments, and from this the neutrino masses can be computed

$$\Gamma_{0\nu 2\beta} = G \cdot |\mathcal{M}^2| \cdot |m_{ee}|^2,$$

[d] As of today only 35 naturally occurring isotopes are known which are capable of undergoing double β-decay.

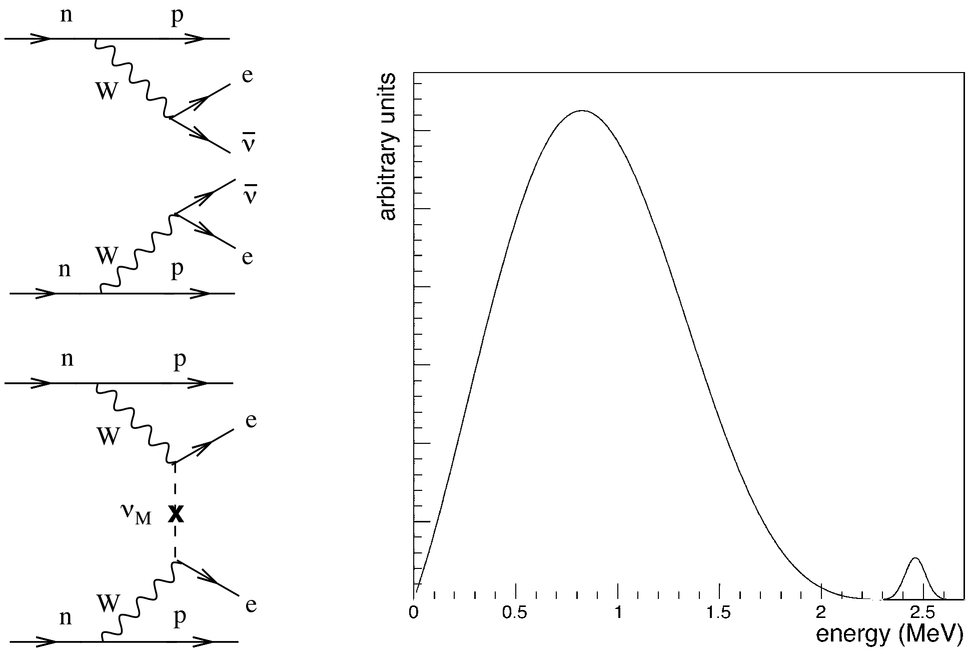

Figure 1.9: Left: Feynman diagrams of a double β-decay. The top diagram shows the lepton number conserving process of two simultaneous β-decays, each omitting an antineutrino. In the bottom diagram, the two emitted neutrinos annihilate with each other, leading to the lepton number violating ($\Delta L = 2$) process of a neutrinoless double β-decay [72]. Right: The golden signature of a neutrinoless double β-decay. The large peak at lower energies shows the continuous energy spectrum of the two-neutrino double β-decay. The small peak at the endpoint of the energy spectrum arises from neutrinoless double β-decay, where the full binding energy is released in the detector through the electrons.

where G is a known phase space factor, $|m_{ee}|^2 = |\sum_i U_{ei}^2 m_i|$ is the squared measured mass, and $\mathcal{M}$ is the nuclear $0\nu 2\beta$ matrix element, suffering from a sizable theoretical uncertainty. The 99% C.L. are plotted in the right plot of Figure 1.7.

1.5.3 The Seesaw Mechanism

The seesaw mechanism is a popular theory for explaining the small and non-vanishing mass of neutrinos. The basic idea is to formulate a renormalizable theory where the lightness of the neutrinos arise from the heaviness of a partner above the electroweak scale ($M > M_W$), which is depicted here very briefly.

In the SM all fermions, except neutrinos, get masses through renormalizable Yukawa couplings with the Higgs doublet $\phi = (\phi^+, \phi^0)^T$, and their corresponding mass terms break the $SU(2)_L$ gauge symmetry as a doublet. In contrast, Majorana neutrino mass terms, such as

$$\mathcal{L} = -\overline{l_L}\,\mathbf{m}_l\, l_R - \frac{1}{2}\nu_L^T C\,\mathbf{m}_\nu\,\nu_L + \frac{g}{\sqrt{2}}\overline{l_L}\gamma_\mu \nu_L W^\mu + \text{H.c.},$$

break $SU(2)_L$ as a triplet, and therefore needs a different mechanism of creation.

The next best solution to this problem is to introduce a dimension-five operator of the form

$$\mathcal{O} = (\ell_\alpha \phi)(\ell_\beta \phi)/M,$$

where $\ell = (l_L, \nu_L)$ is the SM lepton doublet [73]. Now, a non-zero vacuum expectation value of the Higgs $\langle \phi^0 \rangle = v$ gives rise to Majorana neutrino masses proportional to v^2/M, in contrast to the other SM fermions, which are linear in v. If the mass scale M is much higher than the electroweak breaking scale v, neutrinos can naturally get much lower masses than the other SM fermions.

In the seesaw mechanism, the operator $\mathcal{O}$ is induced by the exchange of a heavy particle with a mass scale M. The three most popular realizations of such a heavy state in the seesaw mechanism are:

- Type I: heavy fermions as mediators, which are singlets (ν_R) under $SU(3) \times SU(2) \times U(1)$ gauge symmetry [74, 75, 76, 77].
- Type II: SU(2)-triplet scalars (Δ) as mediators [78, 79, 80, 81, 82].
- Type III: SU(2)-triplet fermions (Σ) as mediators [83].

The corresponding Feynman diagrams are shown in Figure 1.10. The details of these processes can be found in the cited articles.

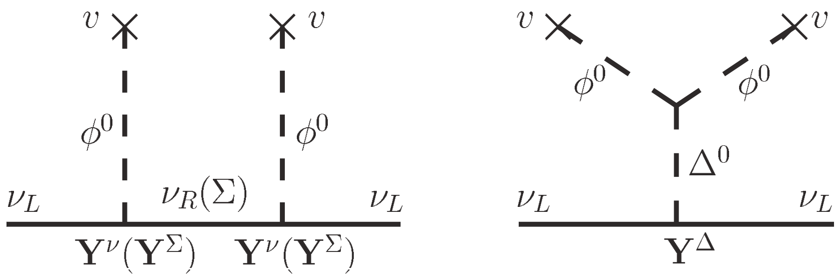

Figure 1.10: Diagrams of the seesaw mechanism for neutrino mass generation. The left diagram corresponds to Type-I and Type-III seesaw masses, mediated by singlet (ν_R) and triplet (Σ) fermions, respectively. The right diagram shows the generation of Type-II seesaw masses via the exchange of a triplet scalar Δ [84].

1.6 The Future of Neutrino Oscillation Physics

One of the major breakthroughs in neutrino physics of 2011 was the indication of a finite mixing angle θ_{13} from several experiments (T2K [2], MINOS [3] and Double-Chooz [4]). Global fits to the data revealed a 3σ[e] evidence for non-zero

[e]The author adopts the PDG convention [16] that probabilities can be expressed in terms of σ, where 1σ corresponds to the standard error interval (68.27%) of a Gaussian distribution. Accordingly, 3σ is just another name for a 99.973% confidence interval.

θ_{13} [85, 86], although the significance is reduced when paying attention to the sign of θ_{13} [87]. If θ_{13} turns out to be as large as the best fit value ($\sin^2\theta_{13} \approx 0.02$) for current data suggests, then there is a good chance to explore CP violation in the leptonic sector during the next years. If there really is leptonic CP violation (LCPV), this could be a mechanism which will help explain the matter excess over antimatter in our universe through the process of leptogenesis.

But not only research on leptonic CP violation profits from a large value of θ_{13}, also the chances to measure the neutrino mass hierarchy and the exploration of the absolute neutrino mass gain from an enhanced $\nu_\mu \to \nu_e$ oscillation. Combining the results of reactor and accelerator experiments could even lead to a test of CPT conservation by comparing the oscillation probabilities for ν_e and $\bar{\nu}_e$ with the help of neutrino factories or β-beams in the future.

1.6.1 Neutrino Factories and β-beams

Two technologies of producing high intensity neutrino beams are currently under investigation: neutrino factories and β-beams. The idea is to accumulate muons or β-decaying nuclei in a storage ring instead of protons, which need to produce pions first before these produce neutrinos.

Neutrino factories aim at exploiting the muon decay (either $\mu^- \to e^- + \nu_\mu + \bar{\nu}_e$ or $\mu^+ \to e^+ + \bar{\nu}_\mu + \nu_e$). Muons, produced from pions, are collected in a storage ring and can be accelerated. Oscillations of the neutrinos from the decaying muons can then be detected by the "wrong signed muons" at the far site. This means that the μ^+ decays into a ν_e which can oscillate into a ν_μ. The muon neutrino then produces a μ^- (the wrong signed muon), which needs to be distinguished in a magnetized far detector from the μ^+ generated from the unoscillated $\bar{\nu}_\mu$. The analogous mechanism works for the μ^--decay. Since both channels $\nu_\mu \leftrightarrow \nu_e$ and $\bar{\nu}_\mu \leftrightarrow \bar{\nu}_e$ can be studied, this is a strong technique to look for CP violation.

The β-beam technology follows the same idea, but instead of muons, β-decaying nuclei are stored. In this way, high intense ν_e or $\bar{\nu}_e$ beams can be produced to search for $\nu_e \to \nu_\mu$ or $\bar{\nu}_e \to \bar{\nu}_\mu$ oscillations, respectively. The advantage is that the far detector does not need to be magnetized. However, the technological barrier of producing and storing a large number of ions to get intense enough neutrino beams needs to be overcome.

1.6.2 Measuring θ_{13}

In July 2011, the T2K collaboration reported an indication of a non-zero value for θ_{13} [2]. The far detector, Super-Kamiokande, observed 6 electron neutrino event candidates from an intense off-axis muon neutrino beam. The beam is produced 295 km away with the energy and the off-axis angle tuned to a maximum signal to background ratio for $\nu_\mu \to \nu_e$ oscillations. 1.5 ± 0.3 events are expected in a three-flavor neutrino oscillation scenario with $|\Delta m^2_{23}| = 2.4 \times 10^{-3}\,\mathrm{eV}^2$, $\sin^2 2\theta_{23} = 1$ and $\sin^2 2\theta_{13} = 0$. This includes the background, such as the misinterpretation of π^0 from a NC interaction as e^- signals in the Super-Kamiokande detector or the intrinsic ν_e contamination of the muon neutrino beam. Applying Poisson statistics, this leads to a 2.5σ significance for $\theta_{13} \neq 0$, which is a strong indication for $\nu_\mu \rightarrow \nu_e$ oscillations.

Similar hints for a non-zero value of θ_{13} come from the first measurements of the Double-Chooz experiment [4]. In contrast to T2K, Double-Chooz is a reactor experiment which explores ν_e disappearance at MeV energies. Anti-electron-neutrinos in the MeV energy region are produced in the fissions of the Chooz nuclear power plant. The 1.05 km far detector of Double-Chooz recorded 4121 events, while the theoretical expectation without oscillations are 4344 ± 165 events, which rules out the no-oscillation hypothesis at the 94.6% confidence level.

These and the results from other experiments, such as MINOS [3] and Chooz [4], and the established results in the solar and atmospheric sector, were included in two global fit analyses. Both conclude that current data suggests that θ_{13} is non-zero at a 3σ significance level. As shown in Figure 1.11, the first analysis finds a best fit value $\sin^2\theta_{13} = 0.021 \pm 0.007$, or $\sin^2\theta_{13} = 0.025 \pm 0.007$ for newly calculated reactor flux systematics [85]. This differs slightly from the results of the second analysis (Figure 1.12), which obtains $\sin^2\theta_{13} = 0.013^{+0.007}_{-0.005}$ for normal and $\sin^2\theta_{13} = 0.016^{+0.008}_{-0.006}$ for inverted hierarchy [86]. For the next years, a quick improvement on the errors of these values is expected, since the reactor experiments RENO [88] in Korea and Daya-Bay [89] in China are about to start taking data. Also an improvement of the T2K flux and more statistics from Double-Chooz will help in further constraining the value of θ_{13} soon. A value of $\sin^2\theta_{13} \gtrsim 0.01$ opens the possibility to explore new physics, such as leptonic CP violation, within the next years with currently known technological solutions.

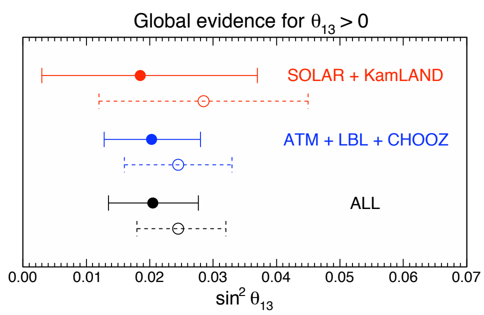

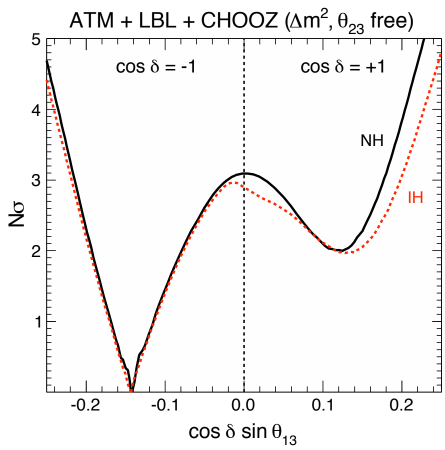

Figure 1.11: Left plot: Global 3ν analysis. Preferred $\pm 1\sigma$ ranges for the mixing parameter $\sin^2\theta_{13}$ from partial (δm^2_{12}-sensitive data labeled "Solar+KamLAND", δm^2_{23}-sensitive data labeled "ATM+LBL+CHOOZ") and global data sets (ALL). Solid and dashed error bars refer to old and new reactor neutrino fluxes, respectively. Right plot: Standard deviations from the best fit in terms of the variable $\cos\delta \sin\theta_{13}$ for the two CP parities ($\cos\delta = \pm 1$) and for both normal hierarchy (NH) and inverted hierarchy (IH), using the ATM+LBL+CHOOZ data set [85].

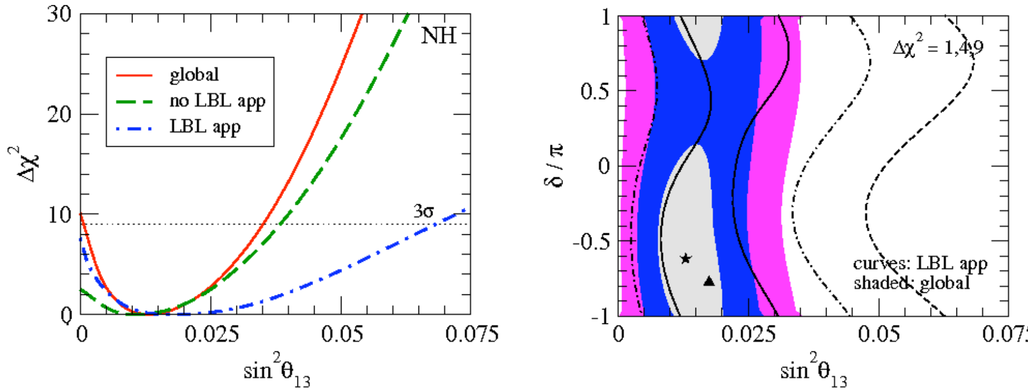

Figure 1.12: Left panel: $\Delta\chi^2$ as a function of $\sin^2\theta_{13}$ for T2K and MINOS ν_e appearance data ("LBL app"), all the other global data ("no LBL app"), and the combined global data ("global"). Right panel: contours of $\Delta\chi^2 = 1, 4, 9$ in the $\sin^2\theta_{13} - \delta$ plane for "LBL app" (curves) and for the global data (shaded regions). Only the results for normal hierarchy are shown [86].

1.6.3 Leptonic CP Violation

CP violation is well established in the quark sector, which was observed in K- and B-meson decays [23, 24], corresponding to a complex CKM matrix. An analogous behavior is expected in the leptonic sector, which can be nicely studied through neutrino oscillations, providing the relevant parameters are not too small to be observable and that possible degeneracies can be overcome (see Figure 1.13). Because of the neutral charge of neutrinos, it is possible that neutrinos, unlike quarks, are of Majorana type, which manifests in two additional CP violating phases $\alpha_{1,2}$ in the PMNS matrix. Up to now, there is no unambiguous evidence for the existence of Majorana type neutrinos. Nevertheless, Majorana type neutrinos are interesting from a theoretical viewpoint, as they might help to explain the smallness of neutrino masses through the seesaw mechanism and are used in the simplest leptogenesis scenarios.

The most promising way to search for LCPV is through the study of neutrino oscillations, which are sensitive to the Dirac type CP phase parameter δ^{CP} in the PMNS matrix 1.6. As mentioned earlier, a relative high value of the mixing angle θ_{13} helps to establish a statement on the existence of LCPV in the next generation of experiments. Other phenomena which are sensitive to a possible CP violation include the neutrinoless double β-decay and lepton flavor violating decays like $\mu \to e\gamma$ [90]. If the neutrino mass generation happens close to the electroweak scale, also high-energy colliders like the Large Hadron Collider (LHC) at CERN could provide observations of phenomena affected by LCPV.

In this thesis, a general picture of the prospects for discovering LCPV in future neutrino oscillation experiments is only briefly outlined. But there are several publications which deal with LCPV and possible future experiments in more detail, a nice overview is given in [84]. Writing down Equation 1.5 for $\nu_e \leftrightarrow \nu_\mu$ oscillations

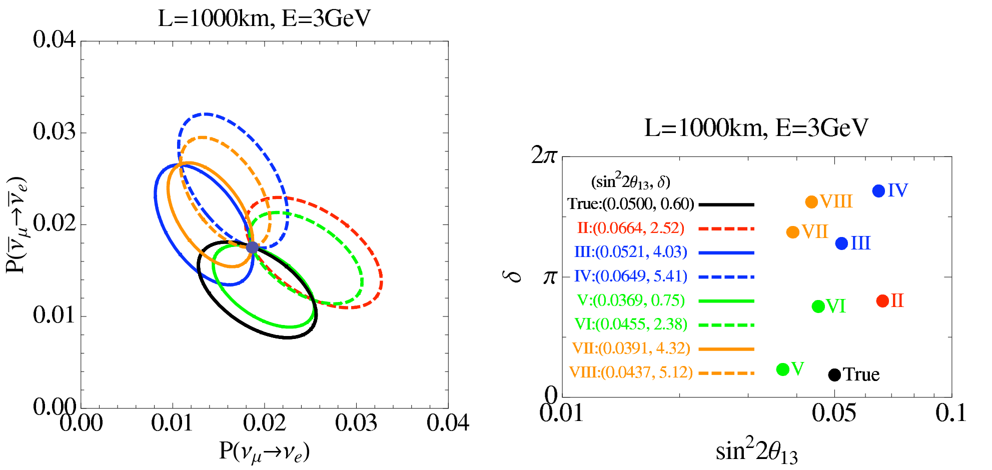

Figure 1.13: Left panel: An illustrative example of the eightfold degeneracy in terms of the bi-probability plot in $P_{\mu e} - \bar{P}_{\mu e}$ space. Right panel: Values of $(\sin^2 2\theta_{13},\, \delta^{CP})$ for the true solutions and the clone solutions II-VIII in $\sin^2 2\theta_{13} - \delta^{CP}$ space. The correspondence between the ellipses (top panel) and the solution labels are made clear by using the same color lines and symbols in both panels [93].

leads to

$$\Delta P^{CP}_{e\mu} = \Delta P^{CP}_{\mu\tau} = \Delta P^{CP}_{\tau e} = \Delta P^{CP} = 4\Im^{12}_{e\mu}(\sin\Delta_{21} + \sin\Delta_{32} + \sin\Delta_{13}).$$

This equation implies that there is no CP violation if one of the mixing angles is zero ($\Rightarrow \Im^{12}_{e\mu} = 0$) or if two or more neutrino masses are degenerate ($\Delta_{kj} = 0$, if $m_k = m_j$). Also, because of $P_{\alpha\alpha} = \bar{P}_{\alpha\alpha}$ under CPT invariance, LCPV cannot be observed in disappearance channels. Furthermore, experiments need to be sensitive to the relevant parameters, which requires L and E to be chosen such that at least one of the phases Δ_{kj} is of the order one.

However, a non-zero measurement of ΔP^{CP} does not automatically imply CP violation, because matter effects in neutrino propagation can fake CP violation, since only ν_e but not $\bar{\nu}_e$ contribute to the MSW resonance. But the two effects show a different behavior with respect to L/E, such that the combination of data from two experiments with either different base lengths or energies can help to reveal the true effect. For details see for example [91, 92].

Further degeneracies are possible, which can lead to an eightfold degeneracy in the worst case. This complicates the measurement of the different, yet unknown, oscillation parameters δ^{CP}, θ_{13}, the sign of Δm^2_{31}, and whether θ_{23} is maximal mixing or not. Namely, the three twofold degeneracies are a $(\delta^{CP}, \theta_{13})$-ambiguity, a $sign(\Delta m^2_{31})$-ambiguity and a $(\theta_{23}, \pi/2 - \theta_{23})$-ambiguity. Each possible set of parameters leads to an ellipse in the $(P, \bar{P})$ bi-probability space, and the degeneracies can be understood as the intersection points of these ellipses, as it is illustrated in Figure 1.13.

1.6.4 Leptogenesis

One of today's unsolved questions in physics is the excess of matter over antimatter, which is inferred from the observation of the Big Bang Nucleosynthesis [94] and anisotropies in the Cosmic Microwave Background (CMB) [95].This excess is usually captured in the baryon asymmetry parameter

$$\eta = \frac{n_B - n_{\bar{B}}}{n_\gamma} \simeq (6.21 \pm 0.15) \times 10^{-10}.$$

Three possible explanations have been examined. The asymmetry coming from initial conditions, baryogenesis and leptogenesis.

The hypothesis of an asymmetry coming from initial conditions is regarded unlikely, since it requires a strong fine tuning of parameters and an initial asymmetry of 10^{-7} to explain the observed effect. Moreover, in a universe with inflation (which is widely accepted to be the case), all initial asymmetries would have been erased in the inflationary phase.

Another possible explanation is the excess to be the result of a dynamical evolution with the assumption of a complete symmetry in the initial conditions of the Big Bang. Sakharov [96] formulated three necessary conditions that need to be fulfilled to allow this explanation:

1. The baryon number is violated.
2. C- and CP-symmetry are violated.
3. Departure from the thermal equilibrium.

The first condition is necessary to allow deviation from total symmetry (B=0). The second condition needs to be fulfilled, because otherwise the rate of a process which produces an excess of baryons is equal to the rate of the complementary process which produces an excess of antibaryons, such that the net baryon number does not change [97]. From the definition of C, P and T transformations acting on quark fields, one obtains:

$$C\hat{B}C^{-1} = (CP)\hat{B}(CP)^{-1} = (CPT)\hat{B}(CPT)^{-1} = -\hat{B}.$$

At thermal equilibrium, the Boltzmann distribution dictates that there should be equal amounts of matter and antimatter. Other processes will turn any baryon asymmetry back into even numbers of baryons and antibaryons. Thus, any baryogenesis must happen under conditions outside of thermal equilibrium:

$$\begin{aligned}\langle\hat{B}\rangle_T &= Tr(e^{-\beta H}\hat{B}) = Tr((CPT)(CPT)^{-1}e^{-\beta H}\hat{B}) = Tr((CPT)e^{-\beta H}(CPT)^{-1}\hat{B}) \\ &= Tr(e^{-\beta H}(CPT)^{-1}\hat{B}(CPT)) = Tr(e^{-\beta H}(-\hat{B})) = -Tr(e^{-\beta H}\hat{B}) = -\langle\hat{B}\rangle_T,\end{aligned}$$

where the Hamiltonian H commutes with CPT. Thus, we obtain $\langle B\rangle_T = 0$ in thermal equilibrium and no baryon excess is produced.

The Sakharov conditions are compatible with the Standard Model and realized in nature. At today's temperatures in the universe, B and L are accidentally conserved, in fact, only the quantity B-L is conserved while B+L is not. But at high temperatures ($\gtrsim 10\,\text{TeV}$, the so-called sphaleron mass) in the early universe, the transition from leptons to baryons can be explained with the help of sphalerons [98]. Sphalerons are unstable solutions in the electroweak theory and describe the transition between two vacuum states. Such a transition process requires nine right-handed quarks (three colors for each generation) and three right-handed leptons (for each corresponding generation). In a sense, this process generates a baryon excess out of a lepton excess. The violation of C- and CP-symmetry in the CKM matrix has been discussed in previous sections. However, the extent of the observed violation in the weak sector is not large enough to explain the full baryon asymmetry. Finally, the out-of-equilibrium temperature is the electroweak phase transition ($\sim 100\,\text{GeV}$). When the universe cools down below this temperature, possible asymmetries can be "frozen in". Specifically, this means that baryon-generating processes, such as the sphaleron process, occur at the interphase, and due to CP violation baryon generation dominates over the conjugate process. These asymmetries are "frozen in" when cooling below the transition temperature and the sphaleron mass. But this process can only explain an asymmetry of $\eta \simeq 10^{-20}$.

Besides physics at the GUT-scale[f] ($\sim 10^{16}\,\text{GeV}$) or the Planck-scale[g] $\sim 10^{19}\,\text{GeV}$ with energies that are not feasible for testing in the laboratory, leptogenesis is a mechanism which could explain the baryon asymmetry. The idea is that, through a yet to be specified mechanism, a large lepton excess is created and then is propagated to a baryon excess through B-L conserving processes. Since CP violation in the leptonic sector is not as constrained as in the quark sector, this mechanism could be held account for the observed asymmetry.

In its simplest realization, new heavy particles are introduced, such that the interactions relevant for leptogenesis are simultaneously responsible for smallness of the neutrino masses via the seesaw mechanism. Since the seesaw mechanism requires lepton number violation, the first Sakharov condition can be fulfilled through sphaleron transitions to baryon violation. The complex Yukawa couplings of the neutrino provide the necessary C and CP violation. And the departure from thermal equilibrium is guaranteed by the out-of-equilibrium decays of the new heavy particles.

[f] Grand unified theories (GUT) are models which predict the unification of the strong, weak and electromagnetic forces above a certain energy threshold, a mechanism similar to the electroweak unification.

[g] The Planck-scale is the energy range, at which quantum effects of gravity start playing a significant role, such that quantum field theories do not hold anymore. It is theorized that all four forces are unified at this energy scale, but the exact mechanisms are still unknown.

Chapter 2

The T2K Experiment

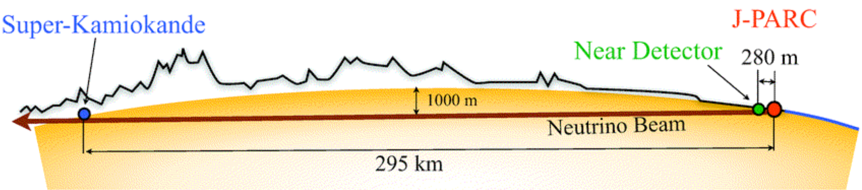

Figure 2.1: A schematic view of the T2K baseline. Neutrinos are produced at J-PARC in Tokai and travel 295 km to the Super-Kamiokande detector in Kamioka [99].

The T2K (Tokai-to-Kamioka) experiment [99, 100] in Japan is a second generation long base line neutrino oscillation experiment that probes physics beyond the Standard Model. It aims at performing high precision measurements of neutrino mixing and also hopes to shed a light on the neutrino mass scale. A high intensity narrow band neutrino beam is produced via the decay of secondary pions created by an intense proton beam at the Japan Proton Accelerator Research Complex (J-PARC). With the help of the off-axis neutrino beam technique the neutrino energy is tuned to the oscillation maximum at $\sim$0.6 GeV for a baseline length of 295 km towards the world largest water Čerenkov detector, Super-Kamiokande [101]. Its excellent energy resolution and particle identification enable the reconstruction of the initial neutrino energy, which is compared with the narrow band neutrino energy, through quasi-elastic interactions.

The physics goal of the first phase is an order of magnitude better precision in the $\nu_\mu \to \nu_x$ disappearance oscillation measurement ($\delta(\Delta m^2_{23}) \lesssim 10^{-4}\,\text{eV}^2$ and $\delta(\sin^2 2\theta_{23}) \lesssim 0.01$) and the discovery of θ_{13} if it is non-zero or improving the sensitivity on $\sin^2 2\theta_{13}$ by a factor of ten in $\nu_\mu \to \nu_e$ appearance with respect to the CHOOZ limits [46]. T2K allows a confirmation of the $\nu_\mu \to \nu_\tau$ oscillation or discovery of sterile neutrinos by detecting neutral current events, and will provide important input on the study of neutrino interactions at an energy scale of $\sim$1 GeV. Besides quasi-elastic scattering, resonant pion production and deep inelastic scattering build an essential part of the neutrino cross section in this energy region.

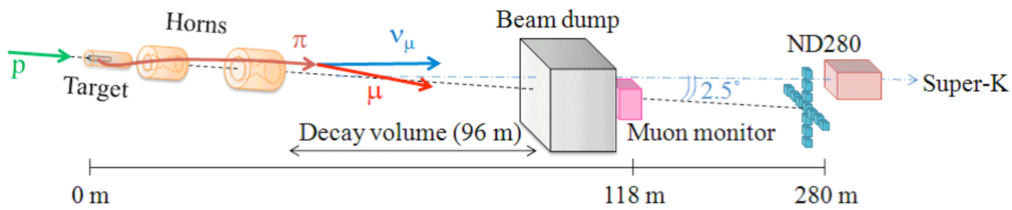

Figure 2.2: A schematic view of the T2K neutrino beamline [104].

In a possible second phase, an upgrade of the accelerator in beam power and the construction of a larger far detector (e.g. a 1 Mton Hyper-Kamiokande detector [102] at the Kamioka site) are envisaged. Another order of magnitude improvement in the $\nu_\mu \rightarrow \nu_e$ oscillation sensitivity allows for a search of CP violation in the lepton sector [84], which might give a hint to the observed matter-antimatter discrepancy in the universe through Leptogenesis [103].

In Figure 2.2 a schematic view of the T2K neutrino beam is drawn. A 30 GeV proton beam impinges on a graphite target and thereby produces secondary mesons, mainly pions and kaons. The pions are focused in a toroidal magnetic field with the help of three magnetic horns, operated with a pulsed current of up to 320 kA. In the subsequent 96 m long decay pipe, the pions mainly decay into muons and neutrinos ($\pi^+ \rightarrow \mu^+ + \nu_\mu$). In the following 75 ton graphite beam dump, all particles are stopped; except neutrinos and high energy muons ($E_\mu \gtrsim 5$ GeV), which are measured by the muon monitor to retrieve information on the beam on a bunch-by-bunch basis. 280 m downstream of the target, the on-axis near detector INGRID and the off-axis detector ND280 analyze the neutrino beam properties. INGRID is an array of scintillator/iron sandwich calorimeters which measures the neutrino beam profile and direction. The magnetized ND280 measures the ν_μ flux and energy spectrum, the intrinsic electron neutrino contamination as well as the exclusive neutrino interaction rates. These inputs are essential to characterize signal and background in the Super-Kamiokande detector.

2.1 The Beamline at J-PARC

The T2K beamline (see Figure 2.3) consists of a linear accelerator (LINAC), the Rapid Cycle Synchrotron (RCS), the Main Ring synchrotron (MR), and the primary as well as the secondary neutrino beamline. In the primary beamline the extracted protons from the Main Ring are directed onto a graphite target where secondary pions are produced. In the secondary beamline these pions are focused by three magnetic horns [105]. In the subsequent decay pipe, the pions decay predominantly into muons and neutrinos, which form the T2K neutrino beam towards Kamioka. The off-axis angle with respect to Super-Kamiokande can be tuned from the current setting of 2.5° down to 2.0° to allow for tuning the beam towards optimal oscillations probabilities. An overview of the T2K neutrino beamline is given in Figure 2.4. This section summarizes the functionality of the beamline which is described in more detail in [99].

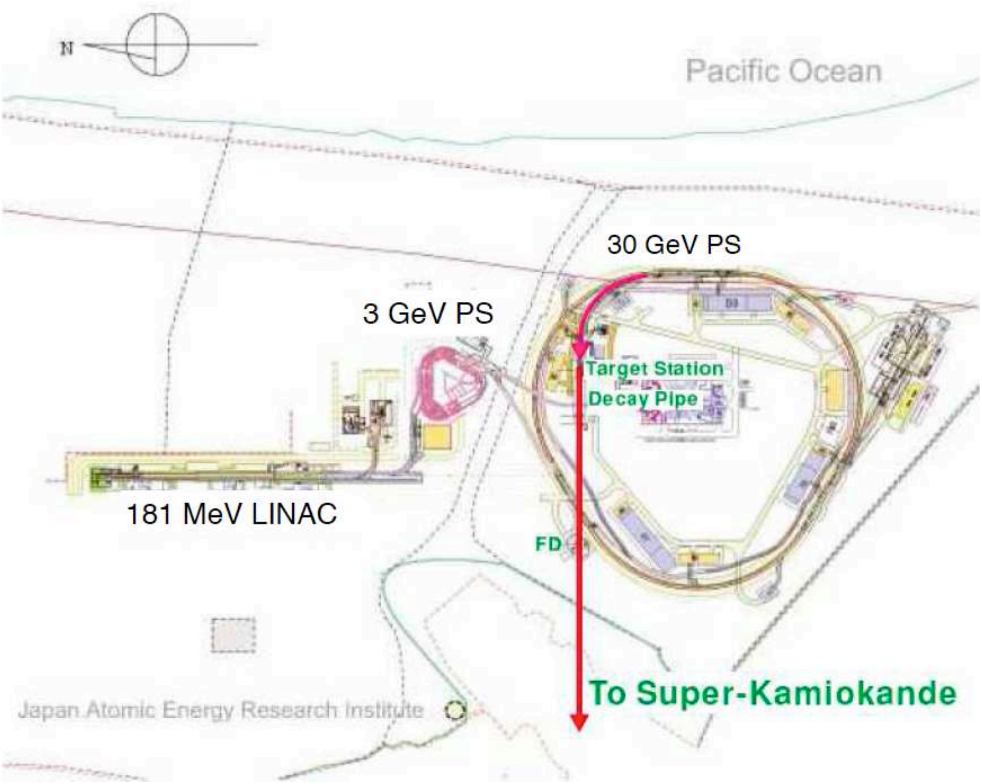

Figure 2.3: Overview of the T2K beamline at J-PARC [100].

2.1.1 J-PARC Accelerator and Primary Beamline

In the LINAC, an H^- beam is accelerated up to an energy of 181 MeV (upgrade to 400 MeV planned in 2012). After the conversion to H^+ by means of charge stripping foils, the proton energy is increased to 3 GeV in the RCS and finally to 30 GeV in the Main Ring. In the so-called fast extraction mode, the protons in a beam spill consisting of 8 bunches (6 bunches until June 2010) are bent by five kicker magnets in the primary beamline towards the target.

The primary beamline consists of the preparation section, the arc section, and the final focusing section. In the 54 m long preparation section, the beam is tuned with 11 normal conducting magnets such that it can be accepted by the arc section. In the 147 m long arc section, the beam is bent by 80.7° toward the final beam direction (i.e. 3.637° below the horizontal in direction of Kamioka) using 14 doublets of superconducting combined function magnets.

The proton beam needs to be well-tuned to ensure a stable neutrino beam production and is therefore equipped with a series of beam quality monitors. The beam intensity is monitored with an uncertainty of 2% on the absolute intensity and a fluctuation of 0.5% on the relative intensity by five current transformers (CTs), which are 50 turn toroidal coils with a ferromagnetic core.

A series of 21 electrostatic monitors (ESMs) measure the beam center position with a precision of better than 450 μm by exploiting asymmetries in the elec-

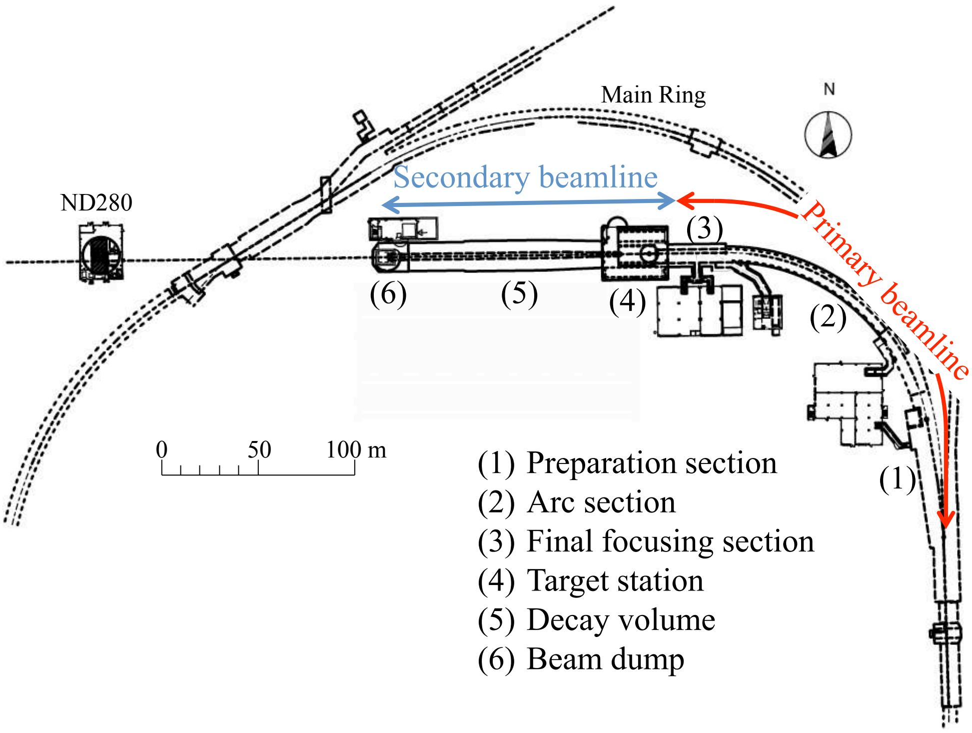

Figure 2.4: Overview of the T2K primary and secondary beamline [99].

tric field induced on four segmented cylindrical electrodes surrounding the proton beam orbit.

At various places along the primary beamline, 50 wire proportional counters filled with an Ar-CO_2 mixture are placed around the beam to monitor beam losses. When the integrated signal during a spill exceeds a threshold value, beam operation will be aborted.

The beam profile is monitored by 19 segmented secondary emission monitors (SSEMs), which are temporarily introduced into the beam during commissioning and extracted from the beam during continuous operation because they reduce the beam intensity by 0.005%. Each SSEM is made of three titanium foils, two of them horizontally and vertically stripped with a HV anode foil in the middle. The proton beam interacts with the foil material and thus produces secondary electrons which drift to the anode and give an indication of the beam profile with a systematic uncertainty of 200 µm on the beam width measurements.

2.1.2 Secondary Beamline

The secondary beamline is separated from the primary beamline by a titanium-alloy beam window. The secondary beamline is placed in a volume of 1500 m^3 filled with helium gas at atmospheric pressure. It includes the target station, a 96 m long decay pipe, and a beam dump (Figure 2.5).

The target station contains the baffle, optical transition radiation monitors (OTR), the target, and three magnetic horns. The baffle is a 1.7 m long graphite

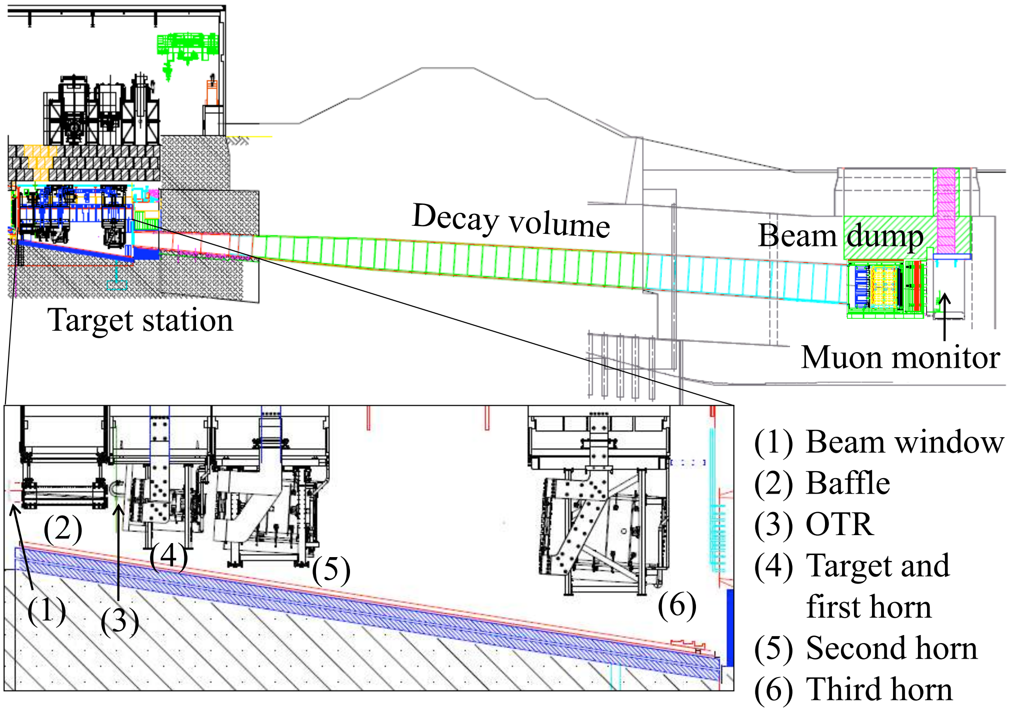

Figure 2.5: Side view of the T2K secondary beamline [99].

block with a hole of 30 mm for the primary proton beam to pass through, and thereby functioning as a collimator to protect the horns.

The purpose of the OTR [106] is to monitor the proton beam in the highly radioactive environment in proximity to the T2K target. It transports transition light from through-passing protons to a lower radiation area where it is possible to operate cameras which capture the light. The OTR measures the proton beam position and width with a precision of better than 500 µm. It consists of a thin titanium-alloy foil which is placed at 45° to the incident proton beam. As the beam enters and exits the foils, transition radiation is produced and reflected at the foil in a 90° angle with respect to the beam direction.

A 91.4 cm long graphite target of 2.6 cm in diameter and a density of 1.8 g cm^{-3} follows the OTR. Besides other hadrons, mainly secondary pions are produced which are collected and focused in the toroidal magnetic fields of the magnetic horns working at a pulsed current of 250 kA (320 kA in the future). When the horns are run with the operation current of 320 kA, the neutrino flux at Super-Kamiokande is increased by a factor of ∼16 at the spectrum peak-energy (∼0.6 GeV).

The pions decay into muons and neutrinos via Lorentz boosted two-body decay in a 96 m long steel tunnel, which is followed by the beam dump. The neutrinos and muons with energies above 5 GeV penetrate the beam dump to reach the muon monitor pit.

2.1.3 Muon Monitor

Downstream to the beam dump, the muon monitor [104, 107] characterizes the neutrino beam on a bunch-by-bunch basis. It measures the profile of the muon distribution and has a precision on the beam center position of better than 3 cm which corresponds to 0.25 mrad. The stability of the beam intensity is known to better than 3%. With 3.3×10^{14} protons per spill, 10^7 charged particles per bunch and cm^2 are expected, composed of 87% muons and 13% from electromagnetic showers. The charge deposition shows a Gaussian profile with a width of 1 m.

The muon monitor consists of two types of detector arrays: a plane of ionization chambers with sensors made of two aluminum ceramic electrodes with 200 V applied between them, and a plane of silicon PIN photo diodes. Each array holds 49 sensors and covers an area of 150 cm × 150 cm.

During beam commissioning, an emulsion tracker was inserted in the muon pit. On a one shot basis the muon flux was determined with 2% uncertainty with the help of a module of eight consecutive emulsion films. A second module of 25 films interleaved by 1 mm lead plates allowed the momentum measurement of each particle via Coulomb scattering with a precision of 28% for muons with a remaining energy of 2 GeV after the beam dump.

2.2 INGRID

The INGRID (Interactive Neutrino GRID) detector is centered on the beam axis and was designed to directly monitor the neutrino beam direction and intensity 280 m downstream of the target with sandwich type iron/scintillator calorimeters. Using the number of observed CCQE neutrino interactions, a precision of better than 10 cm, corresponding to 0.4 mrad, on the beam direction is achieved. INGRID is a 10 m × 10 m cross-shaped detector made of seven horizontal and seven vertical modules with the center modules on the neutrino beam axis. Two additional off-axis modules are installed to check the axial symmetry of the beam. The geometrical setup is shown in Figure 2.6.

Each module has a weight of ∼8 tons and is composed of 11 plastic scintillator planes interleaved with 9 iron plates, all perpendicular to the beam direction. Because of weight restrictions, there is no iron plate between the last two scintillator planes. A scintillator plane consists of two sub-planes, which are made of 24 horizontal bars glued to 24 vertical bars, where each bar has the dimensions 1.0 cm × 5.0 cm × 120.3 cm. Each module is surrounded by four veto planes consisting of 22 bars (compare with Figure 2.6). The scintillator bars are made of polystyrene, doped with 1% PPO and 0.03% POPOP, and produce blue emission light with a peak at 420 nm. A white reflective coating composed of TiO_2 infused in polystyrene is co-extruded. The bars have a 3 mmdiameter hole in the center to insert wavelength shifting (WLS) fibers. The WLS fibers have a diameter of 1 mm with their absorption and emission spectrum centered around 430 nm and 467 nm, respectively, with only a small overlap between the two spectra, thereby reducing self-absorption effects. A multi-pixel photon counter (MPPC) is attached to each fiber by a connector glued to the fibers. The scintillator planes, WLS fibers and

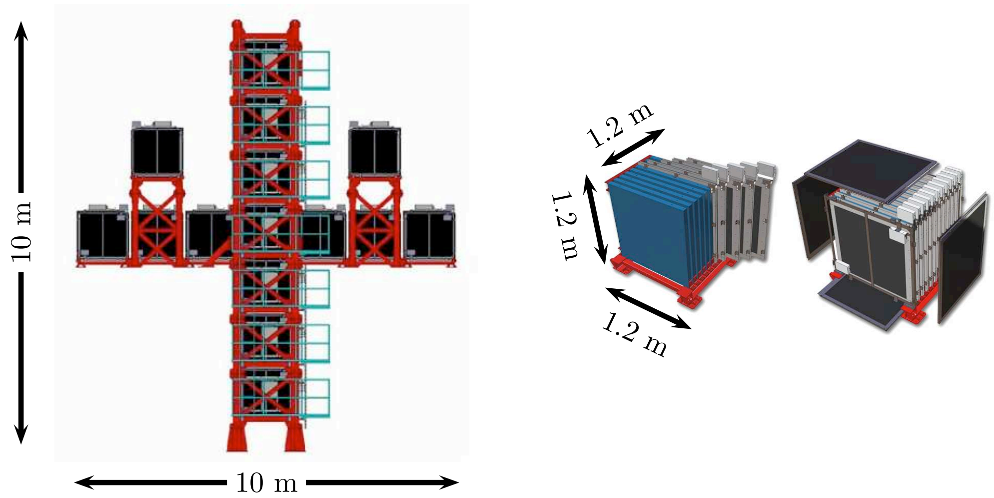

Figure 2.6: The left image shows the INGRID on-axis detector. An INGRID module is shown in the two right images. The middle image shows the tracking planes (blue) and iron plates (gray). In the right image the veto planes (black) are shown [99].

MPPCs are placed in a light-tight dark box made of a aluminum structure and plastic plates. The front end readout boards, Trip-T frontend boards (TFBs), are mounted outside the dark box and each is connected to 48 MPPCs via coaxial cables. In total, INGRID has 9,592 readout channels.

INGRID was calibrated with cosmic ray and beam data. The mean light yield is greater than 10 photo electrons per 1 cm MIP track length, and the time resolution for each channel is 3.2 ns.

In addition to the 16 standard modules, the so-called proton module is placed between the two center modules of the INGRID cross. It holds no iron plates and is built to detect muons and protons from CCQE interactions with good efficiency for comparison with Monte Carlo simulations of the beamline particle propagation and neutrino interactions.

More details on the construction, performance and first physics results of the INGRID detector can be found in [108].

2.3 ND280 Off-axis Detector

The ND280 off-axis detector (Figure 2.7), or ND280, is located 280 m downstream of the target in the direction of Super-Kamiokande, i.e. 2.5° off-axis. Its purpose is to measure neutrino beam properties prior to oscillation, such as the neutrino flux and spectrum and the electron neutrino contamination of the muon neutrino beam. Also, ND280 is designed to study neutrino interaction cross sections and reconstruct exclusive event types, which is important to constrain possible background processes for Super-Kamiokande, such as neutral current π^0 events. While the characterization of the muon neutrino flux is an important input for the disappearance analysis, the energy dependent study of electron neutrinos is essential

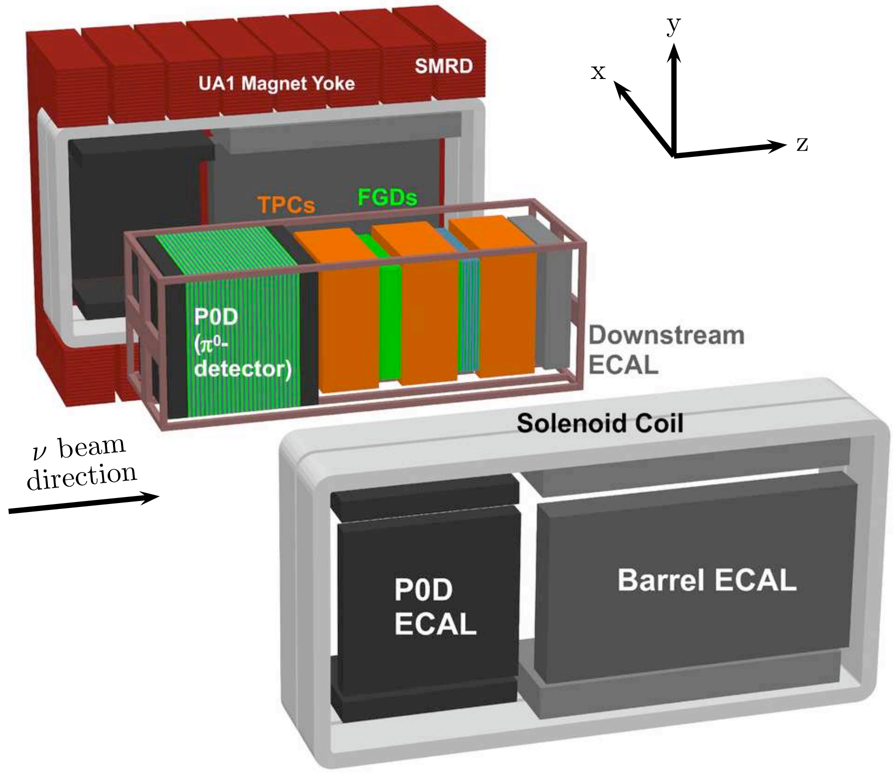

Figure 2.7: An exploded view of the ND280 off-axis detector with magnet outer dimensions of 5.6 m × 6.1 m × 7.6 m.

for the electron neutrino appearance.

To perform these functions, ND280 is divided in several sub-detectors which will be explained in more detail in the following subsections. All sub-detectors are placed in a uniform magnetic field of 0.2 T. Most upstream is the π^0 detector (PØD) which is optimized for the reconstruction of neutral current interactions. It is followed by the tracker which is composed of two finely grained detectors (FGDs) and three time projection chambers (TPCs). The tracker is ideal for the study of charged current events. PØD and tracker are surrounded by an electromagnetic calorimeter (ECal) and side muon range detectors (SMRD) within the magnet yoke.

2.3.1 ND280 Magnet

The magnetic field for ND280 is generated by the former UA1/NOMAD [109, 110] dipole magnet which was refurbished at CERN and shipped to J-PARC in 2008. The 16 C-shaped flux return yokes, made of low carbon steel plates for a total weight of 850 tons, define the magnet outer dimensions of 5.6 m × 6.1 m × 7.6 m. The magnet is mirror symmetric and the two halves can be moved on rails to allow access to its inner volume.

For the T2K experiment, a 0.2 T uniform magnetic field is generated by four water-cooled aluminum coils with a total of 208 turns at a current of 2900 A. This magnetic field allows the identification and momentum determination of charged particles in the ND280 sub-detectors (in particular in the TPCs) contained in the magnet. The design of the coils, with a hole at the up- and downstream end of the magnet allows to place the basket - a support frame made out of stainless steel holding most of the sub-detectors of ND280.

A measurement campaign with a dedicated mapping device was performed in September 2009 in order to map the magnetic field with an accuracy of the order of 1 G. More details about this are given in Chapter 3.

2.3.2 Pi-zero Detector (PØD)

The primary goal of the PØD is to measure NC π^0 production ($\nu_\mu N \rightarrow \nu_\mu N' \pi^0 X$) for neutrino interactions on H_2O with the same muon neutrino flux as at Super-Kamiokande. The PØD is made of four sections (so-called Super-PØDules), the“upstream ECal” followed by the“upstream water target”, the “central water target” and the “central ECal”, as shown in Figure 2.8. The combination of 134 2.2 m long vertical and 126 2.34 m long horizontal triangular scintillator bars form a PØD module, or PØDule. Seven PØDules alternate with 0.4 mm thick lead sheets in the case of the two ECal sections, and for the two water target sections 13 PØDules are interleaved with 28 mm thick water bag layers followed by a 1.5 mm thick brass sheet. This design improves the containment of electromagnetic showers from photon conversion and provides a veto region before and after the water target to reject particles entering from outside the PØD.

The doped polystyrene scintillator bars with a TiO_2 reflective layer have a central hole for WLS fibers (1 mm in diameter). The collected light is mirrored at one end of the bars and read out with MPPCs at the other end, which transfer the signal to the TFBs. The signals from the overall 10,400 channels are transfered to the ND280 DAQ system.

The water bags can be filled or empty, which allows a subtraction method for the neutrino H_2O cross section determination. The total water mass is 1902±16 kg, measured with two type of sensors. Binary level sensors (wet/ dry) and pressure sensors allowing to determine the water depth with a precision of 5 mm. Further information on the design, performance and first results using the PØD can be found in [111].

2.3.3 Time Projection Chambers (TPCs)

The time projection chambers (TPCs) have three key functions. Firstly, they provide the number and orientation of charged particles, therefore allowing to reconstruct different neutrino interaction types with high purity. Secondly, by measuring the curvature of charged particle tracks, they determine the particle momentum. This enables the study of the neutrino interaction rate as a function of neutrino energy prior to oscillation. Finally, the deposited energy via ionization in combination with the momentum information give a strong tool for identifying the different types of particles.

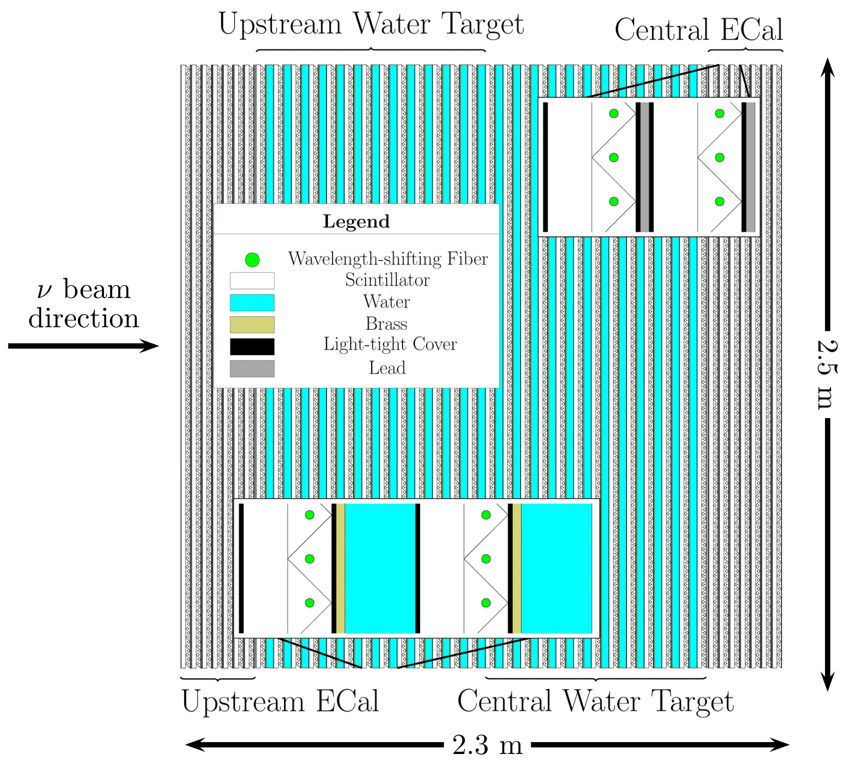

Figure 2.8: PØD schematic view of the four Super-PØDules and their composition as installed in ND280 [111].

Each of the three TPCs has outer dimension 2.3 m × 2.4 m × 1.0 m and consists of an inner box with an argon-based drift gas ($Ar{:}CF_4{:}C_4H_{10}$, 95:3:2) contained in an outer box that holds CO_2 as insulating gas. The inner volume is held under overpressure with respect to the outer gas volume which in turn is set to positive pressure with respect to the atmosphere to prevent impure gas from streaming in.

The inner box panels are precisely machined to form an 11.5 mm pitched copper strip pattern, which together with the central copper cathode provides a uniform electric field roughly aligned with the magnetic field direction of the ND280 magnet. Ionization electrons drift along the electric field towards the readout planes at the two ends of the TPC in positive and negative x-direction, where the charge is amplified by bulk micromegas detectors [113] with a 7.0 mm × 9.8 mm pad segmentation. The signal pattern at the anode pads in combination with the arrival time allow a 3D imaging of charged particle trajectories within the TPC. Two vertical columns of six 342 mm × 359 mm micromegas modules form a readout plane for a total of 72 micromegas modules. The columns are slightly offset in vertical direction such that the inactive regions between the modules in a single readout plane are not aligned.

A calibration system uses diffuse light of a 266 nm laser to illuminate small aluminum discs which are glued to the central cathode surface. The emerging photo electrons provide a control pattern which is used to precisely determine the electron drift velocity and to measure distortions because of inhomogeneous and

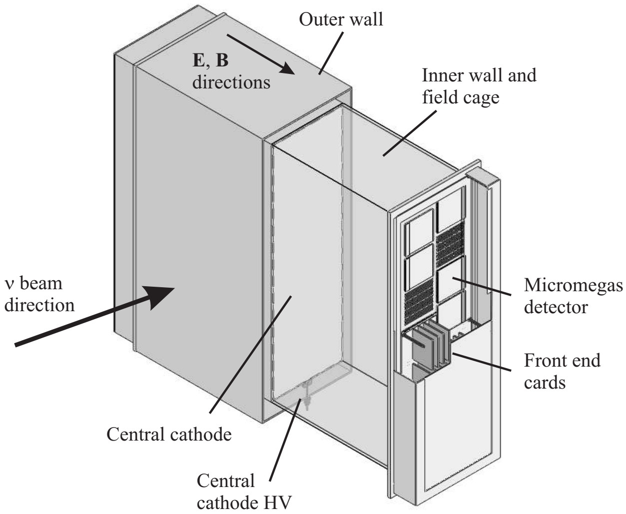

Figure 2.9: Simplified cut-away drawing showing the main aspects of the TPC design with outer dimensions 2.3 m × 2.4 m × 1.0 m [112].

misaligned electric and magnetic fields.

The TPC perform an excellent particle identification (PID), which uses a truncated mean of the energy loss of a particle, taking the lowest 70% of the energy loss into account. This value was optimized with the help of Monte Carlo simulations and test beam studies. This results in an energy deposit resolution of 7.8% for minimal ionizing particles (MIPs), while the point spatial resolution is determined to be 0.7 mm per column by comparison of the transverse coordinate from the global track fit to information obtained from a single column of pads.

More detailed information about the design, construction and the performance of the TPCs can be found in [112].

2.3.4 Fine Grained Detectors (FGDs)

Two fine grained detectors (FGDs) interleave the three TPCs, whose purpose is to provide a target mass for neutrino interactions as well as the tracking of charged particles from the vertex. Moreover, the design of the first FGD being made of scintillators only and the other as a sandwich of scintillator and water allows a comparison of neutrino cross sections on carbon and water.

Each FGD has outer dimensions 2300 mm × 2400 mm × 365 mm and a target mass of 1.1 tons and is constructed from 9.61 mm × 9.61 mm × 1864.3 mm polystyrene scintillator bars with a TiO_2 coating and a central hole, in which WLS fibers are inserted. The light signal is mirrored on one end of a bar and read out by an MPPC at the other end. The first FGD is built of 30 layers of 192 bars each. The bars are orthogonally oriented in successive planes, such that each pair of orthogonal layers builds an XY module perpendicular to the neutrino beam. The second FGD is made of seven XY modules interleaved with 2.5 cm thick water layers at sub-atmospheric pressure[a]. Each FGD is surrounded by a light tight dark box on which the readout electronics for the 42 so-called mini crates, which contain 4 front end boards each, are mounted.

2.3.5 Electromagnetic Calorimeter (ECal)

An electromagnetic calorimeter surrounds the PØD and the tracker to measure photons, primarily from π^0 production. It also helps to distinguish electrons, muons and pions in addition to the TPC dE/dx particle identification.

The ECal is tiled in 13 modules and each is built from a sandwich of scintillators and lead sheets. The scintillator bars are made of doped (1% POP and 0.03% POPOP) polystyrene with a TiO_2 reflective coating and a 1 mm in diameter WLS fiber inserted in a central hole. The bars have a 4 cm × 1 cm cross section and vary in length depending on the module they belong to. The scintillation light from each bar is read out by one or two MPPCs depending on the length of the bar.

The downstream module (Ds-ECal) is placed perpendicular to the neutrino beam inside the basket at the downstream end. It consists of 34 layers with 1.75 mm thick lead sheets corresponding to 10.6 X_0[b]. 50 bars of 2.04 m length form a layer, and the orientation alternates between x and y in successive layers.

The tracker is surrounded by six modules (Barrel-ECal) along the z-axis, which is formed of 31 layers at each side corresponding to 9.7 X_0. On the sides a layer of 3.84 m long bars (two-sided readout because of their length) in z-direction alternates with a layer of 2.36 m long bars in y-direction. On the top and bottom the z layers alternate with x layers of 1.52 m long bars.

Also the PØD is surrounded by six modules (PØD-ECal) parallel to the beam direction. Since photon conversion is happening mainly inside the PØD volume, the PØD-ECal's main tasks are to serve as a veto for entering particles and tag muons and gammas that escape the PØD without being reconstructed. For these purposes, a reduced granularity with six scintillator planes containing 2.34 m long bars always oriented in z-direction interleaved by 4 mm lead sheets is sufficient.

2.3.6 Side Muon Range Detector (SMRD)

The side muon range detector (SMRD) provides energy measurements of muons which escape from the inner sub-detectors at high angles with respect to the beam. It also serves as a trigger for cosmic ray muons, and can veto beam related interactions in surrounding walls and the ND280 magnet yoke. The SMRD consists of 440 scintillator planes in total, which equip the 1.7 cm air gaps between the 4.8 cm thick steel plates of the magnet yoke. The magnet is built of 16 C-shaped yokes, where two C-yokes form a ring, such that there are eight yoke rings, numbered from 1 to 8 along the beam direction. The three innermost horizontal (vertical) gaps of are equipped with four 167 mm × 7 mm × 875 mm (7 mm × 175 mm × 875 mm)

[a] The lower pressure with respect to the surrounding volume is a safety measure to avoid the water spilling over the electronics in a case of a leak.

[b] X_0 is the radiation length which is defined to be the distance after which an electron has only $1/e$ of its initial energy remaining.

scintillation counters per gap. For the three most downstream yoke rings (6, 7, 8), more gaps (4, 6, 6) are instrumented with counters.

The scintillator bars are made of doped polystyrene, painted with a reflective TiO_2 coating and hold an S-shaped groove which contains a WLS fiber. 4,016 MPPCs detect the scintillation light and together with information from 880 temperature sensors are read out by 128 TFBs, the same electronics system as it is used for INGRID, the PØD, and the ECal.

The performance shows an average MIP light yield of about 50 photo electrons, and the position resolution is determined to be $\sim$7 cm.

2.4 Super-Kamiokande

The far detector, Super-Kamiokande, is located in the Kamioka Observatory, and has been successfully taking data since 1996. The detector was also used as a far detector for the K2K experiment [114]. It is a 50,000 tons water Čerenkov detector located at a depth of 1,000 m (2,700 meters water equivalent) in the Kamioka mine in Japan. During its four major running periods (SK I to SK IV) Super-Kamiokande contributed results in the field of flavor oscillations of atmospheric, solar and accelerator-produced neutrinos [42, 54, 48, 115, 116], as well as setting the world-leading limits on the proton lifetime [117, 118, 119]. A schematic view of detector is shown in Figure 2.10.

The cylindrical detector cavity is 41 m in height and 39 m in diameter, filled with 50,000 tons of pure water. It consists of two major volumes: The inner detector (ID), 33.8 m in diameter and 36.2 m in height, is surrounded by the approximately 2 m thick outer detector (OD), optically separated by a 50 cm wide cylindrical structure which consists of a stainless steel scaffold covered by plastic sheets. 11,129 inward facing photomultiplier tubes (PMTs), each 50 cm in diameter, are instrumented on all surfaces of the inner detector with a 70.7 cm grid spacing for a 40% cathode surface coverage. The outer detector contains 1,885 outward facing PMTs (20 cm in diameter) on its inner wall and is used as an anti-counter to identify entering/exiting particles to/from the ID.

The primary strategy for T2K flavor oscillation measurements is the counting of CCQE events from electron and muon neutrinos. The relativistic charged particles, produced in these neutrino interactions, travel through the detector with a speed faster than the velocity of light in water. The thereby polarized water molecules rapidly turn back to their ground state and emit Čerenkov light, which is detected by the ID PMTs.

For both ν_e and ν_μ CCQE signals the starting position of the leptons is required to be fully contained in the fiducial volume, which is defined to be more than 2 m away from the ID wall for a total fiducial mass of 22,500 tons. The pulse hight and timing information of the PMTs are fitted to reconstruct the vertex, direction, energy, and particle identification of the Čerenkov rings. A typical vertex, angular and energy resolution for 1 GeV muons is 30 cm, 3° and 3%, respectively. The typical ring shape, which is obtained from fully contained charged particles with an energy above the Čerenkov threshold, allows to infer the vertex position and the momentum of the charged particles. A very good discrimination between fuzzy

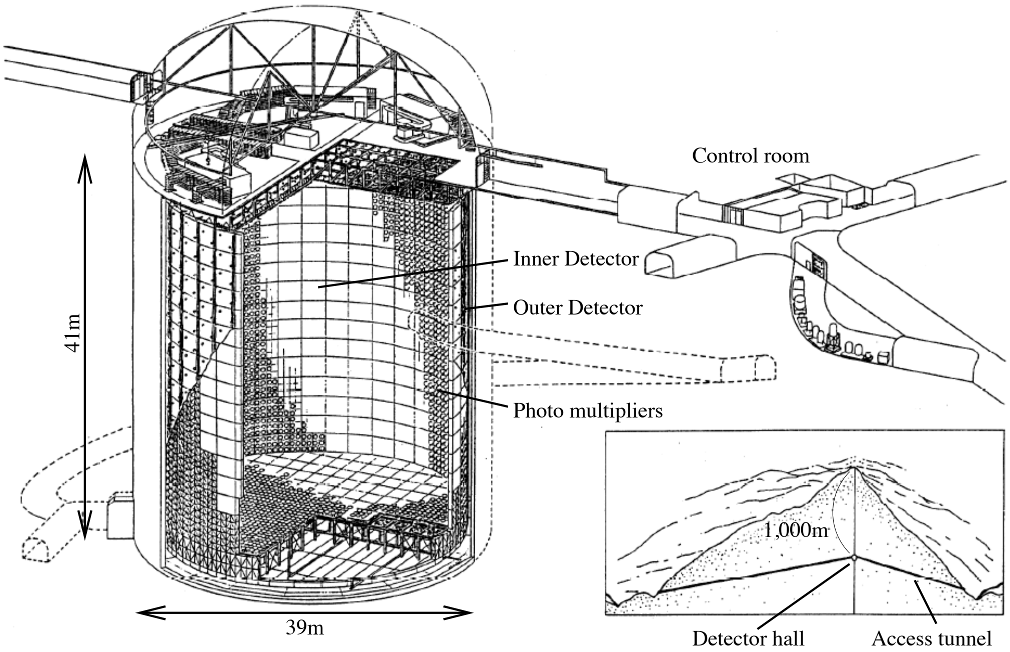

Figure 2.10: A schematic view of the Super-Kamiokande Detector.

electron like rings of Čerenkov light and sharp edged rings from muons enables to separate ν_e from ν_μ interactions. The blurring of the e-like rings originates from multiple scattering which is more likely to occur for electrons than for muons. A typical rejection factor to separate muons from electrons (or vice versa) is about 100 for a single Čerenkov ring event at 1 GeV. The electrons and muons are further separated by detecting decay electrons from the μ decays. A typical detection efficiency of decay electrons from stopping cosmic muons is roughly 80% which can be improved by further analysis. A 4π coverage around the interaction vertex provides an efficient π^0 detection.

Interactions of neutrinos from the J-PARC accelerator are identified by synchronizing the timing between the beam extraction time at the accelerator and the trigger time at Super-Kamiokande using the Global Positioning System (GPS). The synchronization accuracy of the two sites is demonstrated to be less than 200 ns. Because of this stringent time constraint, and the quiet environment of the deep Kamioka mine, a chance coincidence of any entering background is negligibly low. A typical chance coincidence rate of atmospheric neutrino events is 10^{-10} per spill, which is much smaller than the signal rate of about 3×10^{-3} per spill. [101]

For the SK IV period, in which the T2K running period falls, an electronics upgrade was completed in 2008 to improve the data processing rate and the trigger method. The 550 new front end boards for the readout of the 13,014 PMTs allowed an increase of the order of a magnitude in the input pulse rate from 1.4 kHz per channel to 80 kHz per channel. In combination with new programmable software triggers, which are capable of implementing a coincidence trigger with the beam arrival time as in the case of T2K, the setup improved Super-Kamiokande's ability to better accommodate a larger range of neutrino studies. The DAQ system records hit information in a 1 ms time window around the T2K beam arrival time and passes the data to a cluster of online PCs which organizes the PMT hit informations for later offline analysis.

Chapter 3

Magnetic Field Measurement of the ND280 Magnet

The precise mapping of the magnetic field in the instrumented region of the ND280 detector complex has several goals. The dipole magnetic field itself is a key element for precisely measuring the momentum of the charged particles passing through the inner detector volume. The performance requirements of the TPCs correspond to a momentum resolution of better than 10% for $\sim$1 GeV particles, and to a momentum scale known to better than 2% [112]. Besides mapping the distortions of the magnetic field accurately, it is also important to know the absolute scale of the measured magnetic field values.

To achieve these goals, a dedicated movable mapping device was designed, constructed and tested. The device was equipped with 89 electronics cards, each holding three orthogonal Hall probes, to map the instrumented detector region inside the ND280 basket ($2.3\,\mathrm{m} \times 2.4\,\mathrm{m} \times 6.6\,\mathrm{m}$) with an accuracy of the order of 1 G. Because of technical problems with the magnet power supply[a], the ND280 magnetic field was mapped at a mean value of $\sim$700 G. This is almost a factor three lower than the nominal field of the ND280 magnet of 2000 G (0.2 T) which was used during neutrino data taking.

The design of the mapping device and the survey of the equipment will be described in Section 3.1. The calibration of the Hall probes and the achievable accuracy of the probes will be discussed in Section 3.2. The topic of Section 3.3 is the equalization and calibration of the data taken during the mapping campaign. The scaling of the measured field to the nominal values and the systematic errors are also evaluated in detail. Section 3.4 summarizes the results of the mapping.

The description of the mapping device and calibration is also described in a recently published article [120], and the calibration procedure together with the estimation of systematic errors is summarized in a T2K internal note [121]. The final results of the measurements are briefly reported in [99] and will also be discussed in [122]. This chapter combines the results of these articles in a coherent way with an emphasis on the analysis of the magnetic field measurement data.

[a]The temporary problems were solved in the months following the B-field mapping, such that physics data taking from 2010 on has been performed with the nominal magnetic field value.

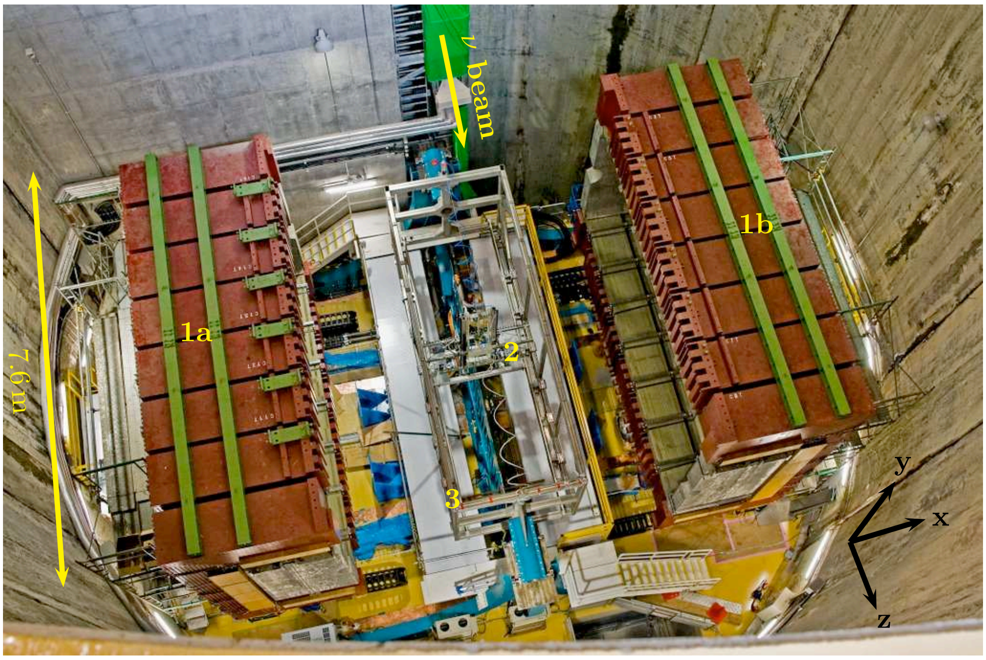

Figure 3.1: Top view of the ND280 magnet with open yokes (1a, 1b). The mapping device (2) is installed within the basket (3).

3.1 The Mapping Device

3.1.1 Mechanics and Electronics

The mapping device was built in a collaboration by the CERN PH-DT group and the Bern T2K group. It was designed to measure a volume slightly larger than the instrumented region inside the basket. The device has a total weight of ~700 kg and consists of three parallel arms, which cover the width (x-direction) of the detector region (2.2 m) and are movable in y (2 m in height) and z (6 m in length). For the movement in the z-direction, additional rails had to be temporarily installed into the basket and aligned with the mapping device.

To prevent undesired field distortions, the whole equipment was built of non-magnetic materials such as aluminum and stainless steel. It can be moved by means of three pneumatic motors (one for the movement in y-direction and two for the movement along the z-axis). A drawing and a photograph of the device are shown in Figure 3.2 and 3.3, respectively.

The information on the position of the mapping device during its operation is read out by four optical encoders (two for the y- and two for the z-direction) which allow the user to control the movement of the equipment and to know the actual position of the measurement bench with a precision of 10 µm.

In total, 89 electronics cards [123] are installed onto the device. Each card is equipped with three Hall probes, which measure the voltage induced by the Hall effect for each component of the magnetic field (B_x, B_y, B_z). The Hall cards also contain a temperature sensor as well as the necessary readout electronics

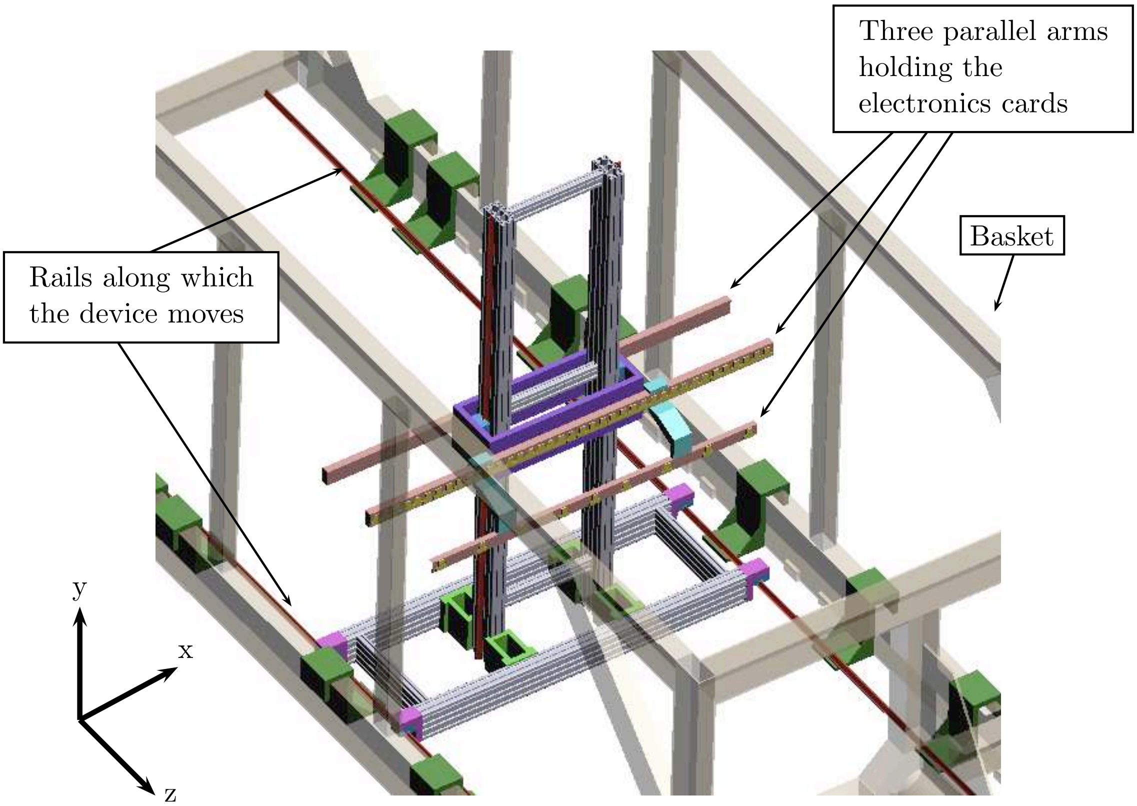

Figure 3.2: Drawing of the mapping device installed into the basket. The device is movable along the rails in z-direction and in y-direction.

(Figure 3.4). The 89 electronics cards are distributed over four chains with a parallel readout. The user can communicate with the cards via CAN bus[b] [124] to activate the routines for movement of the device and initialization, as well as for the readout of the cards. The data of the three Hall probes and the temperature sensor are individually read out and stored. The total readout time per card is 270 ms, summing up to a readout time of 6 s per measurement position.

Each of the two longer arms of the device holds 39 cards covering a range of 2166 ± 1 mm with a distance of 57 ± 0.2 mm from center-to-center of each card in the x-direction. The arms are separated in z-direction by 383 mm. An additional parallel third arm, with a distance of 201 mm in z-direction and 255 mm lower (y-direction) than the second arm, holds 11 cards spread over 1710 ± 1 mm.

3.1.2 Device Survey

The positioning and angular deviations from the desired axes were obtained from several surveys of

1. the mapping equipment and rails with respect to the basket at CERN;

[b] CAN bus is a message-based protocol, which is commonly used as a transfer protocol between electronic control units.

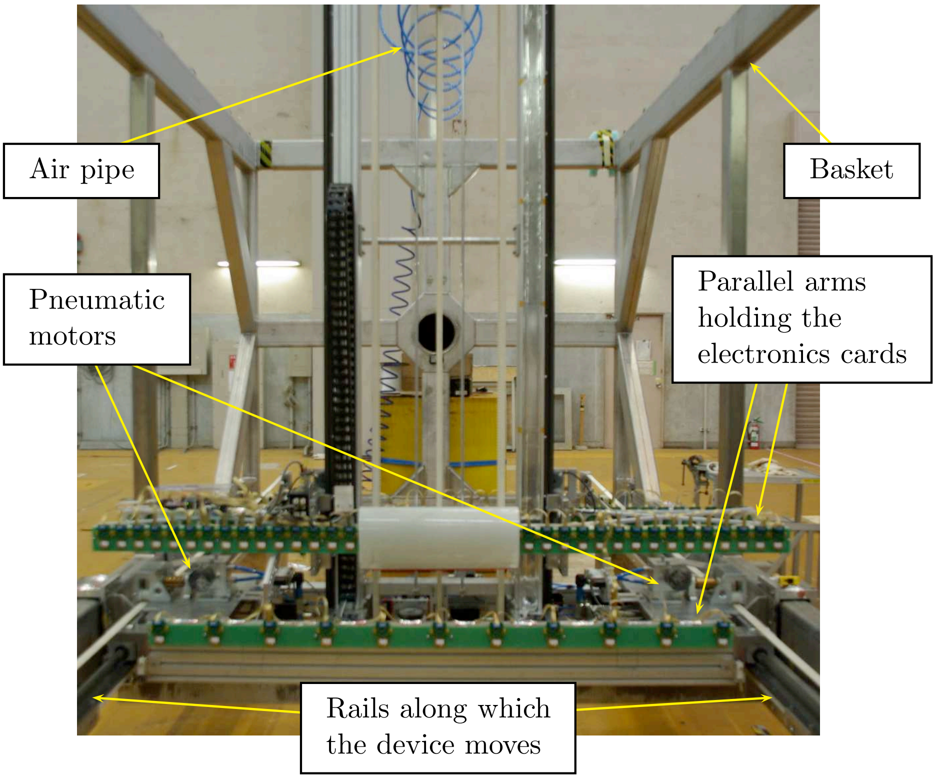

Figure 3.3: Picture of the mapping device in the basket before its installation into the ND280 magnet. Two of three parallel arms which hold the electronic cards are visible. The air pipe supplies the pneumatic motors which drive the machine.

2. the device with respect to the general ND280 reference frame before the actual measurements [125];
3. the device after the field measurement campaigns [125];
4. the positions of the individual Hall probes on the electronics cards.

The x-axis of the ND280 reference frame was chosen to coincide with the corresponding axis of the coordinate system of the mapping device. The second of the above mentioned surveys showed that the y-axis of the mapping device was rotated by 0.8 mrad with respect to the y-axis of the ND280 reference frame. The center of the magnet is the origin of the mapping device reference frame as well as of the ND280 coordinate system.

The three Hall sensors on each card had a slightly different position with respect to each other, as can be seen in Figure 3.5. For the identification of the measurement point, the center of mass of the three probes was taken and the measured voltages were associated with this point. This method induces an error on the position of less than 1 mm. This is negligible, since the magnetic field changes with less than 2 G/cm in the region with the strongest field gradient close to the coils.

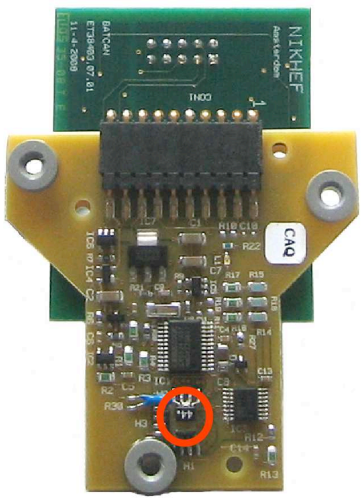

Figure 3.4: One of the cards with its readout electronics is shown. The red circle in the picture indicates the three orthogonal Hall probes which are placed on a small glass cube.

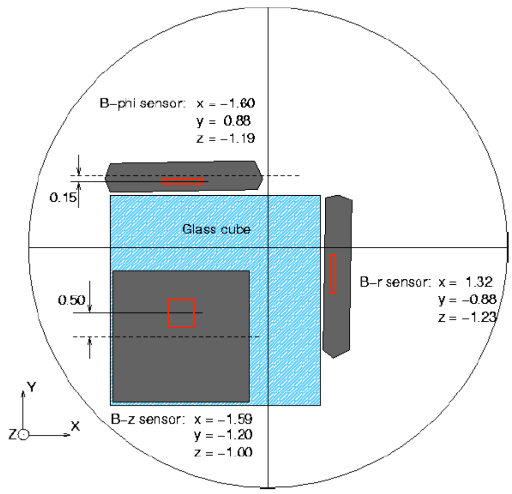

Figure 3.5: Displacements of the Hall probes with respect to each other in mm on a glass cube.

3.2 Hall Probe Calibration

For the Hall probe calibration, performed at CERN, each card was placed in a highly uniform field whose strength was monitored by an NMR probe with a precision of better than 1 G[126]. This setup was already used for the calibration of the field mapping equipment of the ATLAS experiment at the LHC [127, 128]. Pictures of the setup are shown in Figures 3.6 and 3.7. Each card was turned to many different orientations with polar angle θ and azimuth angle ϕ that were precisely measured by pickup coils. The measurements were repeated for several field strengths and temperatures. The Hall voltage (V) is decomposed into orthogonal functions. Spherical harmonics $Y(\theta, \phi)$ describe the rotation angles, and Tschebyshev polynomials T are used for the modulus of the field B and temperature t:

$$V(B, t, \theta, \phi) = \sum_k \sum_n \sum_l \sum_{m=0}^{l} c_{klm} T_k(B) d_{nlm} T_n(t) Y_{lm}(\theta, \phi) \tag{3.1}$$

Using this series, a total of about 200 calibration parameters was calculated for each probe. A separate angular calibration was used to find the orientation of the calibrated coordinate system relative to the three feet that support the card on the mapping device.

All Hall probes were calibrated at 0.2 T and 1.14 T, and probes which deviated more than 2 G at a field of 0.2 T were rejected. A few probes were also calibrated at 0.1 T as a cross-check, and the results were found to be consistent. Figure 3.8 shows the measurements for one of the probes. The accuracy for the angular alignment

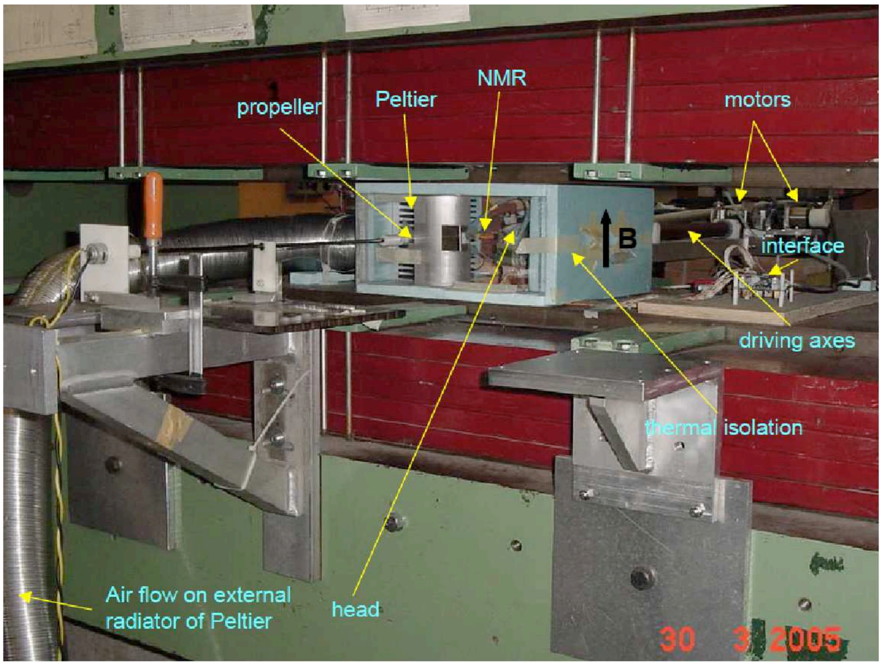

Figure 3.6: Photograph of the calibration setup. In a homogenous magnetic field (from bottom to top) a thermally isolated box is mounted, which is temperature controlled by a Peltier element and a ventilator. Inside the box, an NMR probe monitors the magnetic field and the head to hold the cards with the Hall probes is installed. The head can be rotated freely in three dimensions, which is done by two external motors via driving axes.

between the three probes on an electronic card was measured to be ± 2 mrad. An improvement on both values, the accuracy of the magnetic field and the angular alignment, can be obtained from the actual mapping data, as described in 3.4. All probes have an intrinsic resolution of 0.2 G, which was obtained from repeated B-field measurements under identical conditions, constant B-field, temperature and angle with respect to the magnetic field.

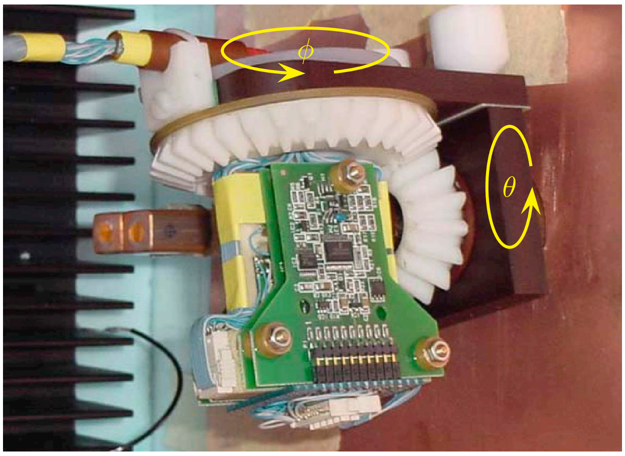

Figure 3.7: Photograph of one of the electronics cards installed within the calibration setup. The card can be rotated in angles ϕ and θ around two orthogonal axes.

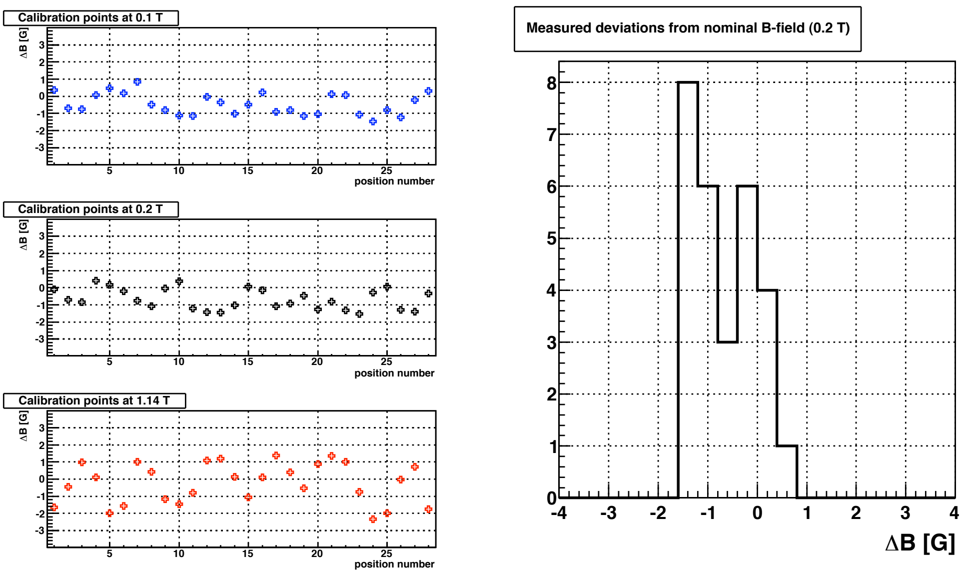

Figure 3.8: Calibration measurements for one of the Hall probes at 28 angles in 45° steps. The measurements for three different magnetic field values are shown on the left (top: 0.1 T, middle: 0.2 T, bottom: 1.14 T). At a magnetic field of 0.2 T, the deviation of B from the nominal magnetic field is below 2 G for all measured angles, as can be inferred from the distribution on the right.

3.3 Calibration and Corrections of the B-field Data

After the mapping, the data were analyzed carefully and the following steps of the calibration were applied:

1. Uncertainties of the survey of the equipment.
2. Corrections for non-linearities in the magnetic field.
3. Skewing corrections due to the movement of the mapping device.
4. Corrections for the misalignment between the Hall probes.
5. Extrapolation from 1000 A up to the nominal values of 2600 A, 2700 A and 2900 A.

All these steps have been cross-checked and several consistency checks were performed which will be mentioned in the corresponding sections of this thesis.

3.3.1 Uncertainties of the Survey of the Equipment

Before and after the mapping of the ND280 magnet, the mapping device was surveyed inside the ND280 basket. Details on this can be found in [125]. As an upper limit on the uncertainty on the position, the value of 1 mm has been estimated. This implies an error of 0.5 mrad on the angle with respect to the ND280 reference frame (1 mm uncertainty over a length of 2.2 m for the mapping device).

3.3.2 Correction of Non-linearities of the Magnetic Field

When ramping up the magnet, a non-linear behavior between the current in the magnet coils and the measured magnetic field is observed. At higher field values, a saturation of the ND280 iron yoke decreases the magnetic field. In a first order approximation, a quadratic function is fitted to describe this behavior, based on the observations of the UA1 and NOMAD experiments which used the same magnet before (and applied similar corrections)[c]. A summary of the magnetic field mapping of the UA1 magnet is given in [129]. For the mapping of ND280 the input values are taken from 220 measurement positions throughout the full basket at a set current of 250 A, 500 A, 750 A and 1000 A. The measured current values of the coils are a little higher than the nominal values (+0.089%), but in this thesis, and in all calculations, I will refer to the nominal values[d]. The parameterization of the fitting function is:

$$B[G] = c_0 + c_1 I(1 + c_2 I) = c_0 + c_1 I + c_1 c_2 I^2 \tag{3.2}$$

[c]However, these experiments had magnet end caps installed, which changes the properties of the magnetic yoke.

[d]Using the true field values would simply implement an additional factor of 1/1.00089 for the c_1 and c_2 parameter in Equation 3.2 and complicate calculations by having to use numbers like 2602.3 A instead of a round number (2600 A in this case) in the reconstruction code.

The c_2 parameter only depends on the magnetization features of the iron yoke. In fact, it also takes into account the magnetization of all surrounding materials such as the basket or the mapping device itself, but the influence of those can be regarded as negligible. In Figure 3.9 the distribution of c_2 for all measurement points is shown to peak at a value of $-3.0 \times 10^{-3}\,\mathrm{kA}^{-1}$. With this given value of c_2, the fit is then repeated for each probe and each direction (B_x, B_y and B_z).

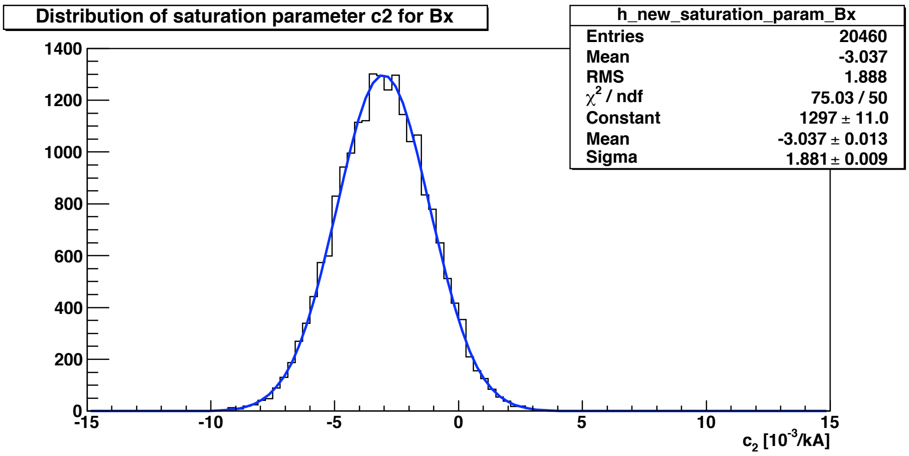

Figure 3.9: Distribution of the fitted c_2 parameter for all measured positions. A Gaussian fit to the distribution is shown in blue. A mean value of $-3.0 \times 10^{-3}\,\mathrm{kA}^{-1}$ is retrieved.

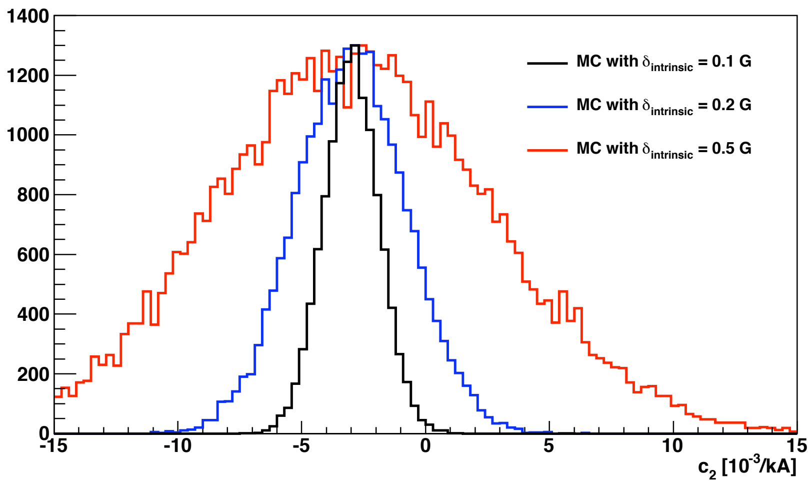

Figure 3.10: MC distribution of the fitted c_2 parameter for all measured positions. Three different values for the intrinsic resolution were simulated (0.1 G, 0.2 G and 0.5 G), and the histograms are normalized to the same maximum value. The width of the distribution is compatible with the data for an assumed resolution of 0.2 G.

The large value of the RMS has two contributions. On the one hand, because of its low value the c_2 parameter is very sensitive to the intrinsic Hall probe resolution of $\sim$0.2 G of each probe. This was checked with a Monte Carlo simulation for different values on the assumed intrinsic resolution of the probes, as shown in Figure 3.10. The measured intrinsic resolution is shown in Figure 3.11. On the other hand, the mean value of the fitted c_2 parameter varies from probe to probe (see Figure 3.12). The combination of the two effects results in the relatively large width of the distribution in Figure 3.9.

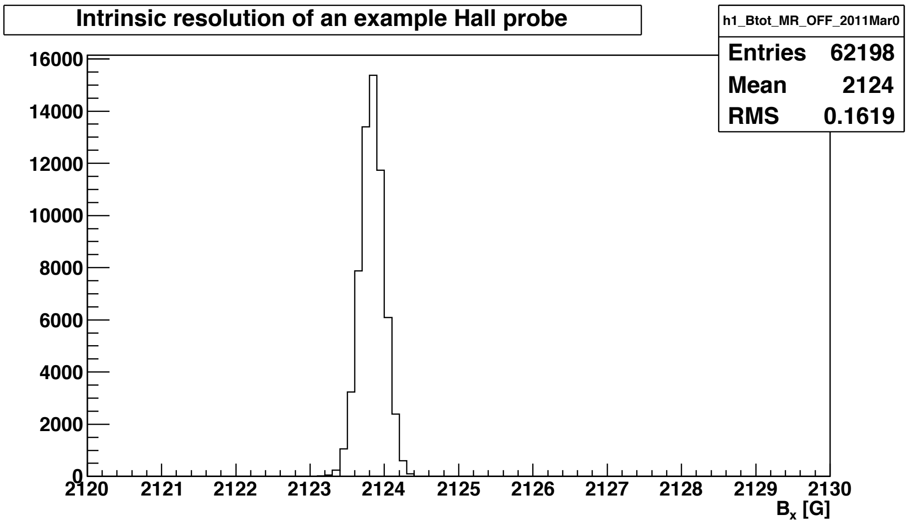

Figure 3.11: Data from one of the permanent Hall cards over the period of three weeks with stable magnet operation. The width of the distribution is a measure for the intrinsic resolution of the probe.

The remaining two parameters c_1 and c_0 describe the strength of the field and the offset value for each probe, respectively. Note that c_1 is the conversion factor from the applied current to the coils to the observed magnetic field in case of no disturbing effects like saturation. This factor varies for each measured position. The parameter c_0 is a property of each Hall probe and corrects for possible offsets. It combines the effects at very low currents and possible distortions at 0 A coil current, such as background fields (like the Earth magnetic field) or remaining magnetization of the yoke.

Figure 3.13 shows the distribution of the offsets for all Hall probes and the corresponding errors. The fact that the errors on the c_0 parameter are rather low with $\delta(c_0) = 0.2$ G and that the RMS $= 1.5$ G for all values is below 2 G confirms the precision from the calibration procedure at CERN.

3.3.3 Skewing Corrections

During the mapping campaign the position of the mapping device in the y- and z-direction was carefully monitored with the help of optical sensors. This allows to correct for skewing and twisting of the mapping device with respect to the

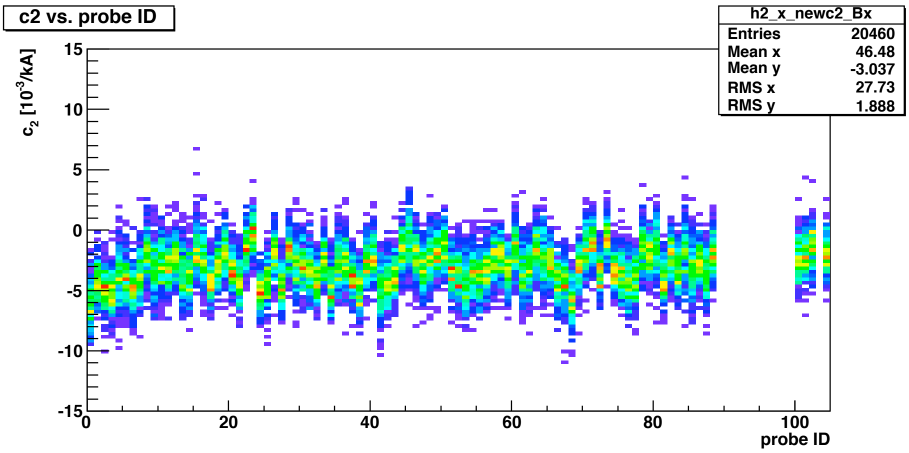

Figure 3.12: The c_2 parameter in dependence on the probe number. The mean value for all fitted c_2 values varies with the probe.

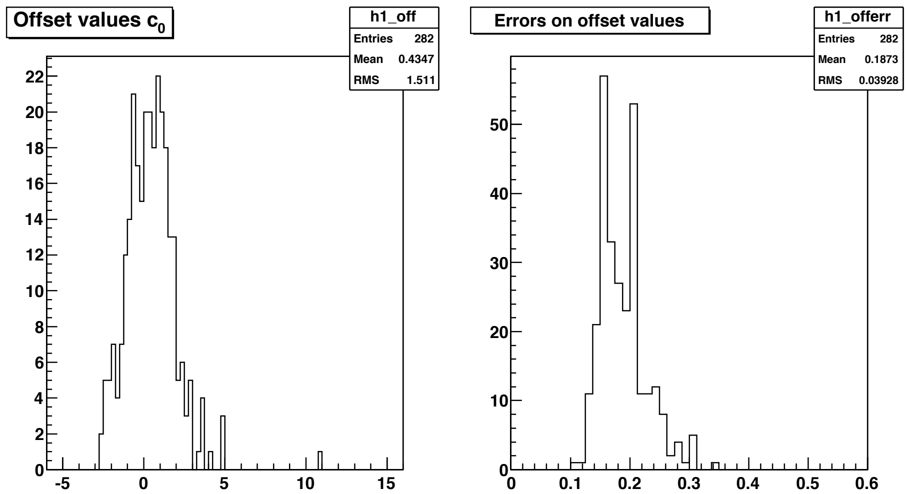

Figure 3.13: Distribution of the offsets for all Hall probes (left). The error for each offset value (right) is at the order of the intrinsic variation (0.2 G) of the Hall probes.

axes of the reference system. Such skewings can happen when the two motors, which drive the device in z-direction, stop at slightly different positions. This independent control of the motors ensured a smooth movement of the mapping device. Because the arms have a length of 2.2 m and the position is monitored with a precision of 0.1 mm, the measured rotations of the mapping device are of the order of 0.1 mrad. In formulas, the corrections are:

$$\begin{aligned}
&\sin\alpha_z = \Delta z/d, \quad \cos\alpha_z = \sqrt{1-(\Delta z/d)^2} \text{ and likewise for } \alpha_y \\
&B'_x = B_x\cos(\alpha_y+\alpha_z) - B_y\sin\alpha_y - B_z\sin\alpha_z \\
&B'_y = B_y\cos\alpha_y + B_x\sin\alpha_y \\
&B'_z = B_z\cos\alpha_z + B_x\sin\alpha_z,
\end{aligned}$$

where d is the distance between the two rails, Δz the distance between the stopping positions of the two pneumatic motors for the movement in the z-direction, and α_i the angles of the skewing. The corrected values B'_i are used for the further analysis. As an example, Figure 3.14 shows the effect of the correction for B_y. With this method, effects at the level of the intrinsic probe resolution of 0.2 G can be corrected.

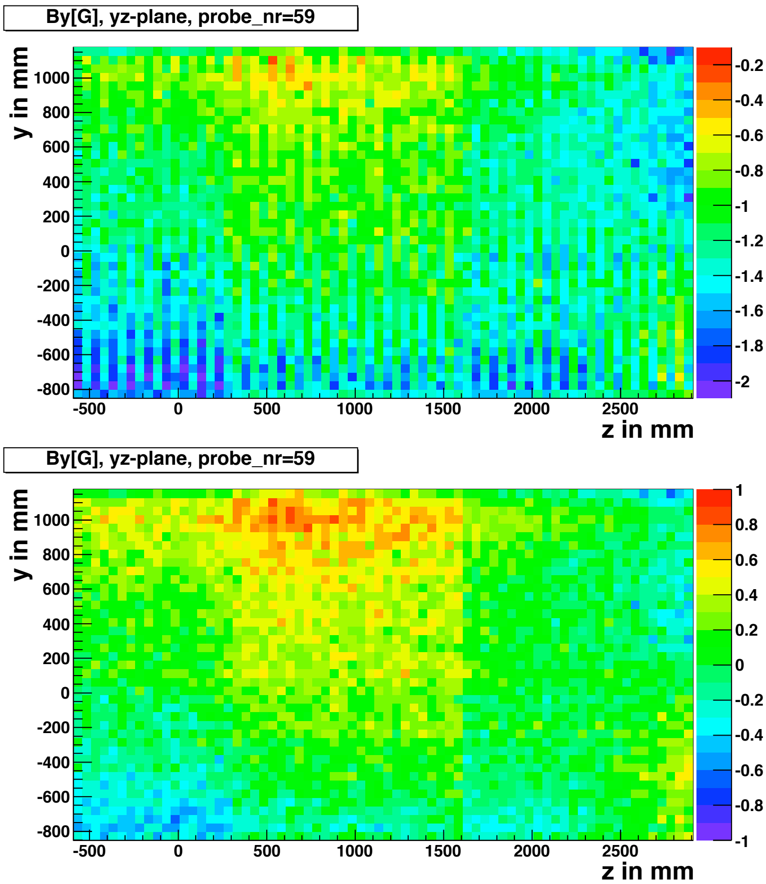

Figure 3.14: Side view of the ND280 TPC region. The colors indicate the B_y field values in G. One can see the improvement (top: without correction; bottom: with correction) of data quality after correcting for skewing effects of the device. The differences between neighboring columns vanish due to the correction and the mean value moves closer to 0 G.

3.3.4 Misalignment Between the Hall Probes

The misalignment of each probe with respect to each other must also be taken into account. From the calibration at CERN (Section 3.2) it is known that the probe alignment agrees within $\pm 2\,\mathrm{mrad}$. For the transverse components B_y and B_z, the alignment can be further refined by exploiting the cartesian symmetry of the ND280 magnet geometry. In the horizontal symmetry plane of the coils at $y = 0$, we expect the vertical field distortions for B_y to vanish. An analogue statement holds for the B_z component.

In these planes of symmetry ($y = 0$ and $z = 0$), either $|B_y|$ or $|B_z|$ should be minimal everywhere. The mean value of one B-field component of the probes along the second arm is taken and defined to be the reference value.

$$B_y^{min} = \overline{B}_y = \frac{1}{39 \cdot n} \sum_{i=1}^{n} \sum_{j=1}^{39} B_{y,ij},$$

with i being the index of the n stopping positions in the y=0-plane of the measurement device and j an index for the 39 Hall probes of the second arm. B_y^{min}=0 holds if the y-axis of the mapping device is perfectly orthogonal to the main component of the magnetic field. The correction for each Hall probe j rotates the y-axis of the probe into the x-direction[e] by an angle φ_j such that the mean of B_y^j equals B_y^{min}:

$$B_y^{min} = \frac{1}{n} \sum_{i}^{n} (B_{y,ij} + \varphi_j \cdot B_{x,ij})$$

$$\Leftrightarrow \quad \varphi_j = \frac{n \cdot B_y^{min} - \sum_i^n B_{y,ij}}{\sum_i^n B_{x,ij}}$$

The analogue rotation with the angle ϑ_j is done for each probe in B_z.

$$\vartheta_j = \frac{m \cdot \sum_i^m B_z^{min} - B_{z,j}}{\sum_i^m B_{x,j}},$$

where m is the number of the measurement position in the z=0-plane. Note that $\varphi_j = \frac{1}{n} \sum_i^n \varphi_{ij}$ and $\vartheta_j = \frac{1}{m} \sum_i^m \vartheta_{ij}$ are the mean rotations for a given probe j under the assumption of a constant B_x, which is true at a level of $\pm 1\%$ for almost the complete measured region. Only for the most downstream part of TPC 3, B_x can differ by up to 4% with respect to the value in the center of the magnet. The uniformity also guarantees that an alignment correction has the same effect as an offset correction, the two effects are indistinguishable.

The values for the mean field values in the symmetry planes and its errors after corrections are:

$$B_y^{min} = 0.08 \pm 0.18\,\mathrm{G} \quad \text{and}$$

$$B_z^{min} = -1.34 \pm 0.35\,\mathrm{G}$$

This implies that the y-axis of the mapping equipment is well aligned with the ND280 reference frame, while the z-axis is systematically rotated.The distributions for the 39 rotation angles are shown in Figure 3.15.

[e] This rotation does not effect the orthogonal B_x and B_z values.

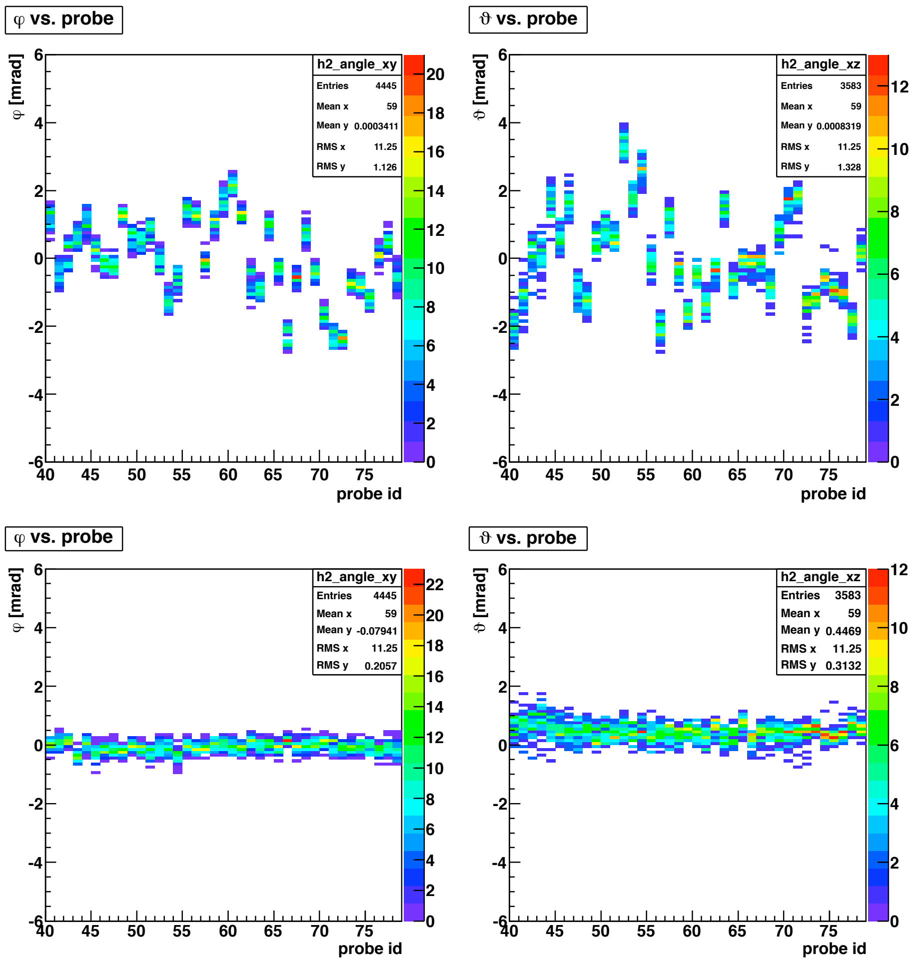

Figure 3.15: The misalignment of the 39 probes along arm 2 of the mapping device before (upper plots) and after the correction (bottom plots) are shown. Each entry corresponds to the rotation with respect to the B_x direction at one measurement point. The rotations of each probe in the xy-plane and xz-plane are denoted by φ and ϑ, respectively.

Figure 3.16 shows the improvement of the data quality for B_y in the plane where y=0. The discrepancy of neighboring measurement points decreases with the applied corrections. The width of 0.3 G/kA (i.e. 0.3 mrad) from the distributions in Figure 3.17, in which the differences in B-field values of neighboring probes are plotted, is taken as a measure for the systematic error of this method.

For $x = 0$, the B_x value is not minimal since this is the main component of the field, which is intended to be as large and uniform as possible. Also, assuming small rotations of not more than 2 mrad and since the B_y- and B_z component are much smaller, their influence is negligible. Only rotations with respect to the x-axis (ξ) need to be considered, which leads to a deviation

$$\Delta B_x = B_x \cdot (1 - \cos\xi) \approx B_x \cdot \frac{\xi^2}{2} \leq 712.6\,\mathrm{G} \cdot \frac{4 \times 10^{-6}}{2} \approx 0.014\,\mathrm{G},$$

where 712.6 G is the measured value for B_x in the center of the magnet, which here is used to illustrate the smallness of the effect. In other words, small rotations of the x-direction do not have any effect on the magnetic field scale.

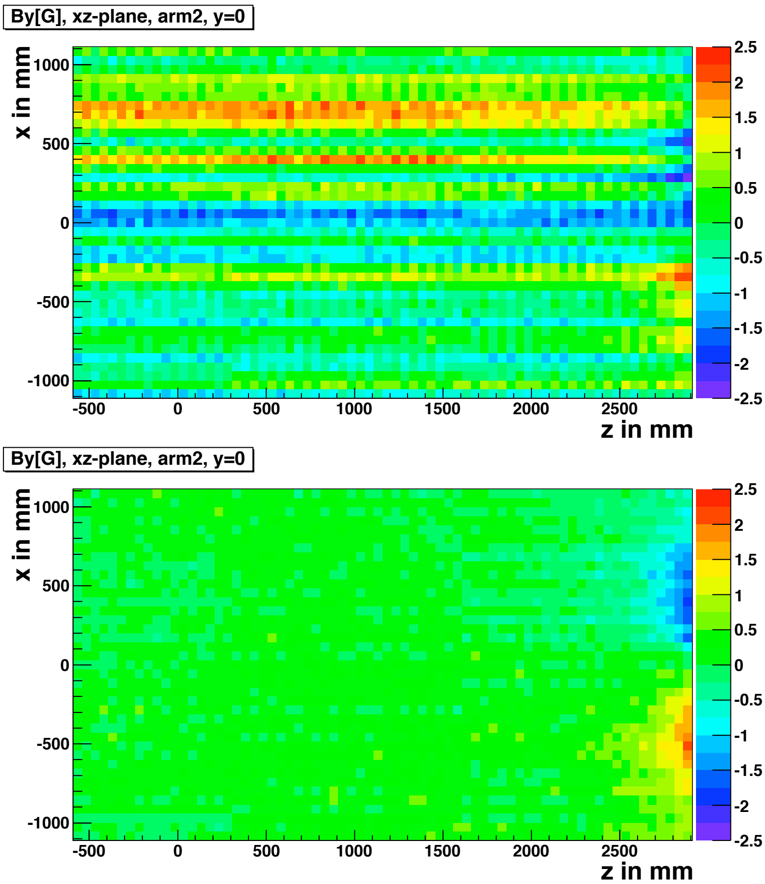

Figure 3.16: Top view on the ND280 TPC region. The colors represent the B_y field values in the horizontal symmetry plane (y=0). Each row corresponds to the measurements of one probe. The differences of the the absolute measured values between the probes is significantly lowered (top: without correction; bottom: with correction). The blue and red colored regions on the right-hand-side of the plot are expected to be as they are, since these are the regions close to the gaps between the coils. Only with the correction of the data, these effects become visible.

3.3.5 Extrapolation from 1000 A to 2600 A, 2700 A and 2900 A

The nominal B-field exceeds the field which was available during the mapping by almost a factor of three. Therefore, the measured B-field values need to be scaled to the actual field values. In order to estimate the scaling function, dedicated stepwise ramp-ups of the ND280 magnet were performed. The acquired values are reported in the Tables 3.1 and 3.2. With the help of the permanent probes, the scaling factor α and its error can be deduced. The scaling factor is the factor with which all B-field values, which were measured at 1000 A, have to be multiplied in

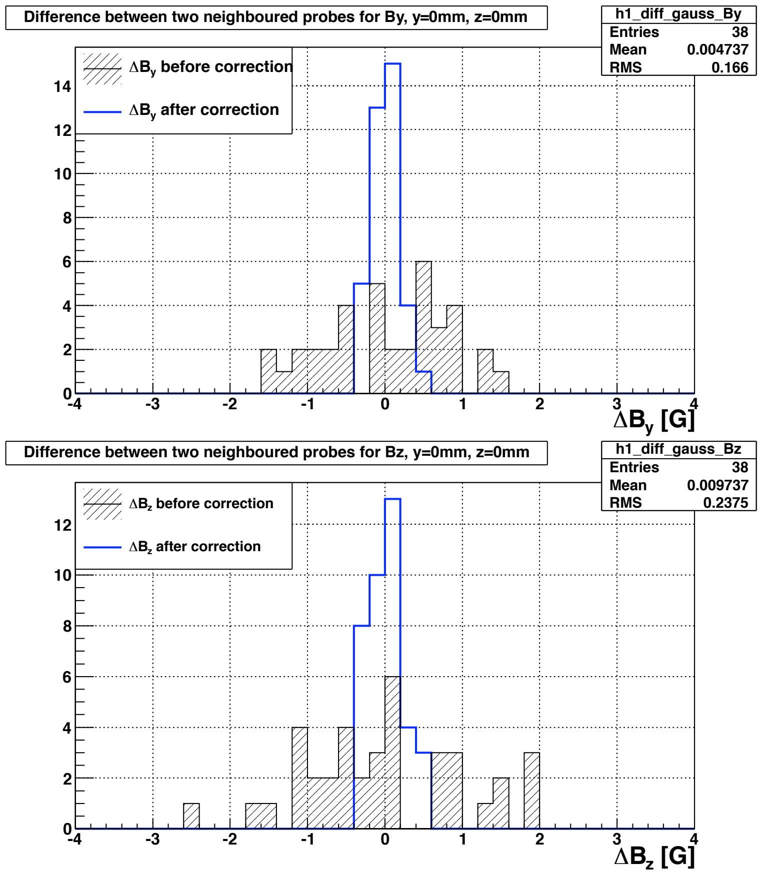

Figure 3.17: Deviations of the measured values between adjacent probes before and after the corrections for B_y (top) and B_z (bottom). The fact that the mean of the distributions is at zero shows that there is no rotational bias along the x-direction.

order to retrieve the corresponding B-field at a different current value. The details for the calculation of the errors of this factor are given in the appendix.

As a cross-check, the field value in the center of the magnet was calculated for 2600 A with the data of the two ramp-ups. The value of $B_x = 1838.70 \pm 9.79$ G from April 2010 is in very good agreement with $B_x = 1838.92 \pm 9.74$ G for the November 2010 data. This indicates a good reproducibility of the magnetic field. Note that the specified errors are systematic errors (as explained in more detail in Section 3.3.6), which cancel out when taking the ratio of the two values. Therefore, the reproducibility of the magnetic field has a precision of better than 2×10^{-4}.

Figure 3.18 shows the ratio of the values of the parameters retrieved from the fit with the November 2010 data and the April 2010 data. The data agrees fairly well, however, a bias due to external effects, e.g. the magnetization of the basket, cannot be excluded completely.

Table 3.1: Measured B-field values in G and fitting parameters for the permanent probes from ramping up to 2600 A coil current on April 12th 2010.

	probe 101	probe 102	probe 103	probe 105
I_{coil} in A	B_{meas} in G			
500	371.3	370.2	368.4	371.0
1000	739.9	738.0	736.8	740.3
1500	1106.9	1104.3	1104.1	1108.2
2000	1471.9	1469.0	1469.4	1474.2
2500	1834.8	1831.6	1832.5	1838.1
2600	1907.2	1903.9	1904.8	1910.7
parameters	fitting coefficients			
$\mathbf{c_0}$ [G]	0.54 ± 0.28	0.43 ± 0.25	-2.41 ± 0.47	-0.45 ± 0.27
$\mathbf{c_1}$ [G kA^{-1}]	743.3 ± 0.41	741.2 ± 0.37	743.2 ± 0.69	744.6 ± 0.39
$\mathbf{c_2}$ [10^{-3} kA^{-1}]	-5.13 ± 0.171	-4.68 ± 0.152	-4.97 ± 0.285	-4.91 ± 0.163
scaling 2600 A	2.577(3)	2.580(3)	2.584(5)	2.580(3)
	2.5803(46)			

Table 3.2: Measured B-field values in G and fitting parameters for the permanent probes from ramping up to 2950 A coil current in November 2010.

	probe 101	probe 102	probe 103	probe 105
I_{coil} in A	B_{meas} in G			
100	76.7	76.7	74.3	75.6
500	371.0	370.9	368.4	371.0
1000	739.5	739.1	736.4	740.5
1500	1106.3	1105.6	1103.5	1108.4
2000	1471.3	1470.4	1468.8	1475.5
2500	1834.3	1833.3	1831.8	1838.8
2600	1906.7	1905.8	1904.2	1911.5
2700	1979.0	1978.1	1976.5	1984.2
2800	2051.4	2050.3	2048.7	2056.8
2850	2087.7	2086.3	2084.9	2093.2
2900	2123.8	2122.3	2120.8	2129.2
2950	2159.5	2158.4	2157.0	2165.6
parameters	fitting coefficients			
$\mathbf{c_0}$ [G]	0.82 ± 0.24	0.78 ± 0.13	-2.23 ± 0.34	-0.72 ± 0.57
$\mathbf{c_1}$ [G kA^{-1}]	742.3 ± 0.31	741.9 ± 0.17	742.6 ± 0.44	745.0 ± 0.74
$\mathbf{c_2}$ [10^{-3} kA^{-1}]	-4.78 ± 0.113	-4.80 ± 0.062	-4.87 ± 0.162	-4.89 ± 0.270
scaling 2900 A	2.8714(3)	2.8714(2)	2.8787(5)	2.8747(8)
$\mathbf{c_0}$ [G]	-0.34			
$\mathbf{c_1}$ [G kA^{-1}	742.95			
$\mathbf{c_2}$ [10^{-3} kA^{-1}]	-4.84			
scaling 2900 A	2.8741(35)			

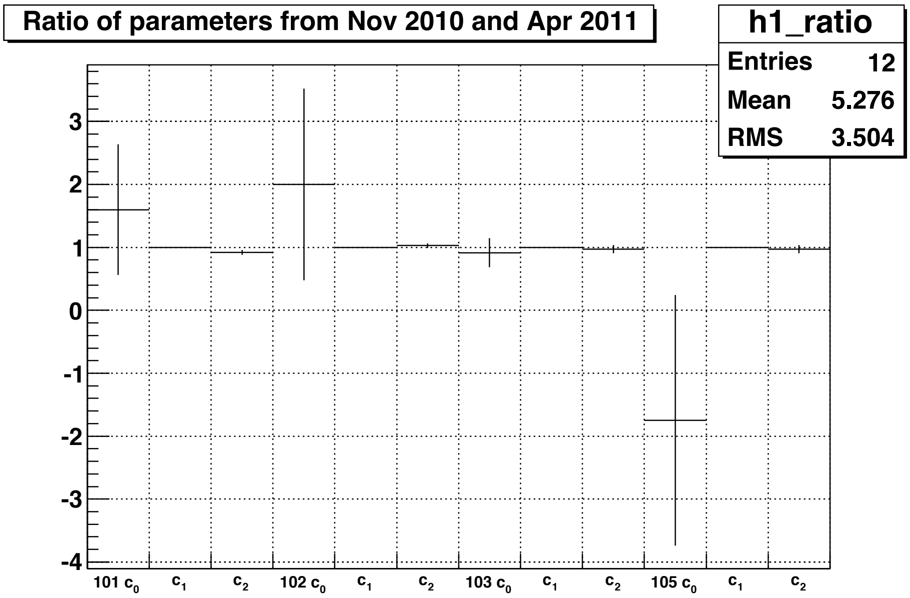

Figure 3.18: Ratio of parameter values for the four permanent Hall probes (101, 102, 103 and 105) retrieved in November 2010 and April 2010.

Table 3.3: Summary of systematic errors for the B-field determination.

Source of error	**Assigned value**	**Comments**
intrinsic uncertainty	0.2 G	
error on c_0 (offset)	0.2 G	
skewing of mapping device	1 mrad	before correction
	0.1 mrad	after correction
misalignment between probes	2 mrad	before correction
	0.3 mrad	after correction
uncertainty from surveys	0.5 mrad	
c_2 parameter	$1.9 \times 10^{-3}\,\mathrm{kA}^{-1}$	
scaling	0.0035	for 2900 A
Total effect		
resolution	0.28 G	
misalignment	0.59 mrad	
c_2 parameter	$1.9 \times 10^{-3}\,\mathrm{kA}^{-1}$	
scaling	0.0035	for 2900 A

3.3.6 Summary of Systematic Errors

Table 3.3 summarizes the systematic errors of the B-field calibration and its impact on the final values. An example for the explicit calculation is given in Table 3.4. For the main component B_x, the scaling is the main source of uncertainty; whereas for the transverse components (B_y, B_z), the misalignment of the probes dominates the systematic error.

The resolution is the combination of the intrinsic resolution of the Hall probes and the error of the offset correction (i.e. the error of the c_0 parameter), both errors are added in quadrature.

The misalignment combines three effects: uncertainties of the skewing of the mapping device with its reference frame, the remaining error on the misalignment between the probes, and finally the uncertainty of the survey which connects the mapping device reference frame with the ND280 reference frame. All three effects are added in quadrature. Note that this type of error scales linearly with an increasing B-field value.

The third kind of corrections concerns the non-linearities of the B-field. For the measurements at 1000 A, this error contains only the uncertainty on the c_2 parameter. The value of $1.9 \times 10^{-3}\,\mathrm{kA}^{-1}$ is assigned as systematic error for c_2, because this is the difference from the mean value for all Hall probes at 1000 A (Section 3.3.2) and the mean value for the permanent probes which we retrieved from the ramp-ups to 2600 A and 2900 A (Section 3.3.5). However, when extrapolating to higher field values, uncertainties on the non-linear part of the B-field become the dominant source of systematic errors.

With the following formulas, the errors at a given field strength can be calculated:

$$\delta_{\mathrm{resolution}} = \sqrt{\delta^2_{\mathrm{intrinsic}} + \delta^2_{c0}} \qquad \text{in G}$$

$$\delta_{\mathrm{align}} = \sqrt{\delta^2_{\mathrm{skew}} + \delta^2_{\mathrm{misalign}} + \delta^2_{\mathrm{survey}}} \qquad \text{in mrad}$$

$$\delta_{c_2} = \bar{c}_2^{\,\mathrm{rampup}} - \bar{c}_2^{\,1000\,\mathrm{A}} \approx RMS(c_2^{1000\,\mathrm{A}}) \qquad \text{in } 10^{-3}\,\mathrm{kA}^{-1}$$

$$\delta_\alpha = \sqrt{\frac{1}{4}\sum \delta^2_{i,\alpha} + \frac{1}{4}\sum(\alpha_i - \overline{\alpha})^2}$$

with $i = 1, 2, 3, 4$ being the index for the permanent probes and δ_i is the scaling error as decribed in the appendix

$$\sigma_{\mathrm{resolution}} = \delta_{\mathrm{resolution}} \qquad \text{in G}$$

$$\sigma_{\mathrm{align}} = \delta_{\mathrm{align}} \cdot B_{\mathrm{mod}} \quad \text{with } B_{\mathrm{mod}} = \sqrt{B_x^2 + B_y^2 + B_z^2} \approx B_x \qquad \text{in G}$$

$$\sigma_{c_2} = c_1 \cdot \delta_{c_2} \cdot I^2 \quad \text{with } c_1 \cdot I[\mathrm{kA}] \approx B \qquad \text{in G}$$

$$\sigma_{\mathrm{scaling}} = \delta_\alpha \cdot B(1000\,\mathrm{A}) \qquad \text{in G}$$

Therefore, the systematic error for any desired B value can be calculated with:

$$\begin{aligned}\sigma(B) =&\sqrt{\sigma^2_{\text{resolution}} + \sigma^2_{\text{align}} + \sigma^2_{c_2} + \sigma^2_{\text{scaling}}}\\ =&\big[(0.28\,\text{G})^2 + (0.00059 \cdot B_{\text{mod}})^2\\ &+ (0.0019 \cdot I\ [\text{kA}] \cdot B)^2 + (0.0035 \cdot B(1000\,\text{A}))^2\big]^{0.5}\end{aligned}$$

Table 3.4: Example calculations for determining the systematic errors.

B measured at 1000 A:		$B_x = 712.60$ G	$B_z = 10.00$ G
misalignment	0.59 mrad	0.42 G	0.42 G
resolution	0.28 G	0.28 G	0.28 G
c_2 parameter	$1.9 \times 10^{-3}\,\text{kA}^{-1}$	1.35 G	0.02 G
total error		$\sigma(\mathbf{B_x}) = \mathbf{1.45\ G}$	$\sigma(\mathbf{B_z}) = \mathbf{0.51\ G}$

$B(1000\,\text{A})$ scaled to 2600 A:		$B_x = 1838.92$ G	$B_z = 25.81$ G
misalignment	0.59 mrad	1.08 G	1.08 G
resolution	0.28 G	0.28 G	0.28 G
scaling	0.0030	2.11 G	0.04 G
c_2 parameter	$1.9 \times 10^{-3}\,\text{kA}^{-1}$	9.15 G	0.13 G
total error		$\sigma(\mathbf{B_x}) = \mathbf{9.46\ G}$	$\sigma(\mathbf{B_z}) = \mathbf{1.13\ G}$

$B(1000\,\text{A})$ scaled to 2700 A:		$B_x = 1908.73$ G	$B_z = 26.79$ G
misalignment	0.59 mrad	1.13 G	1.13 G
resolution	0.28 G	0.28 G	0.28 G
scaling	0.0031	2.23 G	0.04 G
c_2 parameter	$1.9 \times 10^{-3}\,\text{kA}^{-1}$	9.87 G	0.14 G
total error		$\sigma(\mathbf{B_x}) = \mathbf{10.19\ G}$	$\sigma(\mathbf{B_z}) = \mathbf{1.17\ G}$

$B(1000\,\text{A})$ scaled to 2900 A:		$B_x = 2048.14$ G	$B_z = 28.74$ G
misalignment	0.59 mrad	1.21 G	1.21 G
resolution	0.28 G	0.28 G	0.28 G
scaling	0.0035	2.48 G	0.05 G
c_2 parameter	$1.9 \times 10^{-3}\,\text{kA}^{-1}$	11.39 G	0.16 G
total error		$\sigma(\mathbf{B_x}) = \mathbf{11.72\ G}$	$\sigma(\mathbf{B_z}) = \mathbf{1.25\ G}$

3.4 Results of the ND280 Magnetic Field Mapping

In the absence of electric currents and with a quasi static electric field, the Maxwell equations for the magnetic field take the form $\nabla \cdot \mathbf{B} = \mathbf{0}$ and $\nabla \times \mathbf{B} = \mathbf{0}$. This is the case for the mapped volume. The magnetic field data from the Hall probes is fitted to a function, which fulfills these constraints and will be derived later in this section. The goodness of fit gives an indication whether there are additional sources of the magnetic field which demand a change of the boundary conditions. The fitting also helps to smooth out statistical errors. The dominant part of the statistical errors comes from the intrinsic probe resolution, which is rather low with a value of $\sim$0.2 G.

Based on the conductor geometry, a field model was built with the OPERA-TOSCA [130] simulation package, which uses the finite element method. From this model an estimate of the expected field intensity can be inferred, but due to the simulation method there is no analytical function representing the field.

The geometry of the magnet has symmetries in cartesian coordinates with the origin in the center of the magnet as a point of symmetry. Exploiting this feature one obtains the following expression of the magnetic potential Φ_{M} which fulfills the Maxwell conditions:

$$\Phi_{\mathrm{M}} = \sum_{n,m}^{\infty} A_{nm} \sin(a_n x + \alpha_n) \cos(b_m y + \beta_m) \cosh(c_{nm} z + \gamma_{nm}) \tag{3.3}$$

where n,m are integer indices and the constraint $\alpha_n^2 + \beta_m^2 = \gamma_{nm}^2$ is obtained from the solution for the magnetic potential by means of applying the technique

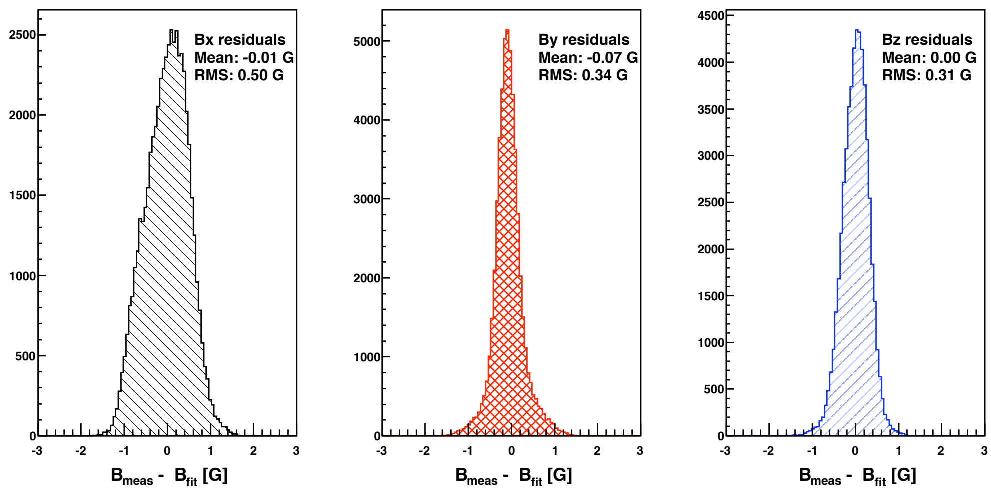

Figure 3.19: Distribution of residuals for each B-field component of the measurements done at the field magnitude of 700 G. The widths of the distributions which is 0.5 G for the B_x component and even smaller for B_y and B_z are a measure for the fit quality and the understanding of not yet respected uncertainties.

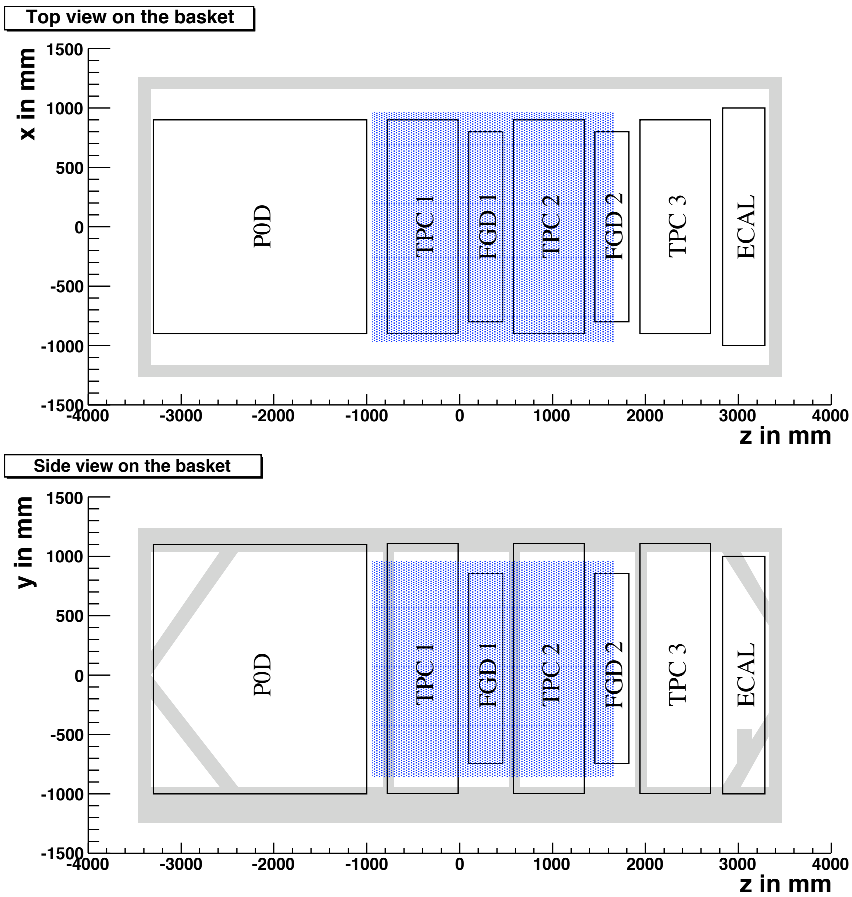

Figure 3.20: Top view (top) and side view (bottom) of the ND280 basket (in grey) and its containing detectors. The blue dotted region indicates the volume, for which the data fitting is applied.

of separation of variables. The other parameters a_n, b_m, c_{nm} and A_{nm} are free parameters which are determined by the fit. From $\mathbf{B} = -\mu\nabla\Phi_{\mathrm{M}}$, the corresponding series for the magnetic field is obtained. Thus, we can use these series to obtain a best combined fit $B^{\mathrm{fit}}_{c,j}$ for each field coordinate and position. The quantity to be minimized in the fit is:

$$\chi^2 = \sum_{i,c} \left(\frac{B^{\mathrm{measured}}_{c,i} - B^{\mathrm{fit}}_{c,i}(A_{nm}, a_n, \alpha_n, b_m, \beta_m, c_{nm}, \gamma_{nm})}{0.2\ \mathrm{G}} \right)^2 \tag{3.4}$$

where i runs over all measured points and the component index c is either x, y or z. The 0.2 G error is the expected intrinsic uncertainty of the Hall probes (see Figure 3.11). The error of the measurements are roughly the same for each of the components, as can be seen in Figure 3.19.

For the minimization, the MINUIT [131] code was used. Since the material of the basket is not completely non-magnetic and welds additionally distort the magnetic field, the regions close to the basket do not fulfill the criteria for the fitting function. Therefore, the fit is only applied in a central region of the mapped volume (with a minimum distance of 20 cm from the basket), where no distorting effects were observed. This central region is indicated in Figure 3.20. The value for χ^2/ndf is 3.95, which is consistent with an underestimation of the error by a factor of two. This is in agreement with values around 0.4 G for the RMS of the residuals, $B_{c,i}^{\text{measured}} - B_{c,i}^{\text{fit}}$, for each component and position. The fit appropriately describes the data, since this number is of the same order of magnitude as the intrinsic resolution of the Hall probes (0.2 G). Figure 3.19 shows the results of this quality measure for the central part of the mapped region. The best goodness of fit was seen for a second order polynomial. Going to higher orders does not improve the fit further. For the remaining parts of the mapped region, we rely on an interpolation between the measured data points. With a maximum distance of only 5.7 cm between two neighboring measurement points, a linear interpolation is sufficient to describe the data in that region. A slice of the final map for the main field component is shown in Figure 3.21.

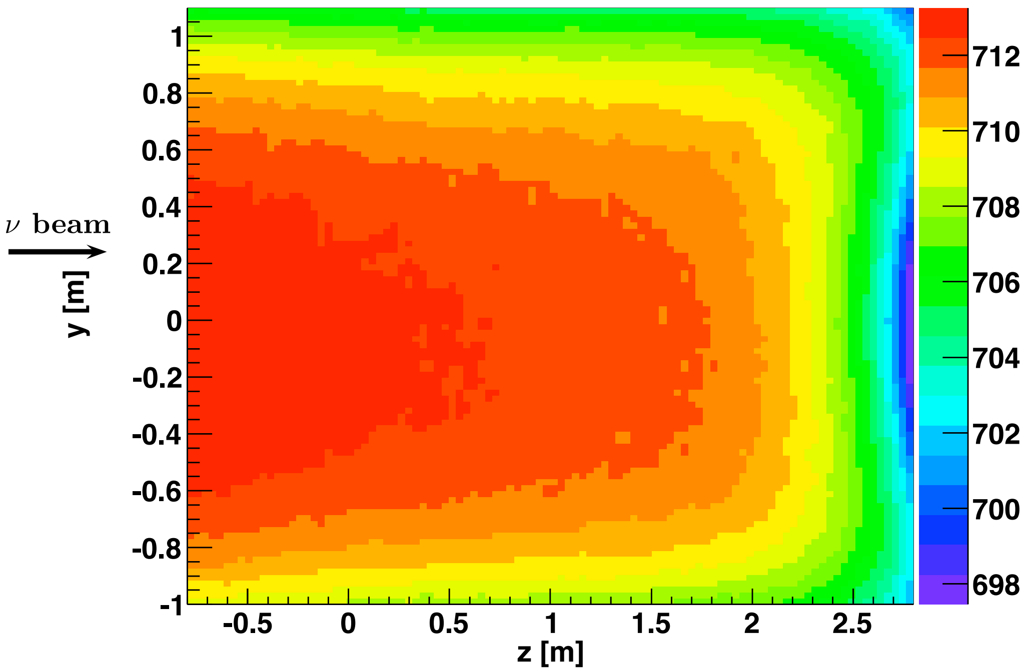

Figure 3.21: The plot shows a slice ($x = 0$ m) of the mapped B_x-field [G] in the TPC region. In the picture, the neutrino beam enters from the left.

Chapter 4

Study of Δ^{++} Resonances in the ND280 Tracker

The study of Δ^{++} resonances is motivated by two factors. Firstly, it can help to probe the momentum scale in the ND280 detector. Δ^{++} resonances were studied in detail in proton beam experiments [132, 133], and the invariant mass and the width of the resonance have been precisely measured in several experiments until today. This knowledge can be used to perform a check of the momentum scale in a detector by reconstructing the invariant mass. The selection of Δ^{++} events is derived in a study of Monte Carlo (MC) data and described in Section 4.1. Kinematical distributions to better understand signal and background are presented in Section 4.2. With this knowledge a simultaneous fit of signal and background events is performed to obtain the Δ^{++} invariant mass peak. A comparison for different hypothetical biases on the momentum completes this study and is used to determine the error on the momentum scale, as described in more detail in Section 4.3. A brief summary and outlook is presented in Section 4.4.

Secondly, Δ resonances are of great interest in neutrino interaction physics. They build the dominant part of resonant single pion production in the sub-to-few GeV neutrino energy region. Single pion production, in turn, is one of the three most important contributions (CC1π, CCQE, DIS) to the CC inclusive cross section in this energy region (see Figure 1.2). Understanding the composition and size of the inclusive cross sections is one of the major goals to reduce background uncertainties in this energy range, because this is the interesting region for the ν_e appearance searches in long baseline oscillation experiments. The work and the developed methods, which are presented in this chapter, can be used to help determining the cross section for the CC1π channel.

4.1 Selecting Δ^{++} Events

This section describes the cuts, which are applied to retrieve an efficient and a pure sample of Δ^{++} events. The first series of cuts are selection cuts, with the main purpose to reduce the amount of data to be looked at. Further cuts are used for particle identification to refine the selected sample. The cut chain and the choices of the corresponding threshold values are developed with the help of MC data. The studies are based on the neutrino interaction MC simulation program NEUT [29]. A comparison of real data with MC is presented in Section 4.3.

4.1.1 Topologies of Δ^{++} Events

The signature of Δ^{++} resonances in the ND280 tracker can look very differently. The produced Δ^{++} either are reabsorbed within the nucleus and thus invisible, or they decay into secondary particles (p, π^+), which form tracks in the detector. For CC muon neutrino interactions in one of the FGDs, the latter class of events can be divided in three major event topologies. If all involved particles (μ^-, p and π^+) possess enough energy, three tracks in the subsequent TPC will be seen. An example event of this case is shown in Figure 4.1. But it might also happen that one of the positive charged particles is absorbed within the FGD, leading to two more topologies. In one case, the proton track is fully contained in the FGD, and the other two particles escape to the TPC. Analogously, in the other case, the pion might deposit all its energy in the FGD, and the muon and the proton penetrate to the TPC. The μ^- is always required to be found in the downstream TPC, because Δ^{++} resonances are only produced in CC neutrino interactions.

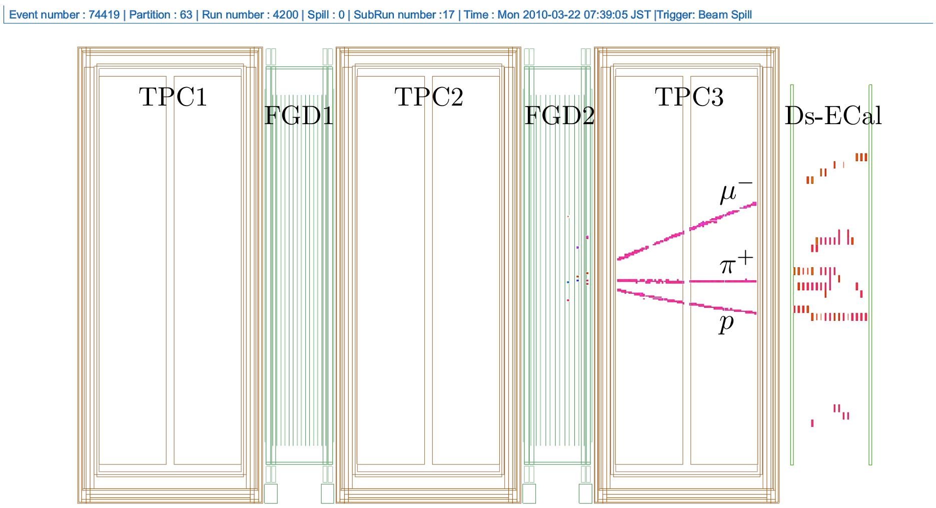

Figure 4.1: Candidate event for a Δ^{++} resonance from a charged current ν_μ interaction occurring in FGD 2, with three tracks penetrating into the subsequent TPC, also forming tracks and showers in the Ds-ECal.

A feasibility study with NEUT MCP1[a] was performed to check if a study of Δ^{++} resonances can be useful to constrain the momentum scale of ND280. The preferred event topology for more detailed can also be inferred. The relative rates and the corresponding purities of the three above-mentioned event topologies are reported in Table 4.1.

[a]Monte Carlo Production 1 is the first of various stages in the simulation of neutrino events in the ND280 detector, including the neutrino beam simulation.

The sample with 3 tracks penetrating into one of the TPCs has the highest efficiency. It is best suited for studying kinematical variables, because of the momentum resolution and PID performance of the TPCs. This implies the possibility of identifying and reconstructing the involved particles, which is necessary for the envisaged check of the momentum scale. The further analysis will concentrate on this type of events.

Table 4.1: Relative rate of Δ^{++} events and purity values from the feasibility study with MCP1 data for the three samples with different Δ^{++} resonance event topologies. The relative rate is the number of Δ^{++} events with a certain topology divided by the number of Δ^{++} events of all three topologies together. The purity is the ratio of selected Δ^{++} events with respect to all selected events.

Sample	Δ^{++} relative rate	Δ^{++} purity
3 TPC tracks	62.4%	29.5%
proton in FGD	21.7%	46.1%
pion in FGD	15.9%	34.9%

4.1.2 Monte Carlo Data Production

For the detailed study, more realistic MC data is used, namely events from MCP-4C[b]. The MC data describe the status of software, beam configuration, and detector simulation as of autumn 2011. The MC samples can be divided in three different groups:

- MC-magnet: Monte Carlo data with neutrino interactions in the full ND280 detector including the magnet.
- MC-basket: Monte Carlo data where interactions only occur in the subdetectors inside the magnet, namely PØD, FGDs, TPCs and ECals.
- MC-ccpiplus: a special Monte Carlo sample of charged current neutrino interactions with a π^+ and no other mesons in the final state.

All three samples are divided into two subsamples: a sample in which the PØDis simulated to be filled with water, and one without water. The two subsamples are added for the analysis in this thesis, as only interactions in the FGDs are considered. There is no background from interactions in the PØDfor the selected sample of Δ^{++} events. The MC-magnet sample is further divided in data for two run periods. RUN 1 corresponds to the real setup for the data taking between January and June 2010, where the Ds-ECal was the only installed ECal module, and the neutrino beam was delivered in spills of six bunches at an average beam power of $\sim$50 kW. RUN 2 describes the setup for data taking between

[b]MCP-4C is a Monte Carlo sample, which was produced in the fourth major production of MC data for neutrino interactions in ND280. The letter C stands for respin C, the third iteration of the production.

November 2010 and March 2011 with an increased beam power of ∼100 kW, which was partly achieved by increasing the number of bunches from six to eight. During RUN 2, all ECal modules were installed into the ND280 detector. The number of protons on target (POT) for each of these MC subsamples and for real data are reported in Table 4.2.

Table 4.2: List of protons on target for each of the MC and real data samples.

<table>
<tr><th>sample</th><th>PØD water</th><th>run configuration</th><th>POT [10^{20}]</th><th colspan="2">combined POT [10^{20}]</th></tr>
<tr><td>MC-magnet</td><td>in</td><td>RUN 1</td><td>5.45</td><td>5.45</td><td rowspan="5">49.61</td></tr>
<tr><td>MC-magnet</td><td>in</td><td>RUN 2</td><td>11.02</td><td rowspan="2">21.99</td></tr>
<tr><td>MC-magnet</td><td>out</td><td>RUN 2</td><td>10.97</td></tr>
<tr><td>MC-basket</td><td>in</td><td>RUN 2</td><td>11.08</td><td rowspan="2">22.17</td></tr>
<tr><td>MC-basket</td><td>out</td><td>RUN 2</td><td>11.09</td></tr>
<tr><td>real data</td><td>in</td><td>RUN 1</td><td>0.294</td><td rowspan="2">1.064</td><td rowspan="2">1.064</td></tr>
<tr><td>real data</td><td>both</td><td>RUN 2</td><td>0.771</td></tr>
</table>

4.1.3 Selection Cuts

To select Δ^{++} events, a series of selection and veto cuts need to be applied. The cuts are listed below and are explained in more detail afterwards. Table 4.3 summarizes the efficiency and purities of the cuts, which are obtained from the full combined MC-magnet and MC-basket sample:

1. Same Bunch.
2. Track quality.
3. Exactly 1 Vertex in FGD.
4. FGD fiducial volume.
5. At least 3 TPC tracks.
6. 2 positive tracks and 1 negative forward TPC tracks from vertex.

to 1: One beam spill is divided into six (RUN 1) or eight bunches (RUN 2). The bunches are separated by 582 ns, and each bunch has a duration of 58 ns. Only events and particle tracks which fall into the timing window of a beam bunch are considered.

to 2: The track quality cut consists of two parts. Firstly, all tracks containing a TPC segment must fulfill the criteria of having a minimal reconstructed momentum of 50 MeV, to reject noise. Secondly, the highest energetic negatively charged track, the muon candidate track, is required to have at least 18 hits in the TPC segment nearest to to the vertex. This cut is based on studies of a CC inclusive sample for the ND280 tracker [134]. It ensures a good reconstruction of the muon candidate track to allow a pure selection of CC events.

to 3: The third cut requires exactly one vertex in the FGD, where a vertex is defined as the starting point of the muon candidate track, i.e. the most energetic negative track. Thus, it is naturally fulfilled for reconstructed data. Additionally, for MC data, this cut requires to have at most one true vertex per FGD in order to avoid a wrong association of reconstructed tracks with the true vertex.

to 4: The vertex must be in a fiducial volume (FV), which is again based on the cuts for the CC inclusive selection. This cut is needed to reject particle tracks, which are produced in the surrounding material of the FGD. These tracks can be mistaken as starting in the FGD border regions. Slight variations of the FV do not bias the obtained distributions when comparing MC and real data. The chosen dimensions for the FV are:

$|\mathrm{x}| < 0.875\,\mathrm{m}$,
$|\mathrm{y} - 0.55\,\mathrm{m}| < 0.875\,\mathrm{m}$,
$0.137\,\mathrm{m} < \mathrm{z} < 0.447\,\mathrm{m}$ for FGD 1
or $1.482\,\mathrm{m} < \mathrm{z} < 1.810\,\mathrm{m}$ for FGD 2.

to 5: The minimal condition for obtaining a sample with a proton, a pion and a muon track in the TPC is to have at least three TPC tracks. All three tracks together are necessary to select CC events and reconstruct the Δ^{++} invariant mass.

to 6: Finally, one negative track and two positive tracks must come from the same vertex. This cut rejects background tracks, which stem from different interactions. These tracks are required to reach the subsequent TPC. In principle, also events with backward going tracks can be studied, but this introduces additional complications related to charge confusion and the correct vertex association of tracks.

4.1.4 PID Cuts

The particle identification (PID) in the ND280 Tracker, with the help of the so-called pull variable, is well established for CCQE events, as reported in [134]. The pull variable describes the deviation of the measured from the expected energy deposit of a track with a certain particle hypothesis (in terms of standard deviations). It is defined as:

$$\delta_\alpha = \frac{\bar{C}_T - C_{E,\alpha}}{\sigma_{0,\alpha}},$$

where α is the particle hypothesis (e.g. a muon), $\bar{C}_T$ is the calibrated truncated mean energy deposit, $C_{E,\alpha}$ is the expected energy deposit for a particle hypothesis α and

$$\sigma_{0,\alpha} = \sigma_{T,\alpha} \oplus (dC_E/dp)\sigma_p$$

Table 4.3: Efficiency and purity breakdown of the preselection cuts. All selected events and true Δ^{++} events are shown seperately. Efficiency is defined as the number of true Δ^{++} events after a cut divided by the number of Δ^{++} events after the track quality cut. The purity is the number of Δ^{++} events divided by all selected events. In the upper table, the numbers are reported for the combined MC-magnet sample for RUN 1 and RUN 2 together. The lower table shows the corresponding values for the MC-basket sample.

MC-magnet					
cut nr.	cut name	all events	true Δ^{++}	efficiency	purity
1 & 2	track quality	586645	38760	100.0%	6.6%
3	1 true FGD vertex	268786	38616	99.6%	14.4%
4	vertex in FGD FV	218632	31373	80.9%	14.3%
5	$\geq$ 3 TPC tracks	62108	9134	23.6%	14.7%
6	2pos and 1neg	9511	2390	6.2%	25.1%

MC-basket					
cut nr.	cut name	all events	true Δ^{++}	efficiency	purity
1 & 2	track quality	325053	31923	100.0%	9.8%
3	1 true FGD vertex	221489	31923	100.0%	14.4%
4	vertex in FGD FV	181069	26003	81.5%	14.4%
5	$\geq$ 3 TPC tracks	49959	7499	23.5%	15.0%
6	2pos and 1neg	8063	2168	6.8%	26.9%

is the total width. σ_T is the variance of $\bar{C}_T$, and σ_p is the uncertainty of the momentum measurement [135].

Using the same pull variable cuts as for the CCQE case is not necessarily the best choice when studying other samples, such as resonant particle production. The cut values for different particle hypotheses, presented in Table 4.4, are the basis for PID cut studies. First, the negative charged track is extracted and checked if it is a muon to identify CC candidate events. Then, positive charged tracks are investigated. e^+ candidates are rejected and π^+ candidates selected. The remaining positive track is accepted when it is compatible with a proton.

Table 4.4: Pull cuts for particle identification.

	$\boldsymbol{\mu^-}$	$\boldsymbol{\pi^+}$	**p**
charge	-1	+1	+1
$\|\delta_\mu\|$	< 2.5		
$\|\delta_e\|$	> 2	> 2	> 2
$\|\delta_\pi\|$		< 2.5	
$\|\delta_p\|$			< 2.5

This basic selection lacks to implement the full information, which can be obtained for each track. In order to select Δ^{++} events more efficiently, several possibilities of improvements of the PID have been studied, such as: setting a threshold value, e.g. the use of a different pull cut value for tracks with a momentum above 1.5 GeV; assuming that one of the two positive particles is a proton and match the other track; or looking at the momentum ratio of the two positive particles.

For the analysis presented in this thesis, a likelihood method has been adopted, which uses the pull variables for different particle hypotheses and combines the obtained information. This method guarantees a good PID association, while decreasing the Δ^{++} efficiency only marginally. It is described in more detail below. With Bayes' theorem, the probability of having a particle α given a pull value δ_β for a particle hypothesis β with a certain energy E can be expressed as the likelihood:

$$L_{\alpha,\beta} = Pr(\alpha|\delta_\beta) = \frac{N_\alpha \cdot Pr(\delta_\beta|\alpha)}{\sum_i N_i \cdot Pr(\delta_\beta|i)}, \tag{4.1}$$

where all terms are energy dependent; i is an index running over all particle hypotheses which are taken into account; N_i is the number of true particles i at energy E; $Pr(\delta_\beta|\alpha)$ is the probability of having a certain pull value for hypothesis β, given the true particle at energy E is of type α. These conditional probabilities of the pull distributions need to be known a priori. Because detector effects, e.g. acceptance or energy resolution, need to be taken into account, these distributions are obtained from simulated data.

Equation 4.1 can be used to discriminate between the pion and the proton by calculating the likelihood for each particle hypothesis. Because only two particles (p, π^+) need to be distinguished, it is sufficient to look at two particle hypotheses and two pull values. The ratio of the two likelihoods, $R_{p,\pi} = L_{p,\pi}/L_{\pi,p}$, can be used as the discriminating number. This also guarantees a proper normalization. The general expression for two particle hypotheses α and β is:

$$R_{\alpha,\beta} = \frac{Pr(\alpha|\delta_\alpha) \cdot Pr(\alpha|\delta_\beta)}{Pr(\delta_\beta|\alpha) \cdot Pr(\delta_\beta|\beta)} \tag{4.2}$$

If $R_{\alpha,\beta} > 1$, or equivalently $\ln(R_{\alpha,\beta}) > 0$, then particle α is more likely to be realized, otherwise particle β. However, these probabilities are dependent on the selected sample and the cut value needs to be optimized. For example, the pull value is not a good discriminator for energies above 1.5 GeV, because the energy loss due to ionization for protons and pions is comparable in the high energy tail of the Bethe formula [136].

Figure 4.2 shows the discrimination power of the above presented likelihood ratio method for the combined MC-magnet and MC-basket sample, after applying the bunch and the track quality cut. The protons and pions are well separated except for the overlap region ($-2 \lesssim \ln(R_{\pi,p}) \lesssim 0$).

Analogously, a likelihood cut is introduced to reject positron tracks. The cut value is chosen to be $\ln(R_{p,e}) > 0$ or $\ln(R_{\pi,e}) > 0$ for the proton and pion hypothesis, respectively.

Finally, it is also required that the angle between the proton and the pion $\psi(p, \pi)$ differs from zero. This excludes single tracks, which are erroneously broken into two tracks in the reconstruction algorithm.

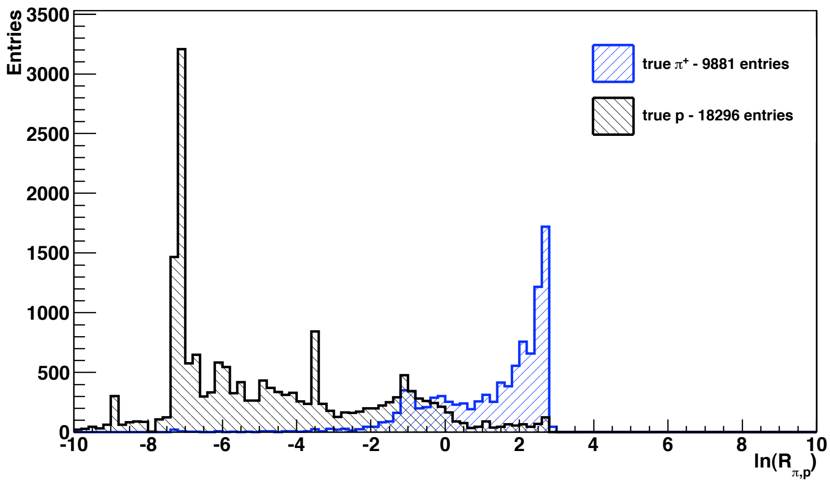

Figure 4.2: The logarithmic likelihood ratio values for true protons (black) and π^+ (blue) are shown. The TPC tracks for this plot are selected from the combined MC-magnet and MC-basket sample after the track quality cut. The particles can be well distinguished except for the overlap region ($-2 \lesssim \ln(R_{\pi,p}) \lesssim 1$).

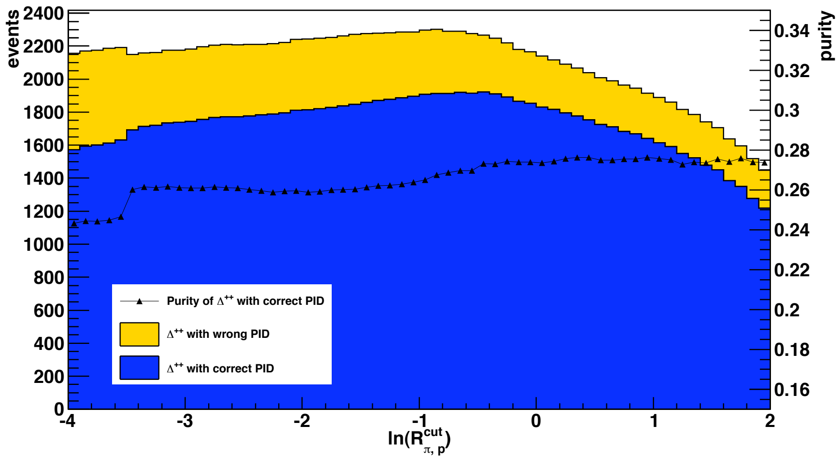

Figure 4.3: The plot shows the number of selected Δ^{++} events (left scale) as a function of the chosen cut value for the logarithmic likelihood ratio $R_{\pi,p}$. The selected Δ^{++} events with a correct association of the reconstructed track to the true particle are shown in blue, the selected Δ^{++} with a wrong association are shown in yellow. The black triangles indicate the purity (right scale), which is defined as the ratio of correctly associated Δ^{++} tracks over all tracks passing the selection cuts. This includes background events which are not shown in the colored stack histogram. The combined MC-magnet and MC-basket sample is used. The cut value which maximizes the number of correctly associated Δ^{++} events, $R^{\mathrm{cut}}_{\pi,p} = -0.5$, is chosen for the further analysis.

Table 4.5 summarizes the number of events of a correct association of the particle hypotheses with the true particles. All events are divided into two sets. Signal events are events with the correct MC interaction code, i.e. true Δ^{++} events. Background events are all other neutrino interactions, in which no Δ^{++} resonance is produced. For each of the two sets, the number of events are reported, which correctly associate the proton and the pion with the true particles, labeled as "correct PID". The corresponding purities and efficiencies are also written. The efficiency is the number of correctly associated Δ^{++} events with respect to the case without any applied PID cut (2pos and 1neg). The purity is the ratio of correctly associated events over all events remaining after the cut.

Table 4.5: Association of reconstructed p- and π^+-tracks to the true particle tracks. For the PID of the negatively charged particle, the μ^- pull cut is chosen. The positively charged tracks are best associated with the likelihood cut. Additionally, positrons are rejected on a likelihood-based cut. The proton and pion track are required to have a non-zero angle with respect to each other. The combination of all these cuts leads to the final sample (last line of the table).

cut name	all events	all Δ^{++}	Δ^{++} with correct PID	efficiency	purity
2pos and 1neg	17574	4558	1892	100.0%	11.1%
μ^- pull	14895	4180	1892	100.0%	12.7%
& e^- rejection	12708	3613	1663	87.9%	13.1%
p and π^+ pulls	4346	1390	1056	55.8%	24.3%
& e^+ rejection	2870	917	706	37.3%	24.6%
p and π^+ likelihood	7586	2340	1883	99.5%	24.8%
& e^+ rejection	7058	2280	1883	99.5%	26.7%
& $\psi(p,\pi) \neq 0$	6887	2257	1883	99.5%	27.3%

4.2 Kinematical and Other Distributions

After applying the preselection and the PID cuts, 2257 Δ^{++} events are selected, of which 1883 events have the correct particle association (μ^-, p and π^+). The final signal purity is therefore $1883/6887 = 27.3\%$, as shown in Table 4.5. The 374 Δ^{++} events with a wrong PID association are considered as background, because they would bias the kinematical distributions discussed below. For the purposes of checking the momentum scale, the distribution of the reconstructed Δ^{++} invariant mass is interesting, which is shown in Figure 4.4. The Δ^{++} invariant mass can be reconstructed from the momentum of the π^+ and the p which are produced in the decay $\Delta^{++} \to p + \pi^+$:

$$m_{\text{inv}}(\Delta^{++}) = \sqrt{(E_p + E_\pi)^2 - (\vec{p_p} + \vec{p_\pi})^2}.$$

The peak of the signal events around the expected invariant Δ^{++} mass of 1.232 GeV [16] is background dominated with deep inelastic scattering (DIS)[c] events as the main contributors.

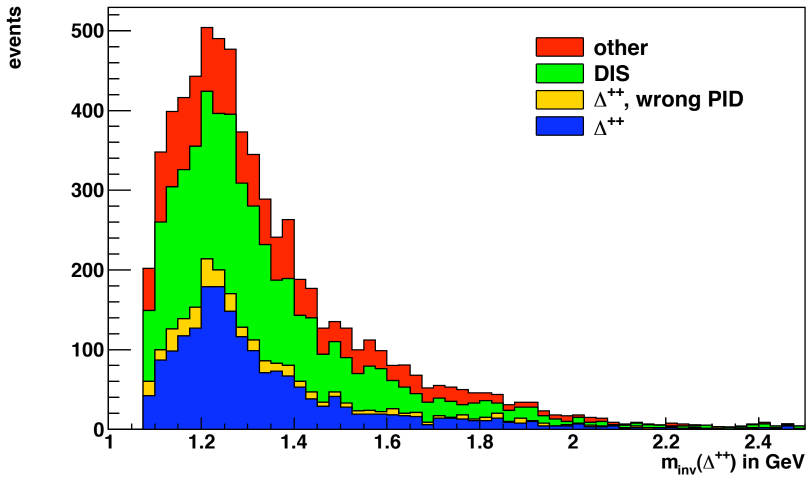

Figure 4.4: Reconstructed invariant mass under the Δ^{++} resonance hypothesis for events passing the selection cuts. The colors of the stacked histogram indicate the different types of interactions. The signal consists of Δ^{++} events with correct particle association (blue). The background is formed from Δ^{++} events with an incorrect particle association (yellow), DIS events (green) and all other backgrounds (red).

Because of its large number of events, the background is studied in more detail. Extended cuts are derived as well as fitting methods, based on several reconstructed kinematical variables, which are discussed in more detail below the following list:

E_ν - the neutrino energy;

Q^2 - the four momentum transfer from the neutrino to the target nucleus;

p_T - the transverse momentum of the neutrino;

$\psi(p, \pi^+)$ - the angle between the two decay particles (p and π^+) of the Δ^{++};

$\phi(\Delta^{++}, \mu^-)$ - the angle between the reconstructed momentum of the Δ^{++} and the muon.

The reconstructed neutrino energy

$$E_\nu = |\vec{p}_\nu| = |\vec{p}_\mu + \vec{p}_p + \vec{p}_\pi|$$

is shown in Figure 4.5. As intuitively expected, in average Δ^{++} events are less energetic than DIS events, in which, in general, more particles are produced.

[c]The definition of DIS in NEUT is events with an invariant mass of the hadronic system $W > 1.3$ GeV and more than one pion for $W < 2$ GeV to avoid double counting of CC1π events.

Often, not the complete neutrino energy can be reconstructed for DIS events, as can be seen in Figure 4.6. The missing reconstructed energy indicates a lack of identified particle tracks. This can be caused by reabsorption of short-living fragments of the target nucleus. Also, not all particles reach the TPCs or they do not deposit enough energy. This can be the case for gammas or other neutral particles.

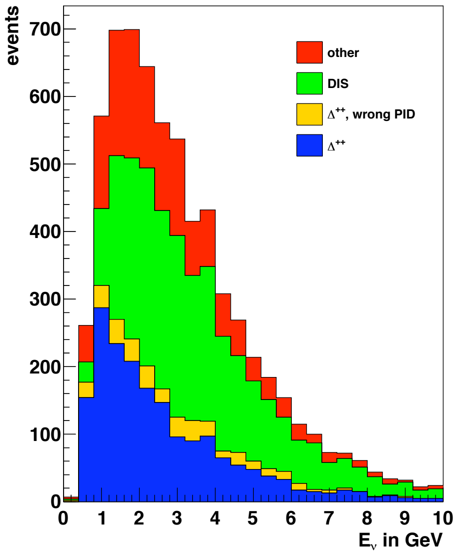

Figure 4.5: Reconstructed neutrino energy. The color coding is similar to Figure 4.4.

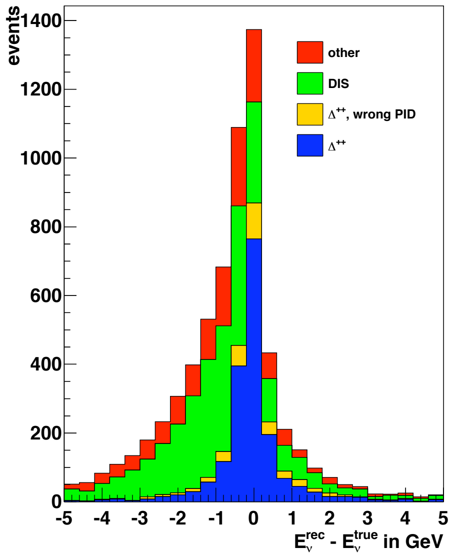

Figure 4.6: Residual of reconstructed and true neutrino energy. The color coding is similar to Figure 4.4.

The four momentum transfer is defined as:

$$Q^2 = 2E_\nu E_\mu(1 - \cos\theta_\mu),$$

with neutrino energy E_ν, muon energy E_μ, and the angle θ_μ between the muon direction and the expected neutrino beam direction. Because ND280 is close to the decay tunnel, in which the neutrinos are produced, and $\sim$2.5° off-axis to the central beam direction, the incoming neutrinos are not from a point-like source, but they have an angular distribution. The value for the expected neutrino direction is obtained from the full MC sample.The Q^2 distribution is suppressed for Δ^{++} events in comparison with DIS background for $Q^2 \lesssim 100\,\text{MeV}$, as shown in Figure 4.7. The Q^2 distribution is an important component for model building and the determination of form factors. However, for discriminating between signal and background of the Δ^{++} sample, the following properties are more powerful.

The reconstructed transverse momentum of the neutrino

$$p_T = |(\vec{p}_\mu + \vec{p}_p + \vec{p}_\pi)_{xy}|$$

can help to distinguish between Δ^{++} events and DIS background events, as shown in Figure 4.8. A too high value for p_T indicates an insufficient amount of reconstructed transverse momentum, which can happen when particles are missing in the reconstruction. For a point-like neutrino source and perfect reconstruction of all particles, the distribution is expected to show only the contribution of Fermi motion, which describes the motion of nucleons inside the target nucleus due to the Heisenberg uncertainty principle. The additional Fermi momentum gives a contribution of up to $\sim$200 MeV. The transverse momentum is calculated with respect to the expected neutrino beam direction.

The angle $\psi(p, \pi^+)$ also shows different characteristics for Δ^{++} and background events (Figure 4.9). In the center of mass reference frame of the Δ^{++}, π^+ and p are back-to-back. Depending on the transfered momentum in the neutrino interaction, the Lorentz boost reduces the angle between the two particles in the laboratory reference frame. The higher the energy the narrower becomes the angle, such that the typically higher-energetic DIS events are more likely to have lower angles ψ. Additionally, the angle between p and π^+ is reduced when more than two particles are created, because p and π^+ are no longer back-to-back in the rest frame of the nuclear target system.

The variable $\phi(\Delta^{++}, \mu^-)$ can also help in separating the Δ^{++} signal events from background (Figure 4.10). The argumentation is analogous to the previous case. If no other particles are produced, then μ^- and Δ^{++} are back-to-back in the target nucleus rest frame. This angle is reduced if additional particles are produced. Fermi motion of the interacting nucleon smears the angular distribution.

The information of these kinematical variables is combined to obtain a sample with reduced background. Cuts for each of the variables are determined by maximizing a figure of merit. The chosen figure of merit is the product of purity (π) and the root of the number of signal events ($\sqrt{N_{\mathrm{sig}}}$). This choice differs from $\pi \cdot N_{\mathrm{sig}}$, which minimizes the expected statistical error of the measured quantity [137], but it enhances purity considerably. The study of combined cuts revealed that the application of simultaneous cuts on only two variables, p_T and $\phi(\Delta^{++}, \mu^-)$, are sufficient to maximize the figure of merit. The optimal cut values $p_T < 0.3$ GeV and $\phi(\Delta^{++}, \mu^-) > 0.9$ are obtained, as can be inferred from Figure 4.11.

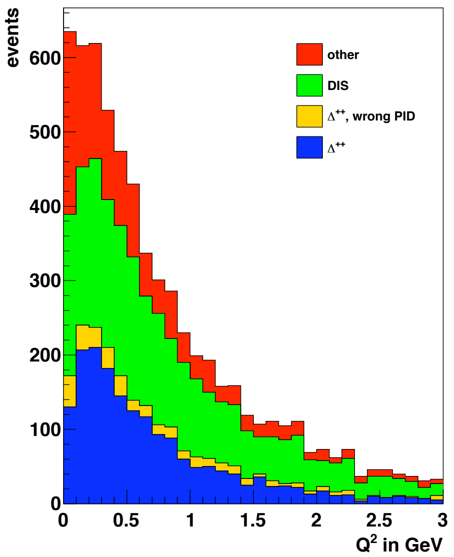

Figure 4.7: Reconstructed four-momentum transfer Q^2. The color coding is similar to Figure 4.4.

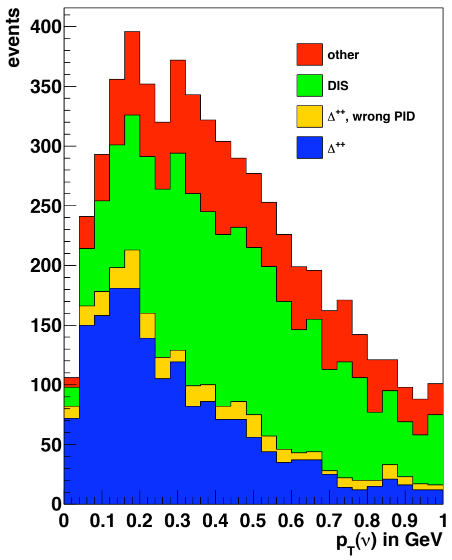

Figure 4.8: Reconstructed transverse momentum of the neutrino. The color coding is similar to Figure 4.4.

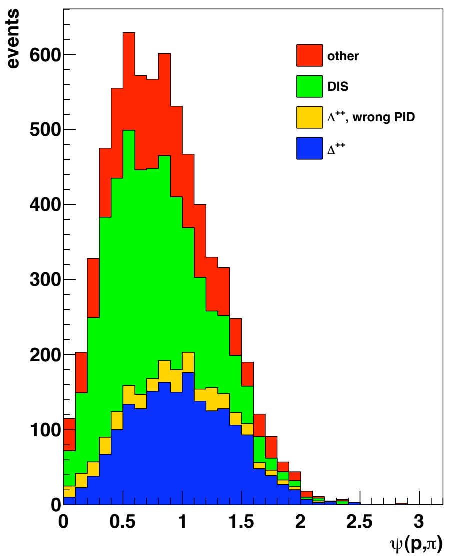

Figure 4.9: Reconstructed angle between proton and pion, the decay products of the Δ^{++} resonance. The color coding is similar to Figure 4.4.

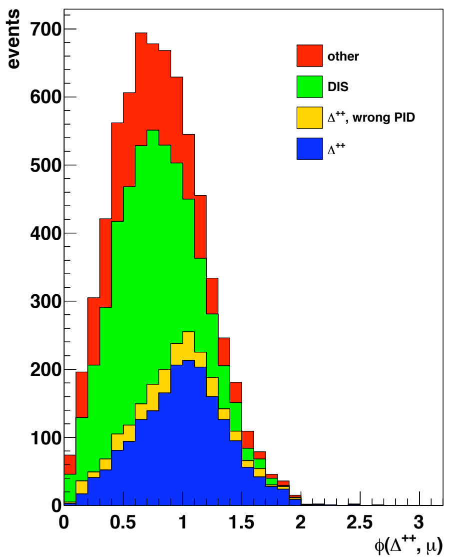

Figure 4.10: Reconstructed angle between Δ^{++} and the muon. The color coding is similar to Figure 4.4.

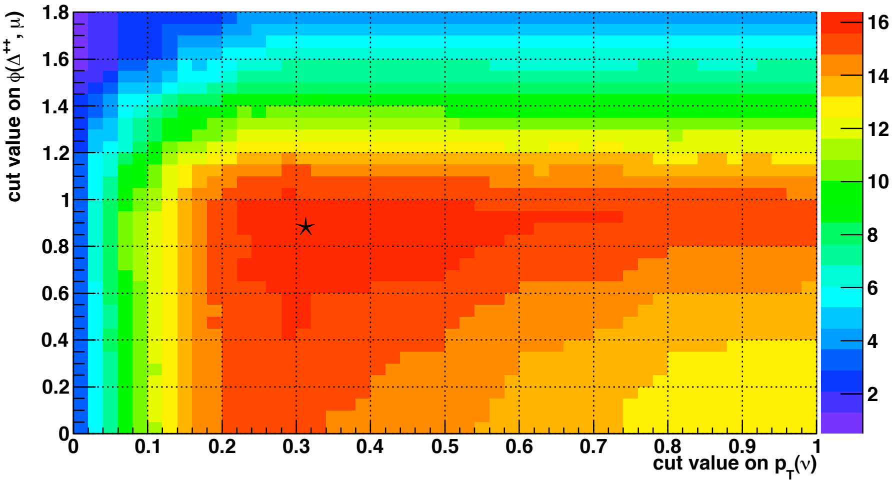

Figure 4.11: Determination of the optimal cut values for p_T and $\phi(\Delta^{++}, \mu)$. The colors indicate the value for the figure of merit $\pi \cdot \sqrt{N_{\mathrm{sig}}}$. The star ($\star$) marks the maximum value of the figure of merit. For p_T, all events above the corresponding cut value are rejected. Analogously, all events below the cut value for $\phi(\Delta^{++}, \mu)$ are rejected.

4.3 Fitting the Δ^{++} Invariant Mass Peak

As a result of the cut studies, two samples of Δ^{++} events are selected. A highly efficient sample with 39.6 Δ^{++} events per 10^{20} POT and a purity of 27.3%, and a sample with increased purity with 15.0 Δ^{++} events per 10^{20} POT and a purity of 60.1%. For each sample the invariant mass of the Δ^{++} can be reconstructed, which is shown for data and MC in Figure 4.12. Because of the low statistics of the latter sample, fits of the invariant mass peak are not robust. Therefore, the further analysis is only performed with the former, highly efficient sample.

Since the backgrounds are large, it is important to find appropriate fitting functions for the signal and the background. For the fitting procedure the RooFit [138] package is used. Figure 4.13 shows the signal and background events separately, each with the corresponding fitting function. The background distribution can be described by a Landau distribution, which fits better to the data than polynomials. For the fit of the Δ^{++} signal events, a Breit-Wigner function is used. It is important to note that the fitting functions are not analytically derived from the underlying processes. They are an empirical description and contain smearings and biases. These can occur due to final state interactions in the target nucleus, secondary interactions of the particles emerging the nucleus, and detector effects, such as geometrical acceptance and energy resolution.

Another approach is to use the obtained MC signal and background data without the description of an analytical fitting function. The directly obtained distributions for signal and background are fitted simultaneously to the measured data. In general, this method is preferred, because detector effects are described more accurately. But it requires a large set of MC interactions to ensure that

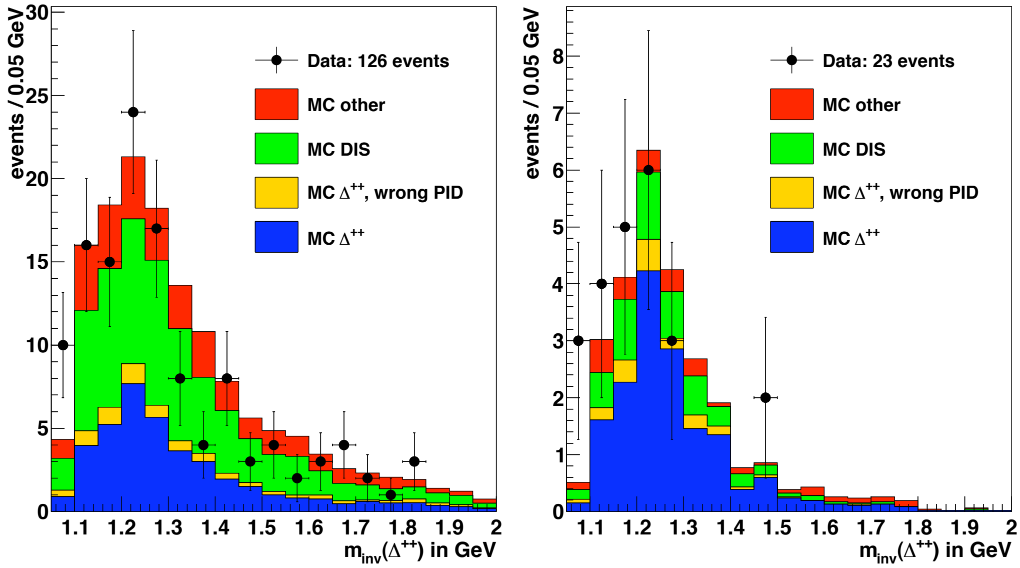

Figure 4.12: Comparison of the invariant mass of the reconstructed Δ^{++} between data and MC after the selection cuts (left) or kinematical cuts (right). The histograms are normalized to POT. Data events are represented by the black circles with statistical error bars. The color coding for MC events is similar to Figure 4.4.

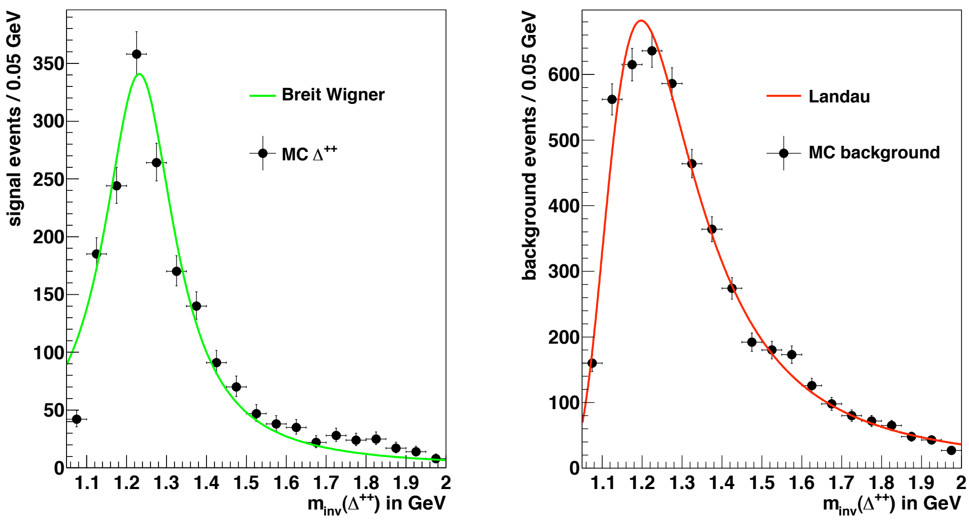

Figure 4.13: Left: The selected Δ^{++} events from MC data (black with errors) is shown together with a Breit-Wigner fit (green). Right: The remaining background events of the selected MC data (black with errors) is shown together with a Landau function (red), which is fitted to the data.

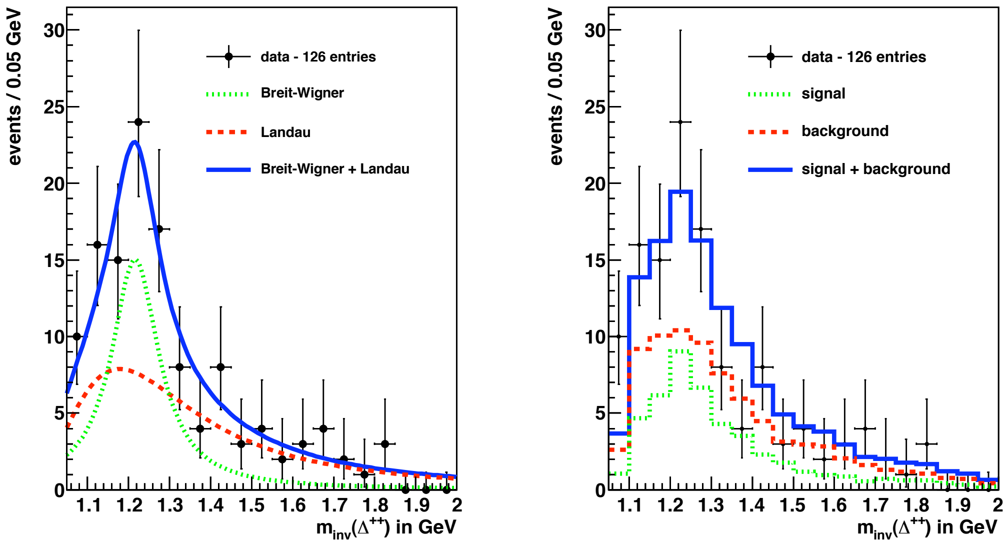

Figure 4.14: Two different fitting methods for the invariant mass of the selected Δ^{++} events (black circles with statistical error) are presented. The left plot shows a simultaneous fit (blue) of signal and background with a Breit-Wigner function (dotted green) and a Landau function (dashed red), respectively. The analogous fit functions in the right plot are obtained from the MC distributions directly.

statistical fluctuations do not form the dominant part of the error.

A comparison of the two fitting methods is presented in Figure 4.14. Both plots show the fits to the signal, the background, and the sum of signal and background distributions. The first method has the advantage that the fit parameters can be directly obtained. This allows to determine the peak value for the signal function together with the corresponding error. The second method describes the detector effects more accurately and shows a different composition of signal and background.

For the check of the momentum scale, the first method is applied. The parameters of the fit functions are constrained in a way, such that the composition of signal and background agrees with the results from the second fitting method. The widths of the signal and the background distributions are required to lie between 0.2 GeV and 0.5 GeV, and the ratio of signal to background events is fixed at 0.273, the purity of the MC sample. For the MC sample and the real data sample, a best fit value of $m_{\text{inv}}^{\text{MC}}(\Delta^{++}) = 1.218 \pm 0.013$ GeV and $m_{\text{inv}}^{\text{data}}(\Delta^{++}) = 1.207 \pm 0.025$ GeV is obtained, respectively.

This fit is repeated for different momentum biases. For this, the reconstructed momentum of all particles is shifted by a certain percentage. For example, a bias of 5% leads to a momentum: $p_{\text{bias}} = 1.05 \cdot p_{\text{data}}$. With the information from this newly reconstructed tracks, the combined fitting function is calculated anew, such that the peak value, the width and the shape are retrieved. For the check of the

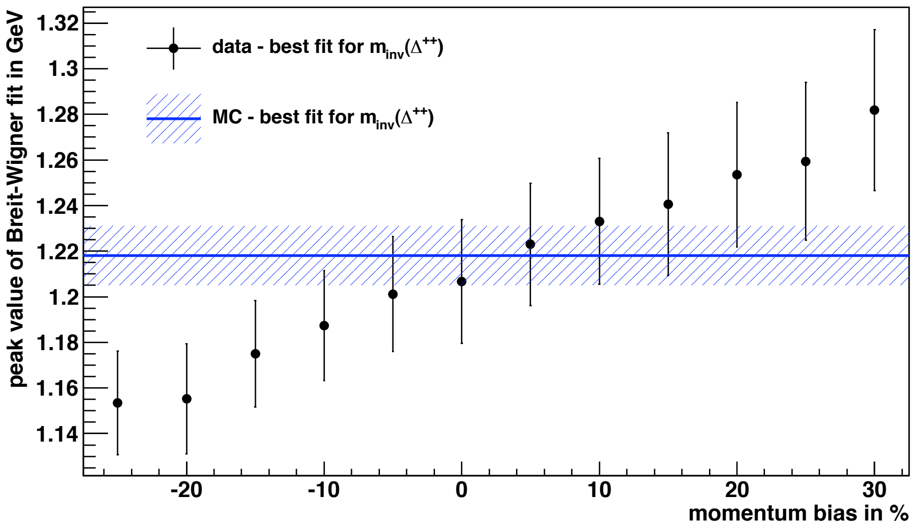

Figure 4.15: The best fit value for the Δ^{++} invariant mass peak (black circles) is plotted as function of momentum bias. The expectation from the MC data is also shown as a blue line. The shaded region indicates the error on the expectation value from the MC data.)

momentum scale only the fitted peak value and its error are used. The best fit values and errors for different moment biases between -25% and 35% are shown in Figure 4.15. The distribution with a momentum shift of 4% agrees best with the expectations from the MC sample. If only the peak value is taken as the quantity of interest, momentum shifts between -7% and 18% agree with the best fit value from the MC data within $1\,\sigma$.

4.4 Summary and Outlook

In this chapter, a method to select Δ^{++} events in the ND280 tracker was presented. A likelihood based PID selection method was developed to select Δ^{++} events with high efficiency. Combined with the information from different kinematical variables, a subsample with a high purity can also be selected. With both types of selections the invariant mass of the Δ^{++} invariance mass can be reconstructed. The comparison of data and MC shows a good agreement, although the number of selected data events is still limited. The information of two different fitting methods can be used to extract the Δ^{++} invariance mass peak from the background dominated data sample. On the one hand, empirical fitting functions can describe the shape of the signal and background distributions. On the other hand, a binned likelihood fit helps to constrain the fitting function parameters, such as the width and the expected peak position of the combined fitting function. The fitted peak position of the signal distribution provides a physical quantity, which is appropriate to use for probing the momentum scale of the detector. By varying the reconstructed momentum of particle tracks, the agreement of the invariant mass peak position with the expectation from MC data is checked. The peak value of the signal distribution for a momentum bias between -7% and 18% is consistent with the expected peak value.

With increasing statistics in the upcoming run periods of T2K, the power of this check will improve. In the future, the presented method of selecting Δ^{++} events as well as the study of kinematical variables can help to determine the Δ^{++} production rate. The methods can also be used to constrain the CC1π cross section, e.g. by comparing the production rates in water and carbon.

Conclusions

A measurement of the magnetic field of the ND280 near detector in the T2K experiment was performed. For this purpose, a dedicated, automated device formed from non-magnetic materials, and equipped with Hall probes, has been designed, built and tested. During the measurement campaign in September 2009, the ND280 magnet provided a ~700 G dipole magnetic field. A measurement accuracy of ~1 G is obtained from a three dimensional mapping of the ND280 inner detector volume. This precision is ensured by the careful calibration procedure of each Hall probe in a reference magnetic field. The systematic errors of the measurement are evaluated for the extrapolation to the nominal ND280 magnetic field of 2000 G (0.2 T). This results in an accuracy of better than 2 G for the transverse magnetic field components (B_y, B_z). The systematic error of the main component is evaluated to be $\sigma(B_x) = 11.72$ G for a field of $B_x = 2048.14$ G in the center of the magnet, which corresponds to a magnetic field scale uncertainty of 0.57%. The modulus of the magnetic field and its error varies with less than 1% in the instrumented detector region, except for the regions which are close to the coils, where the field drops by up to 5%. The precise knowledge of the magnetic field meets the requirements for the ND280 TPCs to achieve a momentum accuracy of better than 2%.

The reconstruction of the Δ^{++} invariance mass peak is used to probe the momentum scale of the ND280 detector. For this purpose the data from the 2010 and 2011 neutrino beam runs is used. A sample of CC muon neutrino interactions in the ND280 tracker is selected, in which Δ^{++} resonances are produced ($\nu_\mu p \rightarrow \Delta^{++} \mu^- \rightarrow p\pi^+\mu^-$). The event topology of one negatively charged and two positively charged tracks in the TPCs, with all tracks coming from the same vertex in the FGD fiducial volume, is used to study this type of events. With the help of the TPC PID performance and a likelihood method, which has been developed to correctly identify protons and pions, 126 candidate events with an expected signal purity of 27.3% are selected from the data. The combined neutrino flux of the data taking period corresponds to 1.064×10^{20} POT. Another sample of 23 events with an enhanced expected purity of 60.1% is selected by exploiting the information from various kinematical variables. These are: the reconstructed neutrino energy, the transverse momentum of the neutrino, the angle between the μ^- and the Δ^{++}, and the angle between the Δ^{++} decay products p and the π^+. The reconstructed invariant mass for both samples agree with the expectations from a MC study. Because of the higher number of signal events and less biases on the kinematics, the more efficient sample with 126 candidate events is chosen to be used to check the momentum scale of the detector. For this purpose, the signal and background are fitted simultaneously with functions which are derived from the MC study. The peak value of the Δ^{++} signal distribution is compared to the expected value $m_{\mathrm{inv}}^{\mathrm{MC}}(\Delta^{++}) = 1.218 \pm 0.013\,\mathrm{GeV}$. The value of $m_{\mathrm{inv}}^{\mathrm{data}}(\Delta^{++}) = 1.207 \pm 0.025\,\mathrm{GeV}$, which is retrieved from the data, is compatible with the expectation within one standard deviation. This feature holds for momentum biases between -7% and 18%.

Appendix A

Appendix

A.1 Additional Checks and Plots for the Alignment Correction

The a posteriori correction of the alignment between the Hall probes is a delicate issue. Care must be taken to not introduce a bias to the data by putatively improving the error. Therefore, additional cross-checks are reported in this section.

Figures A.1 and A.2 show the mean values and the error of the mean for the transverse B-field components for different xy- and xz-slices of the ND280 TPC region. By construction, the mean values should not change before and after the correction. This can be verified for B_y, where the mean value for all slices is compatible with zero before and after the correction. However, for B_z, there seems to be a small shift before and after the alignment corrections. The fact that the mean of B_z differs from zero may be explained by a misalignment between the x-axis and the direction of the main component of the magnetic field. A difference of 1 G corresponds to a rotation of 1.4 mrad. But there also seems to be an increase in the mean of B_z with rising z values.

For both B_y and B_z, the errors become smaller because of the alignment corrections. To see this, one needs to compare the error bars for B_y in the xz-planes and for B_z in the xy-plane (see the top left and bottom right plots in Figures A.1 and A.2). The errors of the other two plots show the variation of the transverse B values and are expected to be different from zero. However, the mean values are expected to be constant in the other two plots, which is the case (top right and bottom left).

Furthermore, it can be confirmed that indeed the planes of symmetry were used for the correction method. In the symmetry planes, the error of the mean is expected to be lowest after the correction. For B_y, this is clearly the plane where y=0 (top left plot of Figure A.2), for B_z this is not so obvious. But for B_z the variation remains small for a wide range of xy-planes around z=0. This means that the correction method is not sensitive to small deviations from the true symmetry plane.

Another check to see a possible rotation of the mapping device reference system with respect to the main B-field direction, is to look at the slices orthogonal to

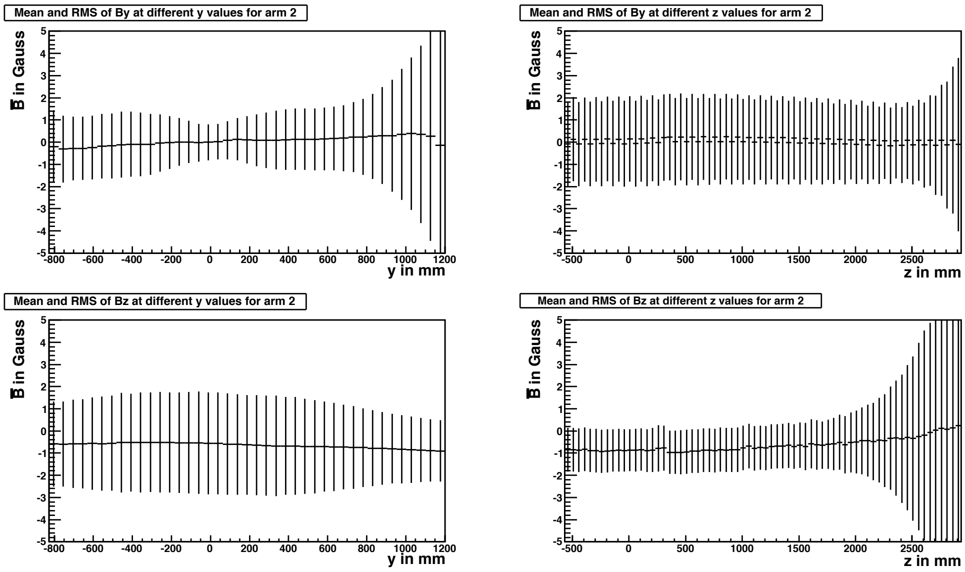

Figure A.1: The mean value and the error of the mean for B_y (top plots) and B_z (bottom plots) for different xz-slices (left plots) and xy-slices (right plots) before the alignment corrections are shown.

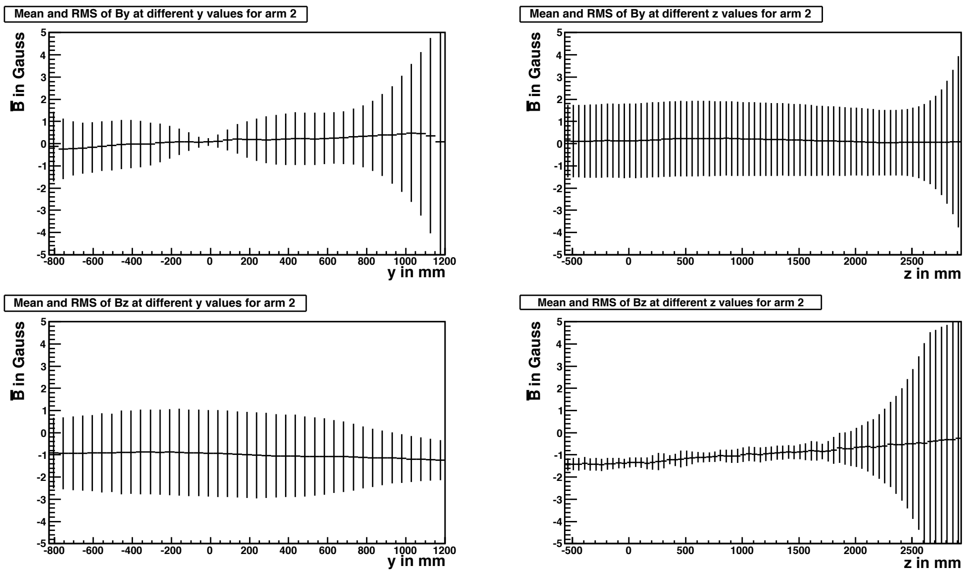

Figure A.2: The mean value and the error of the mean for B_y (top plots) and B_z (bottom plots) for different xz-slices (left plots) and xy-slices (right plots) after the alignment corrections are shown.

the one of the symmetry planes. For B_y, this could be for example the xy-slice with z=0. For B_z, the xz-plane with y=0 is chosen analogously. These planes are shown in Figure A.3 before the correction, and in Figure A.4 after the correction.

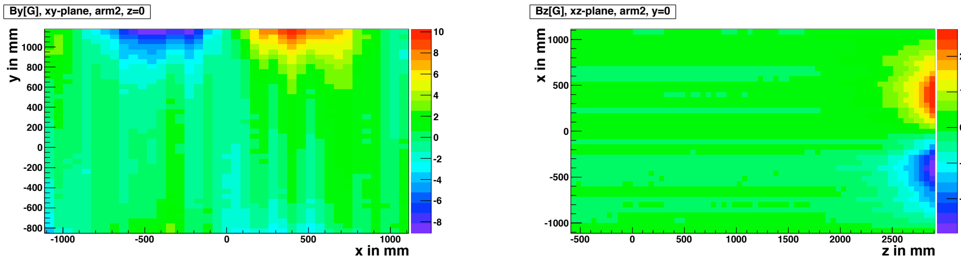

Figure A.3: Transverse B-field values before alignment correction in the planes orthogonal to the symmetry planes for B_y at $z = 0$ (left) and B_z at $y = 0$ (right).

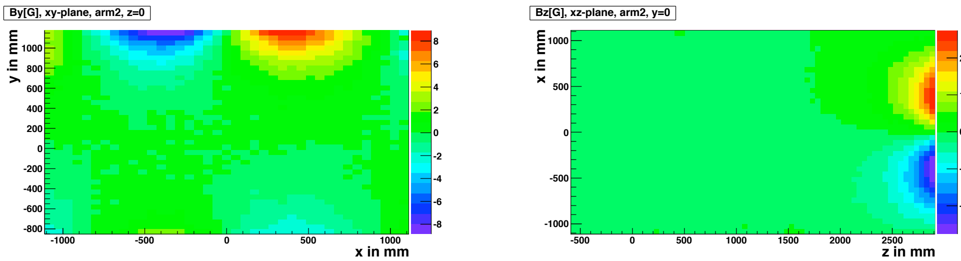

Figure A.4: Transverse B-field values after alignment correction in the planes orthogonal to the symmetry planes for B_y at $z = 0$ (left) and B_z at $y = 0$ (right).

A.2 Error Propagation for B-field Extrapolation

The error propagation starts from Equation 3.2:

$$B[G] = c_0 + c_1 I (1 + c_2 I)$$

Three parameters (c_0, c_1, c_2) and their errors $(s(c_i) = s_i)$ are retrieved from the fit. To propagate the errors properly, the correlations $\rho(c_i, c_k) = \rho_{ik}$ have to be taken into account:

$$s^2(B) = \sum_{i=0}^{2} \left(\frac{\partial B}{\partial c_i} s_i \right)^2 + \sum_{i \neq k} \frac{\partial B}{\partial c_i} \frac{\partial B}{\partial c_k} \rho_{ik} s_i s_k = \sum_{i=0}^{2} \sum_{k=0}^{2} \frac{\partial B}{\partial c_i} \frac{\partial B}{\partial c_k} \mathrm{cov}(i,k)$$

with the covariance matrix elements $\mathrm{cov}(i,k) = \rho_{ik} s_i s_k$ and the partial derivatives

$$\frac{\partial B}{\partial c_0} = 1, \quad \frac{\partial B}{\partial c_1} = I + c_2 I^2, \quad \frac{\partial B}{\partial c_2} = c_1 I^2$$

We therefore get:

$$\begin{aligned} s^2(B) = \; & s_0^2 + (I + c_2 I^2)^2 s_1^2 + (c_1 I^2)^2 s_2^2 + \\ & + 2(I + c_2 I^2) \rho_{01} s_0 s_1 + 2 c_1 I^2 \rho_{02} s_0 s_2 + 2 c_1 I^2 (I + c_2 I^2) \rho_{12} s_1 s_2 \end{aligned}$$

For the fit to 2900 A, the following fit values and correlation matrix R are retrieved. R turns out to be identical for the fit for each of the four permanent probes at the level of 10^{-3} .

parameters	probe 101	probe 102	probe 103	probe 105
$\mathbf{c_0}$ [**G**]	0.82 ± 0.24	0.78 ± 0.13	-2.23 ± 0.34	-0.72 ± 0.57
$\mathbf{c_1}$ [G kA^{-1}]	742.3 ± 0.31	741.9 ± 0.17	742.6 ± 0.44	745.0 ± 0.74
$\mathbf{c_2}$ [10^{-3} kA^{-1}]	-4.78 ± 0.113	-4.80 ± 0.062	-4.87 ± 0.162	-4.89 ± 0.270

$$R = \begin{pmatrix} \rho(c_0, c_0) & \rho(c_0, c_1) & \rho(c_0, c_2) \\ \rho(c_1, c_0) & \rho(c_1, c_1) & \rho(c_1, c_2) \\ \rho(c_2, c_0) & \rho(c_2, c_1) & \rho(c_2, c_2) \end{pmatrix} = \begin{pmatrix} 1.000 & -0.933 & 0.867 \\ -0.933 & 1.000 & -0.986 \\ 0.867 & -0.986 & 1.000 \end{pmatrix}$$

The error of the scaling from one current value $I_A = 1000\,\mathrm{A}$ to another current value $I_B = 2900\,\mathrm{A}$ is of interest. Including this, the formula for the error propagation become slightly more complicated:

$$\begin{aligned} s^2\left(\frac{B_B}{B_A}\right) &= \sum_{i=0}^{2}\sum_{k=0}^{2}\left(\frac{\frac{\partial B_B}{\partial c_i}B_A - \frac{\partial B_A}{\partial c_i}B_B}{B_A^2}\right)\left(\frac{\frac{\partial B_B}{\partial c_k}B_A - \frac{\partial B_A}{\partial c_k}B_B}{B_A^2}\right)\mathrm{cov}(i,k) \\ &= \frac{1}{(B_A)^4}\sum_{i=0}^{2}\sum_{k=0}^{2}\left(\frac{\partial B_B}{\partial c_i}B_A - \frac{\partial B_A}{\partial c_i}B_B\right)\left(\frac{\partial B_B}{\partial c_k}B_A - \frac{\partial B_A}{\partial c_k}B_B\right)\mathrm{cov}(i,k) \end{aligned}$$

As a result, the following values are retrieved for the scaling factor $\alpha = B_B/B_A$ and its error $\delta_\alpha = \sqrt{s^2(B_B/B_A)}$. This is done for each of the four permanent probes at the different nominal current values:

parameters	probe 101	probe 102	probe 103	probe 105
α(2600 A)	2.57825	2.57825	2.58441	2.58107
δ_α(2600 A)	0.00025	0.00014	0.00037	0.00061
α(2700 A)	2.67608	2.67607	2.68260	2.67905
δ_α(2700 A)	0.00027	0.00015	0.00039	0.00066
α(2900 A)	2.87144	2.87142	2.87869	2.8472
δ_α(2900 A)	0.00032	0.00017	0.00045	0.00076

A.3 Measurement of Magnet Stability with the Permanent Probes

Four permanently installed probes monitor the temperature and the B-field values over a longer period, which allows to correct precisely the temperature dependence of the four probes, as it is shown in Figure A.5. Since these are the reference probes for determining the scaling of the B-Field from ~700 G up to ~2000 G a good knowledge of this effect is required.

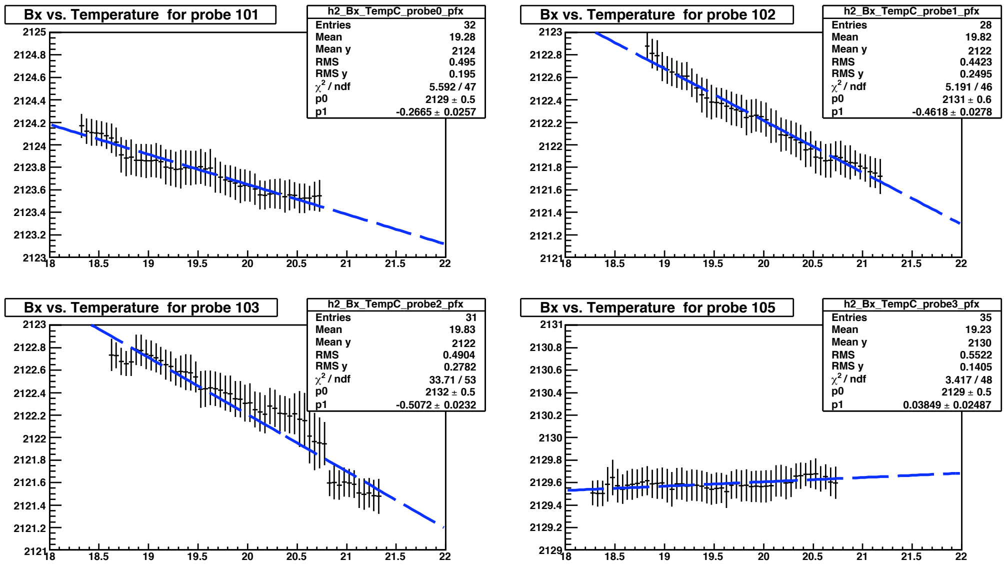

Figure A.5: Temperature dependence of the B-field value for the four permanent probes. A linear trend for each probe is visible which is corrected for by using the parameters of the linear fit for each probe. The x-axes show the temperature in °C, the y-axes show the measured magnetic field in G.

A.4 Some Slices of the B-field Map

This section shows various slices of the B-field maps after corrections in all three dimensions. In addition to the planes through the origin of the ND280 coordinate system, the B-field values at the TPC readout planes and at the downstream end of TPC 3 are shown.

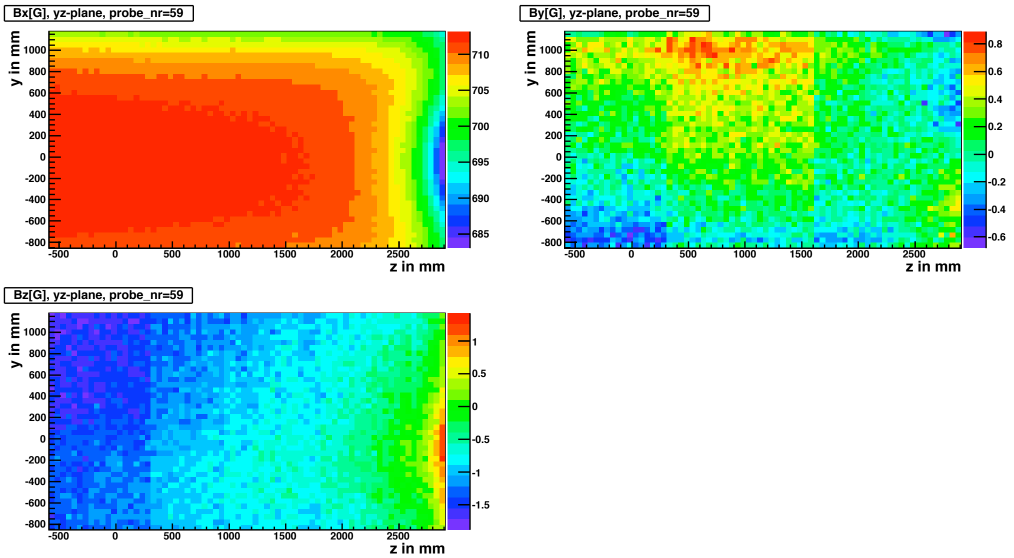

Figure A.6: B_x (top left), B_y (top right) and B_z (bottom left) in the x=0-plane. The colors indicate the B-field in G. Note that each plot has a different scale for the colors.

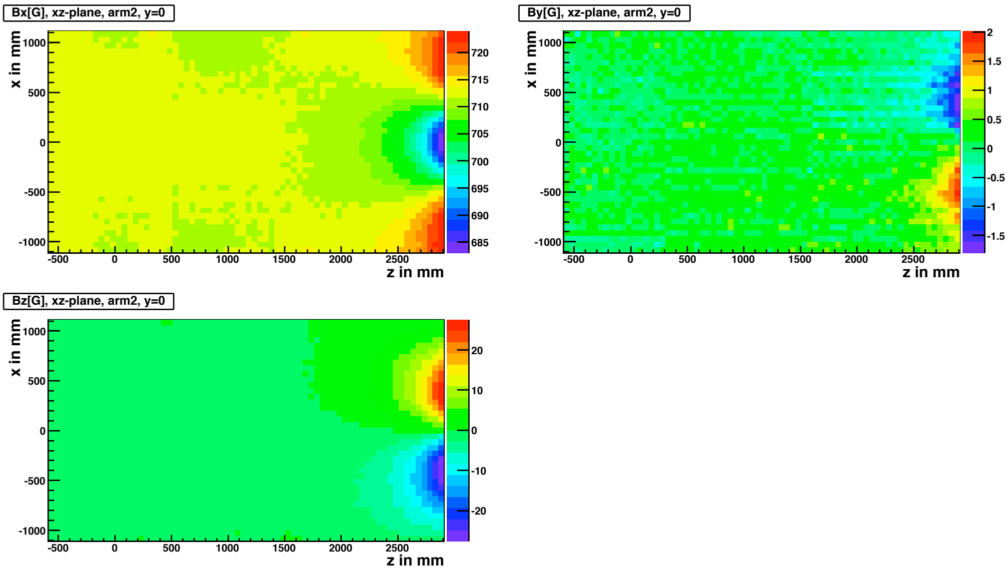

Figure A.7: B_x (top left), B_y (top right) and B_z (bottom left) in the y=0-plane. The colors indicate the B-field in G. Note that each plot has a different scale for the colors.

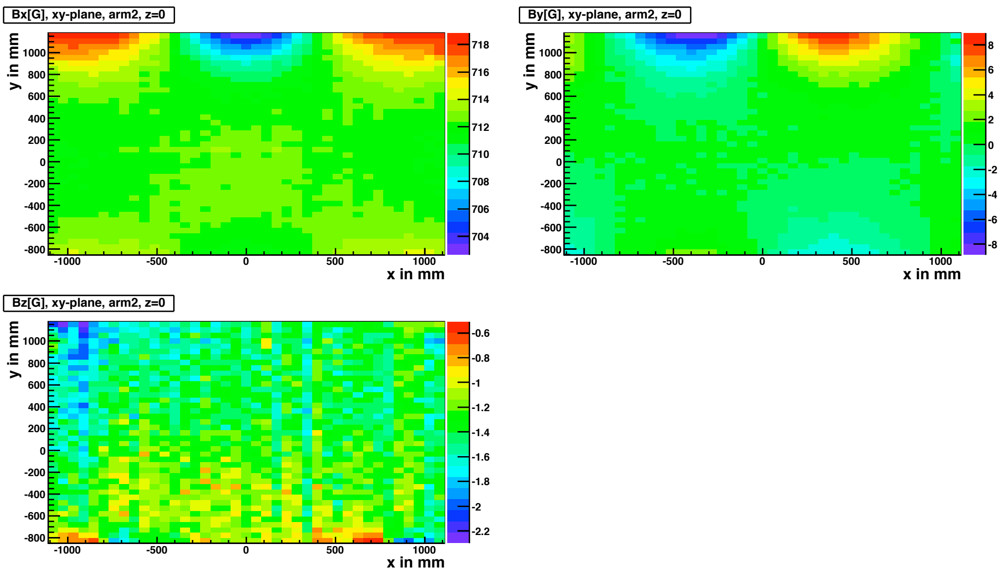

Figure A.8: B_x (top left), B_y (top right) and B_z (bottom left) in the z=0-plane. The colors indicate the B-field in G. Note that each plot has a different scale for the colors.

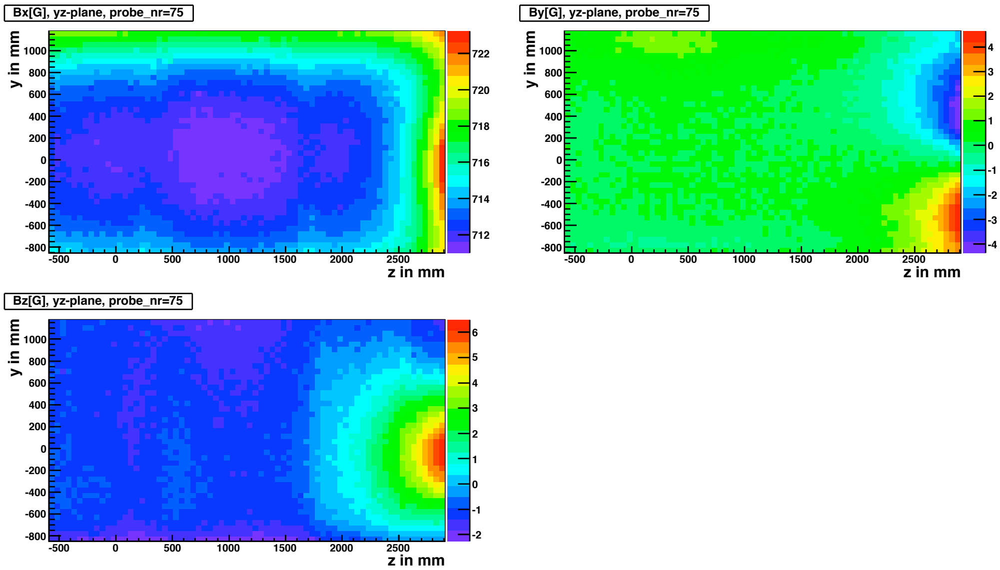

Figure A.9: B_x (top left), B_y (top right) and B_z (bottom left) in the yz-plane where x=912 mm. This corresponds roughly to the position of one of the two readout planes (x=900 mm) of the TPCs. The colors indicate the B-field in G. Note that each plot has a different scale for the colors.

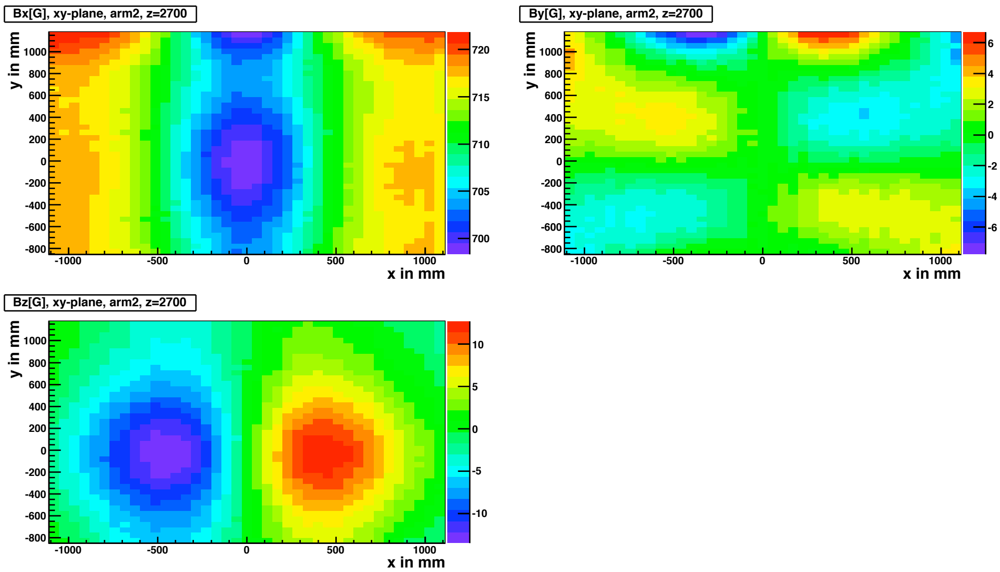

Figure A.10: B_x (top left), B_y (top right) and B_z (bottom left) in the yz-plane where z=2700 mm. This corresponds to the most downstream position of TPC 3. The colors indicate the B-field in G. Note that each plot has a different scale for the colors.

List of Figures

List of Tables

Bibliography

[1] J. Bahcall. *The solar neutrino problem*. Comments Nucl.Part.Phys. **A5** 59–64 (1972).

[2] K. Abe et al. *Indication of Electron Neutrino Appearance from an Accelerator-produced Off-axis Muon Neutrino Beam*. Phys.Rev.Lett. **107** 041801 (2011).
http://dx.doi.org/10.1103/PhysRevLett.107.041801.

[3] P. Adamson et al. *Improved search for muon-neutrino to electron-neutrino oscillations in MINOS*. Phys.Rev.Lett. **107** 181802 (2011).
http://dx.doi.org/10.1103/PhysRevLett.107.181802.

[4] Y. Abe et al. *Indication for the disappearance of reactor electron antineutrinos in the Double Chooz experiment* (2011).
http://arxiv.org/abs/arXiv:1112.6353.

[5] W. Pauli. *Dear radioactive ladies and gentlemen*. Phys. Today **31N9** 27 (1978).

[6] H. Bethe and R. Peierls. *The 'neutrino'*. Nature **133** 532 (1934).

[7] E. Fermi. *An attempt of a theory of beta radiation. 1*. Z. Phys. **88** 161–177 (1934).
http://www.springerlink.com/content/wq2r06j058382226.

[8] F. Reines and C. L. Cowan. *The neutrino*. Nature **178** 446–449 (1956).
http://dx.doi.org/10.1038/178446a0.

[9] G. Danby et al. *Observation of High-Energy Neutrino Reactions and the Existence of Two Kinds of Neutrinos*. Phys. Rev. Lett. **9 1** 36–44 (1962).
http://dx.doi.org/10.1103/PhysRevLett.9.36.

[10] K. Kodama et al. *Final tau-neutrino results from the DONuT experiment*. Phys.Rev. **D78** 052002 (2008).
http://dx.doi.org/10.1103/PhysRevD.78.052002.

[11] *Precision electroweak measurements on the Z resonance*. Phys.Rept. **427** 257–454 (2006).
http://dx.doi.org/10.1016/j.physrep.2005.12.006.

[12] Wikipedia. *Standard Model* (2006). [Online; accessed 12-January-2012]. http://en.wikipedia.org/wiki/File:Standard_Model_of_Elementary_Particles.svg.

[13] S. Tomonaga. *On a relativistically invariant formulation of the quantum theory of wave fields*. Prog.Theor.Phys. **1** 27–42 (1946).

[14] J. S. Schwinger. *On quantum electrodynamics and the magnetic moment of the electron*. Phys.Rev. **73** 416–417 (1948). http://dx.doi.org/10.1103/PhysRev.73.416.

[15] R. Feynman. *Space-time approach to quantum electrodynamics*. Phys.Rev. **76** 769–789 (1949). http://dx.doi.org/10.1103/PhysRev.76.769.

[16] K. Nakamura et al. *Review of particle physics*. J.Phys.G **G37** 075021 (2010). http://dx.doi.org/10.1088/0954-3899/37/7A/075021.

[17] N. Cabibbo. *Unitary Symmetry and Leptonic Decays*. Phys.Rev.Lett. **10** 531–533 (1963). http://dx.doi.org/10.1103/PhysRevLett.10.531.

[18] M. Kobayashi and T. Maskawa. *CP Violation in the Renormalizable Theory of Weak Interaction*. Prog.Theor.Phys. **49** 652–657 (1973). http://dx.doi.org/10.1143/PTP.49.652.

[19] S. Glashow. *Partial Symmetries of Weak Interactions*. Nucl.Phys. **22** 579–588 (1961). http://dx.doi.org/10.1016/0029-5582(61)90469-2.

[20] S. Weinberg. *A Model of Leptons*. Phys.Rev.Lett. **19** 1264–1266 (1967). http://dx.doi.org/10.1103/PhysRevLett.19.1264.

[21] M. Goldhaber et al. *Helicity of Neutrinos*. Phys.Rev. **109** 1015–1017 (1958). http://dx.doi.org/10.1103/PhysRev.109.1015.

[22] C. Wu et al. *Experimental Test of Parity Conservation in Beta Decay*. Phys.Rev. **105** 1413–1414 (1957). http://dx.doi.org/10.1103/PhysRev.105.1413.

[23] J. Christenson et al. *Evidence for the 2π Decay of the K_2^0 Meson*. Phys.Rev.Lett. **13** 138–140 (1964). http://dx.doi.org/10.1103/PhysRevLett.13.138.

[24] D. London and R. Peccei. *Penguin Effects in Hadronic B Asymmetries*. Phys.Lett. **B223** 257 (1989). http://dx.doi.org/10.1016/0370-2693(89)90249-9.

[25] G. Zeller. *MiniBooNE neutrino and antineutrino cross sections* (pp. 103–113) (2006).

[26] M. Antonello et al. *Study of Pion Production in ν_μ CC Interactions on ^{16}O Using Different MC Generators*. Acta Phys.Polon. **B40** 2519–2535 (2009). http://th-www.if.uj.edu.pl/acta/vol40/pdf/v40p2519.pdf.

[27] R. P. Feynman. *Very high-energy collisions of hadrons*. Phys.Rev.Lett. **23** 1415–1417 (1969). http://dx.doi.org/10.1103/PhysRevLett.23.1415.

[28] P. Adamson et al. *Neutrino and Antineutrino Inclusive Charged-current Cross Section Measurements with the MINOS Near Detector*. Phys.Rev. **D81** 072002 (2010). http://dx.doi.org/10.1103/PhysRevD.81.072002.

[29] Y. Hayato. *A neutrino interaction simulation program library NEUT*. Acta Phys.Polon. **B40** 2477–2489 (2009). http://th-www.if.uj.edu.pl/acta/vol40/pdf/v40p2477.pdf.

[30] C. Andreopoulos et al. *The GENIE Neutrino Monte Carlo Generator*. Nucl.Instrum.Meth. **A614** 87–104 (2010). http://dx.doi.org/10.1016/j.nima.2009.12.009.

[31] C. Llewellyn Smith. *Neutrino Reactions at Accelerator Energies*. Phys.Rept. **3** 261–379 (1972). http://dx.doi.org/10.1016/0370-1573(72)90010-5.

[32] D. Rein and L. M. Sehgal. *Neutrino Excitation of Baryon Resonances and Single Pion Production*. Annals Phys. **133** 79–153 (1981). http://dx.doi.org/10.1016/0003-4916(81)90242-6.

[33] G. Miller. *Fermi Gas Model*. Nucl.Phys.Proc.Suppl. **112** 223–225 (2002). http://dx.doi.org/10.1016/S0920-5632(02)01786-3.

[34] N. J. Baker et al. *Total cross sections for $\nu_\mu n$ and $\nu_\mu p$ charged-current interactions in the 7-foot bubble chamber*. Phys. Rev. **D25** 617–623 (1982). http://dx.doi.org/10.1103/PhysRevD.25.617.

[35] M. Derrick et al. *Study of single-pion production by weak neutral currents in low-energy νd interactions*. Phys.Rev. **D23** 569 (1981). http://dx.doi.org/10.1103/PhysRevD.23.569.

[36] G. Radecky et al. *Study of Single Pion Production by Weak Charged Currents in Low-energy νd interactions*. Phys.Rev. **D25** 1161–1173 (1982). http://dx.doi.org/10.1103/PhysRevD.25.1161,10.1103/PhysRevD.26.3297.

[37] W.-Y. Lee et al. *Single Pion Production in Neutrino and anti-neutrino Reactions*. Phys.Rev.Lett. **38** 202 (1977). http://dx.doi.org/10.1103/PhysRevLett.38.202.

[38] M. Hasegawa et al. *Search for coherent charged pion production in neutrino-carbon interactions*. Phys.Rev.Lett. **95** 252301 (2005).
http://dx.doi.org/10.1103/PhysRevLett.95.252301.

[39] A. Aguilar-Arevalo et al. *First Observation of Coherent π^0 Production in Neutrino Nucleus Interactions with E_ν ∼2 GeV*. Phys.Lett. **B664** 41–46 (2008).
http://dx.doi.org/10.1016/j.physletb.2008.05.006.

[40] K. Hiraide et al. *Search for Charged Current Coherent Pion Production on Carbon in a Few-GeV Neutrino Beam*. Phys.Rev. **D78** 112004 (2008).
http://dx.doi.org/10.1103/PhysRevD.78.112004.

[41] Y. Kurimoto et al. *Improved measurement of neutral current coherent π^0 production on carbon in a few-GeV neutrino beam*. Phys.Rev. **D81** 111102 (2010).
http://dx.doi.org/10.1103/PhysRevD.81.111102.

[42] Y. Fukuda et al. *Evidence for oscillation of atmospheric neutrinos*. Phys.Rev.Lett. **81** 1562–1567 (1998).
http://dx.doi.org/10.1103/PhysRevLett.81.1562.

[43] Y. Ashie et al. *Evidence for an oscillatory signature in atmospheric neutrino oscillation*. Phys.Rev.Lett. **93** 101801 (2004).
http://dx.doi.org/10.1103/PhysRevLett.93.101801.

[44] K. Eguchi et al. *First results from KamLAND: Evidence for reactor anti-neutrino disappearance*. Phys.Rev.Lett. **90** 021802 (2003).
http://dx.doi.org/10.1103/PhysRevLett.90.021802.

[45] T. Araki et al. *Measurement of neutrino oscillation with KamLAND: Evidence of spectral distortion*. Phys.Rev.Lett. **94** 081801 (2005).
http://dx.doi.org/10.1103/PhysRevLett.94.081801.

[46] M. Apollonio et al. *Limits on neutrino oscillations from the CHOOZ experiment*. Phys.Lett. **B466** 415–430 (1999).
http://dx.doi.org/10.1016/S0370-2693(99)01072-2.

[47] E. Aliu et al. *Evidence for muon neutrino oscillation in an accelerator-based experiment*. Phys.Rev.Lett. **94** 081802 (2005).
http://dx.doi.org/10.1103/PhysRevLett.94.081802.

[48] M. Ahn et al. *Measurement of Neutrino Oscillation by the K2K Experiment*. Phys.Rev. **D74** 072003 (2006).
http://dx.doi.org/10.1103/PhysRevD.74.072003.

[49] N. Agafonova et al. *Observation of a first ν_τ candidate in the OPERA experiment in the CNGS beam*. Phys.Lett. **B691** 138–145 (2010).
http://dx.doi.org/10.1016/j.physletb.2010.06.022.

[50] P. Adamson et al. *Measurement of Neutrino Oscillations with the MINOS Detectors in the NuMI Beam.* Phys.Rev.Lett. **101** 131802 (2008).
http://dx.doi.org/10.1103/PhysRevLett.101.131802.

[51] Q. Ahmad et al. *Direct evidence for neutrino flavor transformation from neutral current interactions in the Sudbury Neutrino Observatory.* Phys.Rev.Lett. **89** 011301 (2002).
http://dx.doi.org/10.1103/PhysRevLett.89.011301.

[52] M. Cribier. *Results of the whole GALLEX experiment.* Nucl.Phys.Proc.Suppl. **70** 284–291 (1999).
http://dx.doi.org/10.1016/S0920-5632(98)00438-1.

[53] V. Gavrin et al. *Solar neutrino results from SAGE.* Part.Nucl.Lett. **108** 18–26 (2001).
http://dx.doi.org/10.1016/S0920-5632(00)00920-8.

[54] Y. Fukuda et al. *Measurement of the solar neutrino energy spectrum using neutrino electron scattering.* Phys.Rev.Lett. **82** 2430–2434 (1999).
http://dx.doi.org/10.1103/PhysRevLett.82.2430.

[55] B. Pontecorvo. *Inverse beta processes and nonconservation of lepton charge.* Sov.Phys.JETP **7** 172–173 (1958).

[56] Z. Maki et al. *Remarks on the unified model of elementary particles.* Prog.Theor.Phys. **28** 870–880 (1962).
http://dx.doi.org/10.1143/PTP.28.870.

[57] N. Schmitz. *Neutrinophysik* (1997).

[58] L. Wolfenstein. *Neutrino oscillations in matter.* Phys. Rev. **D17** 2369–2374 (1978).
http://dx.doi.org/10.1103/PhysRevD.17.2369.

[59] S. Mikheev and A. Smirnov. *Resonance Amplification of Oscillations in Matter and Spectroscopy of Solar Neutrinos.* Sov.J.Nucl.Phys. **42** 913–917 (1985).
http://dx.doi.org/10.1007/BF02508049.

[60] J. N. Bahcall et al. *New solar opacities, abundances, helioseismology, and neutrino fluxes.* Astrophys.J. **621** L85–L88 (2005).
http://dx.doi.org/10.1086/428929.

[61] S. Fukuda et al. *Determination of solar neutrino oscillation parameters using 1496 days of Super-Kamiokande I data.* Phys.Lett. **B539** 179–187 (2002).
http://dx.doi.org/10.1016/S0370-2693(02)02090-7.

[62] B. Aharmim et al. *Electron energy spectra, fluxes, and day-night asymmetries of B-8 solar neutrinos from measurements with NaCl dissolved in the*

heavy-water detector at the Sudbury Neutrino Observatory. Phys.Rev. **C72** 055502 (2005).
http://dx.doi.org/10.1103/PhysRevC.72.055502.

[63] M. Guzzo et al. *Adiabatic matter effect with three generation neutrinos and the solar neutrino problem* (1994).
http://arxiv.org/abs/hep-ph/9412331.

[64] D. Ayres et al. *NOvA: Proposal to build a 30 kiloton off-axis detector to study $\nu_\mu \rightarrow \nu_e$ oscillations in the NuMI beamline* (2004). Updated version of 2004 proposal. Higher resolution version available at Fermilab Library Server
http://arxiv.org/abs/hep-ex/0503053.

[65] A. Cervera et al. *Golden measurements at a neutrino factory*. Nucl.Phys. **B579** 17–55 (2000).
http://dx.doi.org/10.1016/S0550-3213(00)00221-2.

[66] E. K. Akhmedov et al. *Series expansions for three flavor neutrino oscillation probabilities in matter*. JHEP **0404** 078 (2004).
http://dx.doi.org/10.1088/1126-6708/2004/04/078.

[67] P. Huber et al. *Optimization of a neutrino factory oscillation experiment*. Phys.Rev. **D74** 073003 (2006).
http://dx.doi.org/10.1103/PhysRevD.74.073003.

[68] Wikimedia. *Neutrino Hierarchy* (2011). [Online; accessed 17-January-2012]
http://commons.wikimedia.org/wiki/File:NeutrinoHierarchy.svg.

[69] A. Strumia and F. Vissani. *Implications of neutrino data circa 2005*. Nucl.Phys. **B726** 294–316 (2005).
http://dx.doi.org/10.1016/j.nuclphysb.2005.07.031.

[70] Y. Y. Wong. *Neutrino mass in cosmology: status and prospects*. Ann.Rev.Nucl.Part.Sci. **61** 69–98 (2011).
http://dx.doi.org/10.1146/annurev-nucl-102010-130252.

[71] J. Angrik et al. *KATRIN design report 2004* (2005).
http://inspirehep.net/record/680949/files/FZKA7090.pdf.

[72] I. Avignone, Frank T. et al. *Double Beta Decay, Majorana Neutrinos, and Neutrino Mass*. Rev.Mod.Phys. **80** 481–516 (2008).
http://dx.doi.org/10.1103/RevModPhys.80.481.

[73] S. Weinberg. *Varieties of Baryon and Lepton Nonconservation*. Phys.Rev. **D22** 1694 (1980).
http://dx.doi.org/10.1103/PhysRevD.22.1694.

[74] P. Minkowski. *$\mu \rightarrow e\gamma$ at a Rate of One Out of 1-Billion Muon Decays?* Phys.Lett. **B67** 421 (1977).
http://dx.doi.org/10.1016/0370-2693(77)90435-X.

[75] T. Yanagida. *Horizontal Symmetry and Masses of Neutrinos*. Conf.Proc. **C7902131** 95 (1979).
http://cdsweb.cern.ch/record/1071797.

[76] M. Gell-Mann et al. *Complex Spinors And Unified Theories*. Conf.Proc. **C790927** 315–321 (1979).
http://cdsweb.cern.ch/record/133618.

[77] R. N. Mohapatra and G. Senjanovic. *Neutrino Mass and Spontaneous Parity Violation*. Phys.Rev.Lett. **44** 912 (1980).
http://dx.doi.org/10.1103/PhysRevLett.44.912.

[78] W. Konetschny and W. Kummer. *Nonconservation of Total Lepton Number with Scalar Bosons*. Phys.Lett. **B70** 433 (1977).
http://dx.doi.org/10.1016/0370-2693(77)90407-5.

[79] R. N. Mohapatra and G. Senjanovic. *Neutrino Masses and Mixings in Gauge Models with Spontaneous Parity Violation*. Phys.Rev. **D23** 165 (1981).
http://dx.doi.org/10.1103/PhysRevD.23.165.

[80] T. Cheng and L.-F. Li. *Neutrino Masses, Mixings and Oscillations in SU(2) x U(1) Models of Electroweak Interactions*. Phys.Rev. **D22** 2860 (1980).
http://dx.doi.org/10.1103/PhysRevD.22.2860.

[81] G. Lazarides et al. *Proton Lifetime and Fermion Masses in an SO(10) Model*. Nucl.Phys. **B181** 287 (1981).
http://dx.doi.org/10.1016/0550-3213(81)90354-0.

[82] J. Schechter and J. Valle. *Neutrino Masses in SU(2) $\times$ U(1) Theories*. Phys.Rev. **D22** 2227 (1980).
http://dx.doi.org/10.1103/PhysRevD.22.2227.

[83] R. Foot et al. *See-saw neutrino masses induced by a triplet of leptons*. Z.Phys. **C44** 441 (1989).
http://dx.doi.org/10.1007/BF01415558.

[84] G. Branco et al. *Leptonic CP violation* (2011).
http://arxiv.org/abs/arXiv:1111.5332.

[85] G. Fogli et al. *Evidence of $\theta_{13} > 0$ from global neutrino data analysis*. Phys.Rev. **D84** 053007 (2011).
http://dx.doi.org/10.1103/PhysRevD.84.053007.

[86] T. Schwetz et al. *Where we are on θ_{13}: addendum to 'Global neutrino data and recent reactor fluxes: status of three-flavour oscillation parameters'*. New J.Phys. **13** 109401 (2011).
http://dx.doi.org/10.1088/1367-2630/13/10/109401.

[87] M. Huang et al. *Global Neutrino Data Analysis and the Quest to Pin Down $\sin\theta_{13}$ in Different Mixing Matrix Parametrizations* (2011).
http://arxiv.org/abs/arXiv:1111.3175.

[88] J. Ahn et al. *RENO: An Experiment for Neutrino Oscillation Parameter θ_{13} Using Reactor Neutrinos at Yonggwang* (2010). http://arxiv.org/abs/arXiv:1003.1391.

[89] X. Guo et al. *A Precision measurement of the neutrino mixing angle theta(13) using reactor antineutrinos at Daya-Bay* (2007). http://arxiv.org/abs/hep-ex/0701029.

[90] J. Adam et al. *New limit on the lepton-flavour violating decay $\mu^+ \to e^+\gamma$*. Phys.Rev.Lett. **107** 171801 (2011). http://dx.doi.org/10.1103/PhysRevLett.107.171801.

[91] J. Arafune et al. *CP violation and matter effect in long baseline neutrino oscillation experiments*. Phys.Rev. **D56** 3093–3099 (1997). http://dx.doi.org/10.1103/PhysRevD.56.3093,10.1103/PhysRevD.60.119905.

[92] H. Minakata and H. Nunokawa. *CP violation versus matter effect in long baseline neutrino oscillation experiments*. Phys.Rev. **D57** 4403–4417 (1998). http://dx.doi.org/10.1103/PhysRevD.57.4403.

[93] H. Minakata and S. Uchinami. *Parameter Degeneracy in Neutrino Oscillation – Solution Network and Structural Overview –*. JHEP **1004** 111 (2010). http://dx.doi.org/10.1007/JHEP04(2010)111.

[94] R. H. Cyburt et al. *New BBN limits on physics beyond the standard model from He-4*. Astropart.Phys. **23** 313–323 (2005). http://dx.doi.org/10.1016/j.astropartphys.2005.01.005.

[95] W. Hu and S. Dodelson. *Cosmic microwave background anisotropies*. Ann.Rev.Astron.Astrophys. **40** 171–216 (2002). http://dx.doi.org/10.1146/annurev.astro.40.060401.093926.

[96] A. Sakharov. *Violation of CP Invariance, c Asymmetry, and Baryon Asymmetry of the Universe*. Pisma Zh.Eksp.Teor.Fiz. **5** 32–35 (1967).

[97] M. Trodden. *Baryogenesis and leptogenesis*. eConf **C040802** L018 (2004). http://arxiv.org/abs/hep-ph/0411301.

[98] F. R. Klinkhamer and N. Manton. *A Saddle Point Solution in the Weinberg-Salam Theory*. Phys.Rev. **D30** 2212 (1984). http://dx.doi.org/10.1103/PhysRevD.30.2212.

[99] K. Abe and J. Spitz. *The T2K Experiment*. Nucl.Instrum.Meth. **A659** 106–135 (2011). http://dx.doi.org/10.1016/j.nima.2011.06.067.

[100] Y. Itow et al. *The JHF-Kamioka neutrino project* (pp. 239–248) (2001). http://arxiv.org/abs/hep-ex/0106019.

[101] Y. Fukuda et al. *The Super-Kamiokande detector*. Nucl. Instrum. Meth. **A501** 418–462 (2003).
http://dx.doi.org/10.1016/S0168-9002(03)00425-X.

[102] K. Abe et al. *Letter of Intent: The Hyper-Kamiokande Experiment — Detector Design and Physics Potential —* (2011).
http://arxiv.org/abs/arXiv:1109.3262.

[103] S. Davidson et al. *Leptogenesis*. Phys.Rept. **466** 105–177 (2008).
http://dx.doi.org/10.1016/j.physrep.2008.06.002.

[104] K. Matsuoka et al. *Design and performance of the muon monitor for the T2K neutrino oscillation experiment*. Nucl.Instrum.Meth. **A624** 591–600 (2010).
http://dx.doi.org/10.1016/j.nima.2010.09.074.

[105] S. van der Meer. *A directive device for charged particles and its use in an enhanced neutrino beam* (1961).

[106] S. Bhadra et al. *Optical Transition Radiation Monitor for the T2K Experiment* (2012).
http://arxiv.org/abs/arXiv:1201.1922.

[107] K. Matsuoka et al. *Development and production of the ionization chamber for the T2K muon monitor*. Nucl.Instrum.Meth. **A623** 385–387 (2010).
http://dx.doi.org/10.1016/j.nima.2010.03.010.

[108] K. Abe et al. *Measurements of the T2K neutrino beam properties using the INGRID on-axis near detector* (2011).
http://arxiv.org/abs/arXiv:1111.3119.

[109] G. Arnison et al. *Experimental Observation of Lepton Pairs of Invariant Mass Around* $95\,\mathrm{GeV}/\mathrm{c}^2$ *at the CERN SPS Collider*. Phys.Lett. **B126** 398–410 (1983).
http://dx.doi.org/10.1016/0370-2693(83)90188-0.

[110] J. Altegoer et al. *The NOMAD experiment at the CERN SPS*. Nucl.Instrum.Meth. **A404** 96–128 (1998).
http://dx.doi.org/10.1016/S0168-9002(97)01079-6.

[111] S. Assylbekov et al. *The T2K ND280 Off-Axis Pi-Zero Detector* (2011).

[112] D. Karlen. *Time projection chambers for the T2K experiment*. Nucl.Instrum.Meth. **A623** 108–110 (2010).
http://dx.doi.org/10.1016/j.nima.2010.02.164.

[113] I. Giomataris et al. *Micromegas in a bulk*. Nucl.Instrum.Meth. **A560** 405–408 (2006).
http://dx.doi.org/10.1016/j.nima.2005.12.222.

[114] S. Ahn et al. *Detection of accelerator produced neutrinos at a distance of 250-km*. Phys.Lett. **B511** 178–184 (2001).
http://dx.doi.org/10.1016/S0370-2693(01)00647-5.

[115] Y. Ashie et al. *A Measurement of atmospheric neutrino oscillation parameters by SUPER-KAMIOKANDE I*. Phys.Rev. **D71** 112005 (2005).
http://dx.doi.org/10.1103/PhysRevD.71.112005.

[116] J. Hosaka et al. *Three flavor neutrino oscillation analysis of atmospheric neutrinos in Super-Kamiokande*. Phys.Rev. **D74** 032002 (2006).
http://dx.doi.org/10.1103/PhysRevD.74.032002.

[117] M. Shiozawa et al. *Search for proton decay via* $p \rightarrow e^+\pi^0$ *in a large water Cherenkov detector*. Phys.Rev.Lett. **81** 3319–3323 (1998).
http://dx.doi.org/10.1103/PhysRevLett.81.3319.

[118] Y. Hayato et al. *Search for proton decay through* $p \rightarrow \bar{\nu}K^+$ *in a large water Cherenkov detector*. Phys.Rev.Lett. **83** 1529–1533 (1999).
http://dx.doi.org/10.1103/PhysRevLett.83.1529.

[119] H. Nishino et al. *Search for Proton Decay via* $p \rightarrow e^+\pi^0$ *and* $p \rightarrow \mu^+\pi^0$ *in a Large Water Cherenkov Detector*. Phys.Rev.Lett. **102** 141801 (2009).
http://dx.doi.org/10.1103/PhysRevLett.102.141801.

[120] E. Frank et al. *A dedicated device for measuring the magnetic field of the ND280 magnet in the T2K experiment*. Journal of Instrumentation **7 01** P01018 (2012).
http://stacks.iop.org/1748-0221/7/i=01/a=P01018.

[121] E. Frank et al. *B-field calibration and systematic errors* (2011). T2K technical note T2K-TN-081 (unpublished).

[122] ND280 Magnet Group. *The ND280 Magnet*. Nucl.Instrum.Meth. (2012). In preparation.

[123] Hall probes developed by NIKHEF.
http://www.nikhef.nl/pub/departments/ct/po/html/dcs.html.

[124] Robert Bosch GmbH. *CAN - Controller Area Network Funktionelle Beschreibung*.

[125] D. Karlen. *Aligning the Tracker in the ND280 basket*. T2K technical note T2K-TN-010 (unpublished).
http://www.t2k.org/docs/technotes/010.

[126] F. Bergsma. *Calibration of Hall sensors in three dimensions*. 13th International Magnetic Measurement Workshop, 2003, SLAC.
http://www.slac.stanford.edu/cgi-wrap/getdoc/slac-wp-029-ch13-Bergsma.pdf.

[127] M. Aleksa et al. *Measurement of the ATLAS solenoid magnetic field*. JINST **3** P04003 (2008).
http://dx.doi.org/10.1088/1748-0221/3/04/P04003.

[128] M. Aleksa et al. *Measurement of the solenoid magnetic field* (2007). ATLAS Note ATL-MAGNET-PUB-2007-001.
http://cdsweb.cern.ch/record/1055329/files/magnet-pub-2007-001.pdf.

[129] Bock, R. K. and Thompson, G. *The UA1 Magnetic Field Measurement*. UA1 technical note TN-80/62 (1980).
http://www.t2k.org/nd280/magnet/b-field-mapping/UA1_Bfield/view.

[130] TOSCA/OPERA-3D Software Vector Fields Ltd.. Oxford, U. K.
http://www.cobham.com/about-cobham/aerospace-and-security/about-us/antenna-systems/kidlington.aspx.

[131] F. James and M. Roos. *Minuit: A System for Function Minimization and Analysis of the Parameter Errors and Correlations*. Comput.Phys.Commun. **10** 343–367 (1975).
http://dx.doi.org/10.1016/0010-4655(75)90039-9.

[132] F. Dao et al. *pp Interactions at* 303 GeV/c*; Inclusive Measurement of* Δ^{++} *(1236) Resonance Production*. Phys.Rev.Lett. **30** 34 (1973).
http://dx.doi.org/10.1103/PhysRevLett.30.34.

[133] D. Lichtenberg. *The Masses and Widths of the* Δ^{++} *and* Δ^0 *Resonances*. Lett.Nuovo Cim. **12** 616 (1975).

[134] A. Cervera and others. *Inclusive* ν_μ *CC analysis using the entire ND280 detector*. T2K technical note T2K-TN-044 (unpublished).
http://www.t2k.org/docs/technotes/044.

[135] C. Giganti. *Particle Identification in the T2K TPCs and study of the electron neutrino component in the T2K neutrino beam* (2010). Ph.D. thesis.
http://irfu.cea.fr/Phocea/file.php?class=std&&file=Doc/Publications/Archives/irfu-10-06-T.pdf.

[136] H. Bethe. *Theory of the passage of fast corpuscular rays through matter*. Annalen Phys. **5** 325–400 (1930). Published in English in SELECTED WORKS OF HANS A. BETHE: With Commentary, World Scientific, 1997. (World Scientific Series in 20th Century Physics, Vol. 18). pp. 77-154.

[137] B. List. *Why and When to Optimize Efficiency Times Purity* (2002). [Online; accessed 09-February-2012].
http://www.desy.de/~blist/notes/whyeffpur.ps.gz.

[138] W. Verkerke and D. P. Kirkby. *The RooFit toolkit for data modeling*. eConf **C0303241** MOLT007 (2003).
http://arxiv.org/pdf/physics/0306116.

Acknowledgements

I would like to thank first of all Prof. Dr. Antonio Ereditato for giving me the opportunity of working at the frontier of neutrino physics and thereby doing a Ph.D. at LHEP.

Of course, I owe my thanks to a lot of colleagues at LHEP, but I want to emphasize the special effort of some: Marcello for the support and the inspiring physics discussions throughout the years, which often resulted in new ideas and approaches; Aki for the support in Japan, especially during the time of installation of the mapping device; Roger, Remo, Fatih, and Joël for their outstanding effort as shifters, friends and troubleshooters during the mapping campaign of the ND280 magnet; Michele, Claudia, Martti, Saverio, and Thomas for their efforts in proof-reading my not always well-written documents; Irene and Ursula, who were a great a help in organizing the trips to Japan and fixing all the small, big, or nasty bureaucratic problems throughout my time as Ph.D. student. And last but not least, all the people who contributed to the friendly and open-minded environment at LHEP, and also apart from work.

There is a great bunch of people outside of LHEP who contributed in huge parts to the success of the projects throughout my time as a Ph.D student. My sincere thanks go to Dr. Morgan Wascko for accepting to co-referee and his contagious enthusiasm for physics during and after working hours. Furthermore, I would like to thank: Pierre-Ange, Francois, Antoine, and Felix for their big efforts at CERN and J-PARC to accomplish the mapping of the ND280 magnet; Federico, Dean, Marco, Alberto, and many others for valuable physics discussions; My fellow Ph.D students (at that time) of the T2K collaboration for their various contributions for physics and beyond during the meetings in Japan.

Finally, I thank all my friends and relatives, who were not directly involved in the work which led to this thesis. Nevertheless, I cannot value highly enough their contribution, such that I reached this point in my life. I cannot name all of you, since this would take several pages, but if you read this, I am sure you are one of the most important persons.

Chronological list of the most important publications, of which I am author or co-author, during my time as a Ph.D. student:

- M. Antonella et al., *Study of Pion Production in ν_μ CC Interactions on ^{16}O Using Different MC Generators.* Acta Phys. Polon. B **40** (2009) 2519.
http://www.actaphys.uj.edu.pl/vol40/pdf/v40p2519.pdf
- E. Frank [T2K Collaboration], *Status report and performance of the T2K experiment.* in proceedings of "Identification of Dark Matter 2010", PoS IDM **2010** (2011) 103.
http://pos.sissa.it//archive/conferences/110/103/IDM2010_103.pdf
- K. Abe et al. [T2K Collaboration], *The T2K Experiment.* Nucl. Instrum. Meth. A **659** (2011) 106.
http://dx.doi.org/10.1016/j.nima.2011.06.067
- K. Abe et al. [T2K Collaboration], *Indication of Electron Neutrino Appearance from an Accelerator-produced Off-axis Muon Neutrino Beam.* Phys. Rev. Lett. **107** (2011) 041801.
http://link.aps.org/doi/10.1103/PhysRevLett.107.041801
- E. Frank et al., *A dedicated device for measuring the magnetic field of the ND280 magnet in the T2K experiment.* JINST **7** (P01018) (2012).
http://stacks.iop.org/1748-0221/7/i=01/a=P01018
- K. Abe et al. [T2K Collaboration], *First Muon-Neutrino Disappearance Study with an Off-Axis Beam.* accepted for publication in Phys. Rev. D (2012).
http://arxiv.org/pdf/arXiv:1201.1386

Erklärung

gemäss Art. 28 Abs. 2 RSL 05

Name/Vorname: Frank, Eike

Matrikelnummer: 08-115-420

Studiengang: Physik

Bachelor ☐ Master ☐ Dissertation ☒

Titel der Arbeit: Precision Measurement of the ND280 Magnetic Field in the T2K Neutrino Experiment: Confirmation of the Momentum Scale through Delta++ Resonances

LeiterIn der Arbeit: Prof. Dr. Antonio Ereditato

Ich erkläre hiermit, dass ich diese Arbeit selbständig verfasst und keine anderen als die angegebenen Quellen benutzt habe. Alle Stellen, die wörtlich oder sinngemäss aus Quellen entnommen wurden, habe ich als solche gekennzeichnet. Mir ist bekannt, dass andernfalls der Senat gemäss Artikel 36 Absatz 1 Buchstabe o des Gesetztes vom 5. September 1996 über die Universität zum Entzug des auf Grund dieser Arbeit verliehenen Titels berechtigt ist.

Bern, 21.02.2012

Ort/Datum

Unterschrift

Curriculum Vitae

Name:	Eike Frank
Birthday:	September 11th, 1982
Place of Birth	Leipzig, Germany

2008 - 2012	Ph.D. student under the supervision of Prof. Dr. Antonio Ereditato at the Albert Einstein Center for Fundamental Physics, Laboratory for High Energy Physics of the University of Bern, Switzerland.
2008 - 2012	Student of economics and business at the University of Bern, Switzerland.
2007 - 2008	Diploma student under the supervision of Prof. Dr. Caren Hagner at the University of Hamburg, Germany.
2003 - 2008	Student of physics, philosophy and meteorology at the University of Hamburg, Germany.
2002 - 2003	Correspondent student of physics and mathematics at the University of Kaiserslautern, Germany; simultaneously: community service (Zivildienst).
1995 - 2002	Grammar school: Cato Bontjes van Beek-Gymnasium Achim, Germany.
1989 - 1995	Primary school, Leipzig and Oyten (since 1991).